

EXPERIMENTAL STUDY OF MASS TRANSPORT PARAMETERS OF  
PEMFC POROUS MEDIA

by

**Praful Mangal**

A thesis submitted in partial fulfillment of the requirements for the degree of

**Master of Science**

Department of Mechanical Engineering  
**University of Alberta**

©Praful Mangal, 2014

# Abstract

An experimental set up based on a diffusion bridge is developed to accurately determine the in-plane and through-plane permeability, Knudsen diffusivity and effective molecular diffusivity of gas diffusion layers used in PEFC. The parameters are estimated under various compression levels in in-plane direction. The effect of PTFE on transport parameters is studied in both directions while effect of MPL is studied only in through plane direction. In order to estimate permeability, nitrogen is introduced in one channel, passed through the porous sample, and the pressure drop is measured. Knudsen diffusivity is measured by conducting the permeability experiments with gases of different mean paths i.e. nitrogen and helium. The difference in permeability results was attributed to Knudsen slip.

To measure diffusivity, nitrogen and oxygen are introduced in two channels separated by the porous media. By applying a pressure differential between the channels, ratio of convection and diffusion is modified, and the oxygen concentration is measured in the nitrogen channel. Permeability and effective molecular diffusivity are estimated from pressure drop and oxygen concentration measurements using a one-dimensional mass transport model.

In this study, a steady state Fick's and Darcy's law model is used for gas diffusion layers while Modified Binary Friction Model is used for GDL+MPL assembly for through plane direction. Permeability and effective diffusivity are measured for SIGRACET SGL and several Toray samples with different PTFE loading. Results

show that in-plane permeability reduces with compression and amount of PTFE in porous media. In-plane diffusivity decreases with compression, due to decreasing porosity, and with increasing PTFE content. Through plane permeability, Knudsen diffusivity and effective diffusivity also decreases with PTFE content. Coating of an MPL on GDL samples introduces significant Knudsen slip, increasing amount of PTFE in the presense of MPL also reduces permeability, Knudsen diffusivity and effective diffusivity of porous media.

**Keywords:** mass transport, gas diffusion layer, micro porous layer, permeability, effective diffusivity, Knudsen diffusivity, anisotropy

# Acknowledgements

I would like to begin thanking my supervisor - Dr. Marc Secanell for giving me the opportunity to work in the ESDLab. Throughout my graduate studies, he has been very supportive and encouraging towards my research. Discussions with him during weekly meetings and over beer were enlightening. Sharing his passion and perfection for research were both inspiring and helped to push my limits. His ability to realize ones potential and bringing it out is amazing. Had it not been for his infinite patience over the silliest mistakes I did during my stay, this thesis would not have been possible.

I would also like to thank my teachers from my undergrad days - Dr. C. Balaji, and Dr. Dhiman Chatterrji. Had I not talked to them after class, I would have never considered pursuing research.

I would like to thank the Natural Sciences and Engineering Research Council of Canada (NSERC), the Canada Foundation for Innovation (CFI), and the Government of Alberta Small Equipment Grant Program for financial support. I would also like to thank the Automotive Fuel Cell Cooperation (AFCC) for providing some of the samples used in this study.

I would also like to thank my colleagues for helping, both in research or otherwise. Nick for providing the SEM images, and Mark for conducting MIP experiments used in this thesis. Kailyn and Phil for introducing me to ice skating. Lalit for discussions over setup, theory, politics or life in general, Madhur for sharing his enthusiasm for whatever he does, Shantanu for a good laugh over coffee, Chad for giving tips about loosing weight and how to make an awesome cup of icecream.

Lastly, my parents who are the reason I exist. Their way of making me laugh over skype chats even during tiring times is incredible. They are the ones who always believed in me when I did not. Be it high school, undergrad or grad days, they kept telling me that I got it all.

# Table of Contents

<b>1</b>	<b>Introduction</b>	<b>1</b>
1.1	Motivation . . . . .	2
1.2	PEFC Basics . . . . .	3
1.2.1	Bipolar plates . . . . .	4
1.2.2	Gas diffusion layer . . . . .	5
1.2.3	Microporous layer . . . . .	7
1.2.4	Catalyst layer . . . . .	8
1.2.5	Polymer electrolyte membrane . . . . .	8
1.3	Literature Review . . . . .	9
1.3.1	Permeability . . . . .	9
1.3.2	Diffusivity . . . . .	20
1.4	Contributions . . . . .	28
1.5	Thesis Outline . . . . .	29
<b>2</b>	<b>Experimental study of in-plane mass transport properties of PEM fuel cell porous media</b>	<b>30</b>
2.1	Introduction . . . . .	30
2.2	Materials and Methods . . . . .	31
2.2.1	Experimental Setup . . . . .	31
2.2.2	Experimental Conditions . . . . .	38
2.2.3	Testing Protocol . . . . .	39
2.3	Theory and Data Analysis . . . . .	39
2.3.1	Mathematical models . . . . .	39
2.3.2	Model implementation . . . . .	43
2.4	Results and discussion . . . . .	44
2.4.1	In-plane permeability . . . . .	44
2.4.2	In-plane effective molecular diffusivity . . . . .	52
2.5	Conclusion . . . . .	60

<b>3</b>	<b>Experimental study of through-plane mass transport properties of PEM fuel cell porous media: Permeability, and Knudsen and molecular diffusivity</b>	<b>62</b>
3.1	Introduction . . . . .	62
3.2	Materials and Methods . . . . .	63
3.2.1	Experimental Setup . . . . .	63
3.2.2	Experimental Conditions . . . . .	68
3.2.3	Materials . . . . .	69
3.3	Theory and Data Analysis . . . . .	70
3.3.1	Modified binary friction model . . . . .	70
3.3.2	Model implementation . . . . .	72
3.4	Results and discussion . . . . .	74
3.4.1	Through-plane permeability . . . . .	74
3.4.2	Through-plane effective diffusivity . . . . .	80
3.5	Conclusions . . . . .	89
<b>4</b>	<b>Conclusion and Future Work</b>	<b>92</b>
4.1	Conclusion . . . . .	92
4.2	Future Work . . . . .	94
	<b>References</b>	<b>103</b>
	<b>Appendices</b>	<b>104</b>
	<b>Appendix A</b> Factory certificates of sensors	<b>104</b>

# List of Tables

1.1	The parameters $\alpha$ and $\epsilon_p$ for different flow directions and fiber structures	14
1.2	Blending techniques to estimate the effective in-plane permeability	15
1.3	Flow regimes and the corresponding Knudsen number	20
2.1	Thickness and Porosity (MIP) data of GDL samples	33
2.2	In-plane permeability for sample SGL 34BA at various angles	46
2.3	In-plane permeability for sample Toray090 (untreated)	48
2.4	Data fit for Carman-Kozeny Parameter	48
2.5	In-plane permeability for sample Toray 090 with 40 % PTFE	52
2.6	Effect of absolute pressure on diffusivity	55
2.7	In-plane diffusibility for Toray 090 (untreated) at different compression	56
3.1	Thickness and Porosity (MIP) data of GDL samples	70
3.2	Through-plane permeability for sample SGL 34BA at various aperture diameters	76
3.3	Through-plane permeability for sample SGL 34BA for various layers	77
3.4	Through-plane permeability for sample SGL 34BA and Toray 090 (0, 10, 20 and 40% PTFE)	78
3.5	Through-plane permeability and pore diameter for sample Toray 090 (10, 20 and 40 % PTFE) with MPL	80
3.6	Through-plane diffusibility for Toray 090 (0, 10, 20 and 40% PTFE)	85
3.7	Through-plane diffusibility for Toray 090 (10, 20 and 40% PTFE) with MPL	90

# List of Figures

1.1	Polarisation curve of PEFC . . . . .	3
1.2	Diagram of a PEM Fuel Cell . . . . .	4
1.3	Bipolar plate with (A) Serpentine flow channel, (B) Parallel flow channel	5
1.4	SEM image of a paper based GDL sample . . . . .	6
1.5	Pore size distribution of a Toray090 (untreated) sample . . . . .	7
1.6	SEM image of an MPL . . . . .	8
1.7	SEM image of a catalyst layer . . . . .	9
1.8	Through and in-plane direction of porous media . . . . .	10
1.9	Two bulb setup . . . . .	24
1.10	Closed tube setup . . . . .	24
1.11	Diffusion bridge setup . . . . .	25
1.12	Point source setup . . . . .	26
1.13	Evaporation tube setup . . . . .	26
2.1	Pore size distribution of Toray 090 samples with different PTFE content	33
2.2	Exploded view of in-plane diffusion bridge . . . . .	34
2.3	Experimental set-up to measure in-plane permeability . . . . .	36
2.4	Experimental set-up to measure in-plane diffusivity . . . . .	37
2.5	Experimental setup picture . . . . .	38
2.6	Oscillatory and average volume flow rate, and pressure gradient readings for a Toray 090 (untreated) sample at $262\pm 3$ thickness . . . . .	45
2.7	Inlet pressure versus molar flux curves for a Toray090 (untreated) sample at various compression levels . . . . .	47
2.8	Comparison of permeability results with Carman-Kozeny and T-S Model for SGL 34BA sample . . . . .	49
2.9	Comparison of permeability results with Carman-Kozeny and T-S Model for Toray090 (untreated) sample . . . . .	49
2.10	SEM image for Toray090 samples with (A) 0, (B) 10, (C) 20 and (D) 40% PTFE loadings . . . . .	50

2.11	Permeability results for different PTFE loadings at various thickness .	50
2.12	Permeability results for different PTFE loadings at various porosities	51
2.13	Test repeatability for a Toray 090 (untreated) sample at $262\pm 3$ thickness	53
2.14	Oscillatory and average differential pressure, and oxygen concentration readings for a Toray 090 (untreated) sample at $262\pm 3$ thickness . . .	53
2.15	Experimental data fit to Fick - Darcy model for a Toray090 (untreated) sample . . . . .	56
2.16	Diffusibility results from Fick-Darcy Model for different PTFE loadings at various porosities . . . . .	57
2.17	Diffusibility results from Fick-Darcy Model for different PTFE loadings at various thickness . . . . .	57
2.18	Estimated oxygen concentration across Toray 090 (untreated) at various differential pressure . . . . .	58
2.19	Oxygen convective flux across Toray 090 (untreated) at various differential pressure . . . . .	59
2.20	Oxygen diffusive flux across Toray 090 (untreated) at various differential pressure . . . . .	59
3.1	Exploded view of through-plane diffusion bridge . . . . .	63
3.2	Laminated GDL samples . . . . .	64
3.3	Experimental set-up to measure through-plane permeability . . . . .	65
3.4	Experimental set-up to measure through-plane diffusivity . . . . .	67
3.5	Experimental set-up . . . . .	68
3.6	Pore size distribution of GDL and GDL-MPL samples . . . . .	69
3.7	SEM of a Toray090 (20% PTFE)-MPL sample . . . . .	70
3.8	Test repeatability for a 34BA sample . . . . .	75
3.9	Oscillatory and average volume flow rate, and pressure gradient readings for a 34BA sample . . . . .	76
3.10	Inlet pressure vs molar flux for Toray 090 samples . . . . .	78
3.11	Carman-Kozeny fit to the experimental data . . . . .	79
3.12	Inlet velocity vs inlet pressure for nitrogen and helium for a Toray 090 (10% PTFE)+MPL assembly . . . . .	80
3.13	Test repeatability for a Toray 090 (10 % PTFE) sample . . . . .	81
3.14	Oscillatory and average differential pressure, and oxygen concentration readings for a Toray 090 (10% PTFE) sample . . . . .	82
3.15	Oscillatory and average differential pressure, and oxygen concentration readings for a Toray 090 (10% PTFE)+MPL sample . . . . .	82

3.16	Oxygen molar flux vs differential pressure across porous media for GDL samples . . . . .	84
3.17	Bruggemen and percolation model fit in diffusibility results . . . . .	85
3.18	Oxygen concentration across porous media at various differential pressures . . . . .	86
3.19	Oxygen convective flux across porous media at various differential pressures . . . . .	87
3.20	Oxygen diffusive flux across porous media at various differential pressures	87
3.21	Oxygen molar flux vs differential pressure across porous media for GDL+MPL samples . . . . .	88
3.22	Diffusibility comparison with and without Knudsen diffusivity . . . . .	89
A.1	Factory certificate of mass flow controller . . . . .	104
A.2	Factory certificate of back pressure controller . . . . .	105
A.3	Factory certificate of differential pressure controller . . . . .	106
A.4	Factory certificate of pressure transducer . . . . .	107
A.5	Factory certificate of oxygen sensor . . . . .	108

# Nomenclature

## English Letters

$K_{CK}$	Carman - Kozeny constant
$V_p$	Volume of the pore space
$S_p$	Surface area of the pore space
$\bar{r}$	Mean intercept half length of the porous structure
$r$	Fiber radius of the porous media
$B_v$	Viscous permeability of the porous media
$B_l$	Inertial permeability of the porous media
$D_{bulk}$	Bulk diffusivity of a pair of gases
$D_{eff}$	Effective diffusivity of the porous media
$D^K$	Knudsen diffusivity of the porous media
$D_l$	Diffusion coefficient of gas in liquid water
$F$	Formation factor of the porous media
$E(r)$	Local electric field in the pore space
$K_{norm}$	Viscous permeability of the fibers normal to the flow direction in porous media
$K_{par}$	Viscous permeability of the fibers parallel to the flow direction in porous media
$d$	Fiber diameter in porous media
$S_d$	Distance between consecutive fibers in porous media
$d_p$	Pore diameter in porous media

$K_n$	Knudsen number of a gas
$M$	Molecular weight of a gas
$a(\epsilon)$	Function to define geometry of porous media
$b(S)$	Function to define liquid water saturation in porous media
$S$	Liquid water saturation in porous media
$f_g$	Volume fraction of gas in porous media
$f_l$	Volume fraction of liquid in porous media
$V_{total}$	Total volume of the porous media
$V_i$	Intruded volume of mercury in porous media
$P_i$	Pressure at which mercury intrusion occurs
$t_o$	Thickness of porous media in uncompressed state
$t$	Thickness of porous media in compressed state
$L$	Width of the porous media
$w$	Length of the porous media
$\nabla p$	Pressure gradient across porous media
$\Delta p$	Pressure difference across porous media
$v$	Velocity of gas across porous media
$p_i$	Partial pressure of gas $i$
$R$	Gas constant
$T$	Temperature
$N$	Molar flux of gas in porous media
$n$	Mass flux of gas in porous media
$x$	Mole fraction
$P$	Absolute pressure of gas in channel

$V$  Volume flow rate of gas

### **Abbreviations**

CL Catalyst Layer

GDL Gas Diffusion Layer

MEA Membrane Electrode Assembly

MIP Mercury Intrusion Porosimetry

MPL Microporous Layer

PEM Polymer Electrolyte Membrane

PEMFC Polymer Electrolyte Membrane Fuel Cell

PSD Pore Size Distribution

PTFE Polytetrafluoroethylene

MBFM Modified Binary Friction Model

### **Greek Letters**

$\epsilon_o$  Porosity of porous media in uncompressed state

$\epsilon$  Porosity of porous media in compressed state

$\epsilon_{wet}$  Porosity of porous media in the presense of liquid water

$\epsilon_{dry}$  Porosity of porous media in the absense of liquid water

$\tau$  Tortuosity of porous media

$\Lambda$  Transport parameter from electrical conduction principles

$\epsilon_p$  Percolation threshold porosity

$\alpha$  Fitting parameter in percolation correlation

$\varphi$  Overall fiber volume fraction in porous media

$\varphi_{par}$  Parallel fiber volume fraction in porous media

$\varphi_{norm}$  Normal fiber volume fraction in porous media

$\lambda$	Mean free path of a gas
$\rho$	Density of a gas
$\sigma$	Collision diameter of a gas
$\theta$	Contact angle between mercury and porous media
$\gamma$	Surface tension of mercury
$\eta$	Dynamic viscosity of the gas
$\chi$	Factor to take account of viscous friction in MBFM
$\xi$	Lennard Jones interaction parameter

# Chapter 1

## Introduction

Energy consumption is increasing as population worldwide continues to increase. Environmental degradation from harmful gases and particulates emitted by conventional fossil fuel-based sources of energy stress the need for more sustainable energy production technologies. Over the past century, new technologies have emerged as promising alternatives to fossil fuel based energy sources such as nuclear, solar thermal energy, photo-voltaic cells, geothermal energy, wind energy, and ocean energy. Diversifying energy sources is crucial in order to meet today's energy demands while ensuring energy security and minimizing environment impact [1, 2]. Most renewable technologies such as solar energy however are variable. Therefore, it is difficult to match energy production with energy demand. Storage technologies to store large quantities of energy are needed. Chemical storage in the form of hydrogen or other non-carbon based fuels is a possible method to store large quantities of energy from intermittent energy technologies.

The transportation sector in Canada is the largest source of greenhouse gas emissions, accounting for 27% of the total [3, 4]. To reduce the environmental impact, battery or fuel cell operated vehicles can be used, replacing the conventional internal combustion engines. During recent years, polymer electrolyte fuel cells (PEFC) have proved to be efficient, minimal total emission, energy conversion devices which convert chemical energy to electricity and heat. Hydrogen is used as fuel in a PEFC which, if produced from either nuclear or renewable sources like solar, could result in a zero-emission transportation sector. In addition to the transportation sector, fuel cell are currently being used in many other applications such as backup power, forklift engines, portable electronics, power plants, and replacement of internal combustion engine [5].

## 1.1 Motivation

In order to make PEFCs competitive in commercial markets, fuel cells need to operate at higher energy efficiency and be produced at lower manufacturing costs. Tsuchiyaa and Kobayashib [6] analyzed the cost of fuel cell components in 2020 by using 'learning effects' where they estimated the cost of a fuel cell considering the development of technology in future. The overall cost is estimated at \$38/kW under the assumption of 5 million fuel cell vehicles being used by 2020. Electrode and bipolar plates sum up much of the fuel cell cost. Platinum uses 9.8% of the total cost of manufacturing.

The US department of energy estimated the cost of an operating fuel cell at \$124/kW in 2006, which reduced to \$55/kW in 2013. The target cost for mass production in 2020 is set at \$40/kW. The reduction in cost over the past years was associated to the development of durable membrane electrode assemblies, low platinum group metal content, enhanced durability, advanced manufacturing methods and materials that decreased the manufacturing of gas diffusion layers by 50% since 2008.

To reduce fuel cell cost, two options are available:

1. Increase the amount of power produced for the same cell
2. Reduce amount of platinum per cell

Fuel cell performance with the same amount of catalyst or less can be achieved by improving the mass transport properties of different PEFC layers so that the cell can run at higher current densities. Figure 1.1 shows the polarization curve for a PEFC. The three major losses that are observed in PEFC are kinetics, ohmic and mass transport losses. At high current density, the rate of reactant consumption becomes higher than supply. This is known as the limiting current density. In order to increase the limiting current density, transport in each layer must be analyzed.

The PEFC layers, through which gas transportation takes place, are the gas diffusion layer (GDL), micro porous layer (MPL) and catalyst layer (CL) at both cathode and anode side. The gas diffusion layers are known to be anisotropic in nature, hence it is important to measure gas transport in different directions.

The motivation of this thesis is to analyze and experimentally determine the effective transport properties, viz. permeability, effective diffusivity and Knudsen diffu-

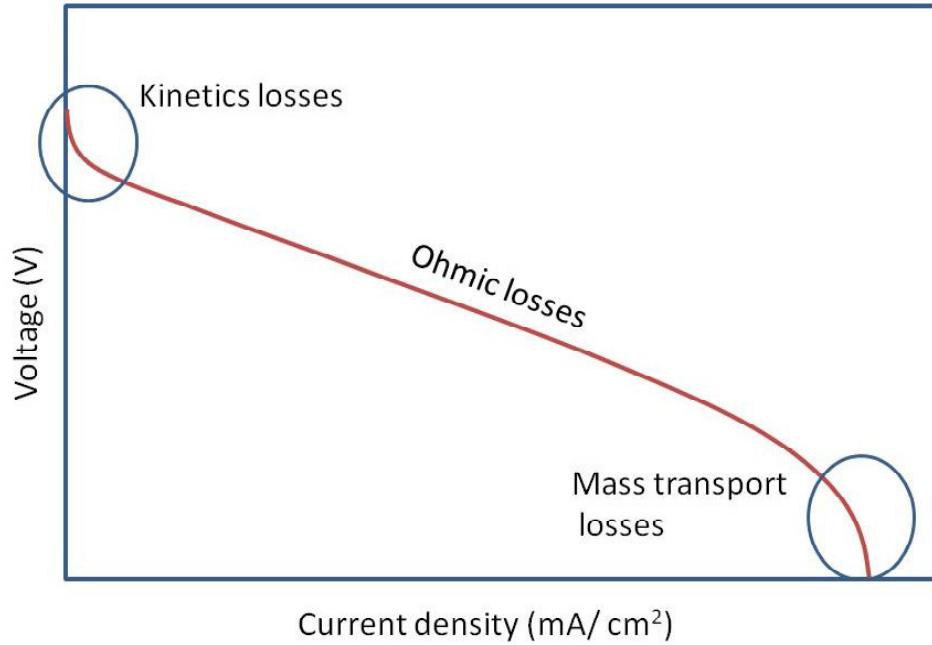


**Figure 1.1** – Polarisation curve of PEFC

sivity of PEFC layers. These values can then be used in mass transport mathematical models for modelling and optimization of fuel cells [7, 8]. The models used in the literature to estimate the transport properties are inadequate in certain cases. In this thesis, correct models are implemented to measure the more accurate transport parameter.

## 1.2 PEFC Basics

A PEFC is an electrochemical device that convert the chemical energy of a fuel, commonly hydrogen, and oxygen, into electricity and heat. During the process, it emits zero particulates,  $SO_x$ ,  $NO_x$  and other greenhouse gases. A fuel cell is made up of cathode and anode electrodes. The cathode is where the reduction reaction (electron consuming) takes place. The anode is where the oxidation reaction (electron producing) takes place. Hydrogen is supplied at the anode. It is then transported through GDL and MPL and gets oxidized at the catalyst layer (CL). The oxygen is introduced at the cathode. At the cathode catalyst layer (CCL), it combines with

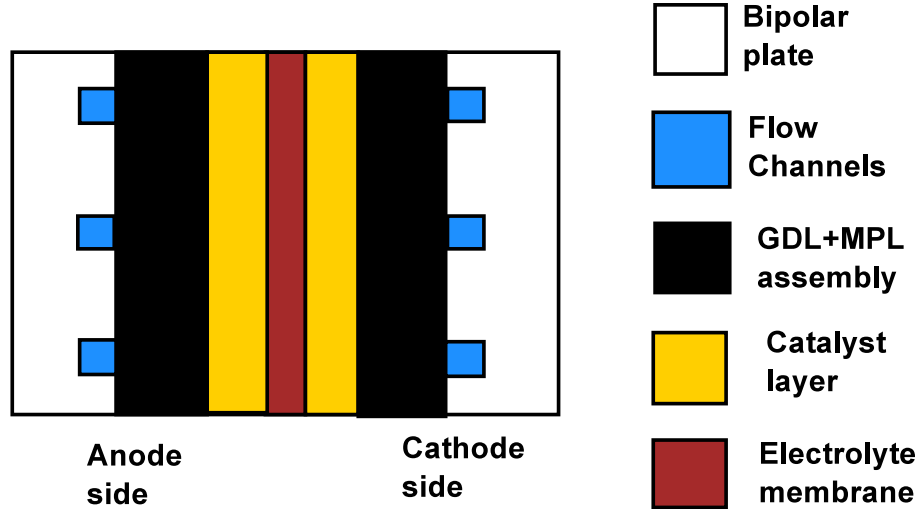
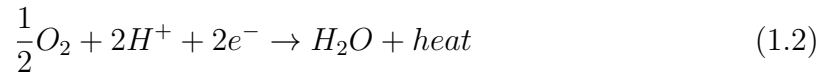


Figure 1.2 – Diagram of a PEM Fuel Cell

protons and electrons, and water is produced . The electrochemical reactions at anode and cathode are:



To get the overall chemical reaction, equations (1.1) and (1.2) are added:



Therefore, in an overall reaction, hydrogen and oxygen reacts to produce water and heat.

Figure 1.2 shows the diagram of a fuel cell with its different layers. Each component of the fuel cell has different functions. The following subsections discuss each of them.

### 1.2.1 Bipolar plates

The bipolar plates, also known as current collectors, are installed at the ends of the cell with gas flow channels machined into them. Figure 1.3 shows a picture of the bipolar plate with serpentine, and parallel flow channels machined into it. The plates are made up of conduction materials like graphite or metals to conduct the electrons and heat. The bipolar plates have many essential functions in a fuel cell stack such as reactant supply to the cell active area, current collection, mechanical support to the

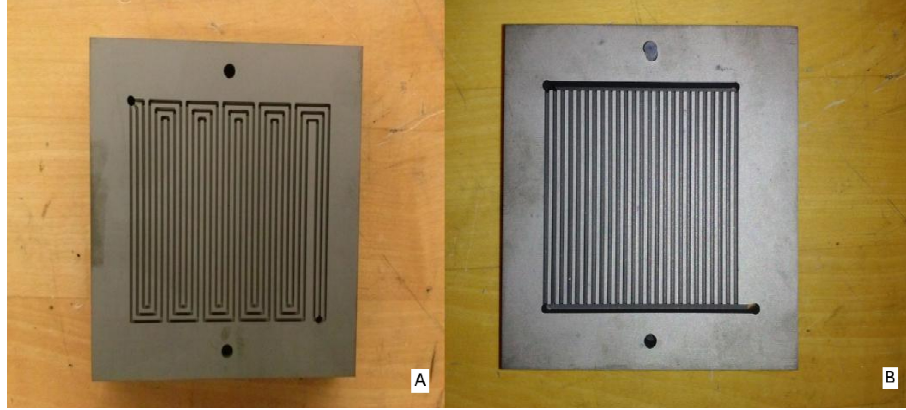


**Figure 1.3** – Bipolar plate with (A) Serpentine flow channel, (B) Parallel flow channel

MEA, water management and heat management [9]. The electrons that are produced at the anode catalyst layer (ACL) are passed from catalyst layer, through GDL, to the bipolar plate. The electrons flow from the bipolar plate through an applied load, doing electrical work before arriving at the cathode.

Many channel geometries are available in the literature. Depending on the application, a specific channel geometry is selected. Some available channel geometries are pin-type flow field, series-parallel flow field, serpentine flow field, integrated flow fields, and interdigitated flow field [9]. The major gas flow direction at cathode and anode is parallel to its corresponding electrode surface [10]. Most commonly, either serpentine or parallel flow fields are employed in PEFC applications.

### 1.2.2 Gas diffusion layer

Gas diffusion layers (GDLs) are attached adjacent to bipolar plates at both cathode and anode side. The GDLs are made porous to allow the reactants to reach to the reaction sites. Figure 1.4 shows a SEM image of a Toray090 (untreated) sample. The porosity,  $\epsilon_o$ , of a GDL is defined as the ratio of the volume of available pores to the total volume of the sample. Mathematically,

$$\epsilon_o = \frac{V_{pore}}{V_{total}} \quad (1.4)$$

GDLs are assumed to have a random distribution of pores of different radius, known as pore size distribution. The pore size distribution of a sample is often measured using a Mercury Intrusion Porosimeter (MIP). MIP uses mercury to intrude into the pores, depending upon the pressure required for intrusion, radius of the pore is estimated using Washburn equation. Pore size distribution relates the change in

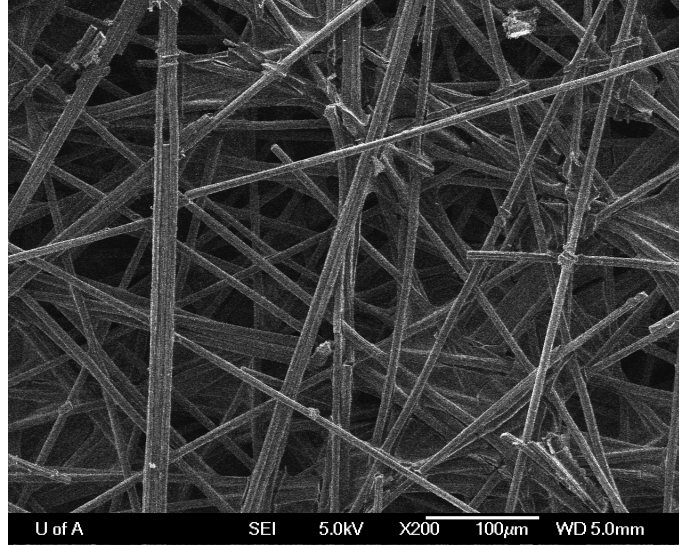


**Figure 1.4** – SEM image of a paper based GDL sample

cumulative volume of mercury with an effective pore radius. Figure 1.5 shows a pore size distribution for a GDL (Toray090 (untreated)) sample measured using a MIP.  $\frac{DX}{D(\ln(r))}$  is plotted with respect to pore radius to produce the pore size distribution curve, where  $X$  is the cumulative pore volume fraction, and  $r$  is the radius of the pore. The peak in the figure represents that most of the pores are about 15-20  $\mu\text{m}$  in size. A more detailed discussion on MIP measurements is shown in Chapter 2, section 2.2.1.1.

The GDL is best described as a carbon-carbon composite since after heat treatment it consists of carbon fibers of around  $7\mu\text{m}$  diameter held together by a carbon matrix [11]. The carbon matrix, which holds the fibers together, is usually referred to as binder and it makes up to 5-15% of the total weight of the final product. The manufacturing process of carbon paper consists of various stages of heat treatment (carbonization and graphitization). While the fibers possess graphite like quantities, the resin-based portion (mostly the binder) of the composite does not graphitize and remains as amorphous carbon [11]. The structure of carbon paper is highly anisotropic since carbonization and graphitization are typically achieved by stacking many sheets or layers of carbon fibers in a horizontal or vertical batch furnace [10]. The GDLs are often treated with a hydrophobic agent called polytetrafluoroethylene (PTFE) to facilitate the liquid water management and avoid water accumulation in the pores, i.e. flooding.

Common available GDLs are carbon cloth and carbon paper. Even though carbon cloth type GDLs provide better permeability and diffusivity properties, its difficult to

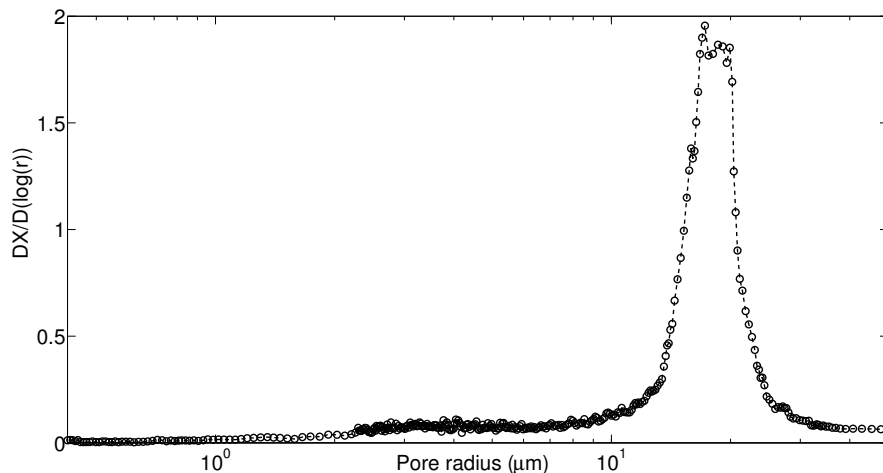


**Figure 1.5** – Pore size distribution of a Toray090 (untreated) sample

sparry an MPL on them, hence, paper based layers are more widely used in PEFCs [12]. The thickness of different type of GDLs have been reported in the range of 192 - 415  $\mu\text{m}$  [13–16].

### 1.2.3 Microporous layer

The microporous layer (MPL) is often sprayed on a GDL to facilitate the liquid water transport through GDL, an issue important especially for cathode side. The MPLs are made of carbon black powder and PTFE. An ink made of carbon black, PTFE and solvents is either painted or sprayed onto the GDL and sintered so that the PTFE binds the carbon powder together. Figure 1.6 shows a SEM image of an MPL. The MPL thickness has been reported in the range of 38.4 - 66.4  $\mu\text{m}$  [16].

The MPLs have a high PTFE content, i.e., around 30% by weight [17]. The MPL consists of carbon agglomerates, and has a pore size distribution around nm in size. Hence, the capillary pressure increases compared to the GDL. This results in improved water removal which increases the PEM fuel cell performance [18].

The MPL reduces ohmic losses by enhancing the hydration of electrolyte membrane, and improving the electrical contact between GDL and CL. The MPL also enhances the chemical and mechanical stability of the CL and membrane since without MPL, the GDL might intrude in the CL and block reaction sites [19].

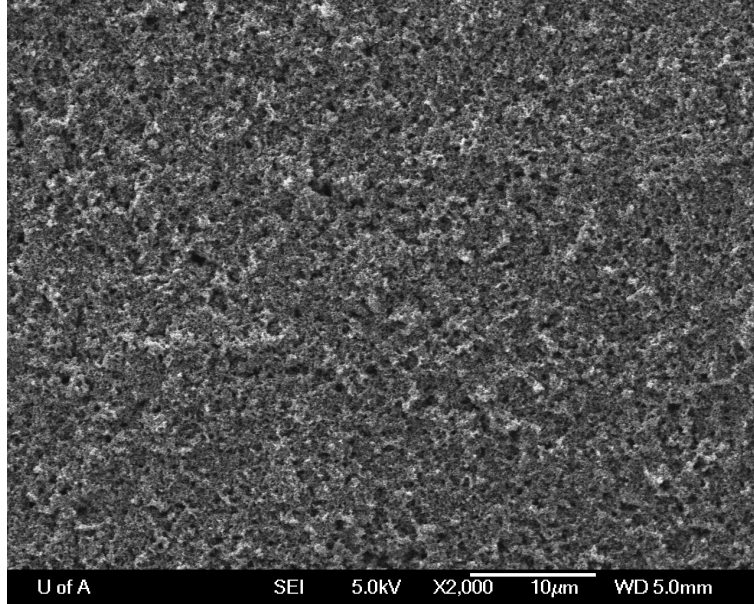


**Figure 1.6** – SEM image of an MPL

#### 1.2.4 Catalyst layer

Catalyst layers (CLs) are generally either painted or sprayed on the electrolyte membrane at both cathode and anode side. The catalyst layer consists of ionomer (usually nafion), Pt catalyzed carbon agglomerates, and void region with the reaction occurring at the surface of the Pt particles [20]. The structure of the CL is believed to have catalyzed carbon agglomerates bound by ionomer, where the platinum particles are supported on carbon particles [21]. Figure 1.7 shows a side view of the catalyst layer printed on a membrane. The pore size distribution of catalyst layers have been reported in the range of 10 to 200 nm [22]. The peak pore size was reported at about 50 nm. The thickness of the catalyst layer is in between 10 [23] and 60 [22]  $\mu\text{m}$ , however ultra-thin electrodes have recently been studied [24].

The carbon enhance the transport of electrons from the reaction site to the bipolar plates while the void region helps to transport the water and reactants.

#### 1.2.5 Polymer electrolyte membrane

The electrolyte membrane is situated between the catalyst layers. The membrane is made up of nafion, which is a sulfonated tetrafluoroethylene polymer [25]. The membrane acts as a proton conductor and electron insulator, helps to transport the protons to the cathode side and hinders the electrons, forcing them to go through an external circuit. The membrane must be able to act as a barrier for reactant cross

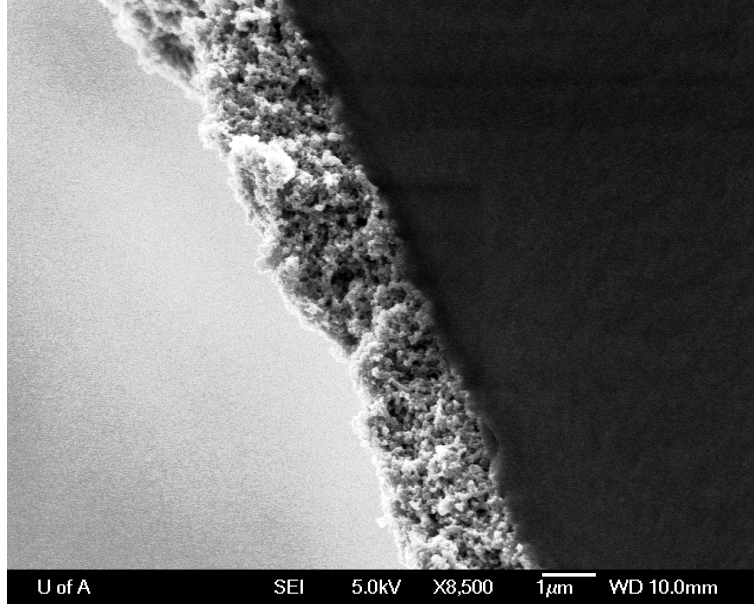


**Figure 1.7** – SEM image of a catalyst layer

over from anode to cathode or vice versa, suggesting a low diffusion coefficient is required for membrane [10].

The fuel cell components discussed above have a direct influence on transport of reactants, products, electrons, and protons. Hence, it is important to study the transport parameters of each one of them. This thesis focuses only on the transport of gases, hence the gas transport parameters, i.e. permeability, Knudsen diffusivity and effective diffusivity, are the only significant parameters to study. The next section discusses about the existing experimental and modelling studies of gas transport parameters in literature.

## 1.3 Literature Review

### 1.3.1 Permeability

In the past decade, many researchers have studied the role of permeability in fuel cell gas transport. Many studies are available for GDLs in literature. As discussed in section 1.2.2, the GDLs are known to be anisotropic in nature. Hence, the GDLs should be tested in different directions. GDLs are generally tested in two perpendicular directions, known as through, and in plane direction. The through plane direction align with the thickness of a GDL while in plane direction is perpendicular to the through plane direction. Figure 1.8 shows the two directions of porous media. Even

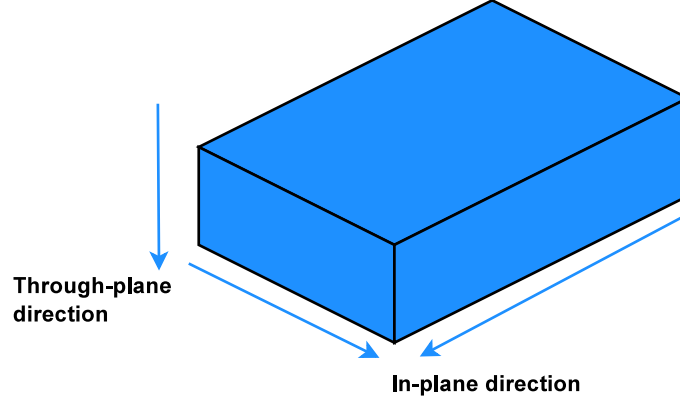


**Figure 1.8** – Through and in-plane direction of porous media

though the MPL and CL play a significant role in gas transport, the permeability has yet not been reported for them because, due to their thin nature, it is challenging to fabricate and test them individually. Only the effect of an MPL on GDL is studied by testing or modelling them together.

Diffusion is considered to be the primary mode of transport in the through plane direction. Depending on bipolar plate geometry both diffusion and convection mass transport occurs in the in-plane direction [15]. In-plane convective transport is particularly important for serpentine channels due to the significant pressure drop between neighbouring channels. Pharoah [26] studied the anisotropic nature of diffusion layers computationally. Results showed that more than 80% of the flow remained in the channels if the GDL isotropic permeability was less than  $10^{-11} m^2$ , and almost impermeable for permeability less than  $10^{-12} m^2$ . At a fix Reynolds number and channel length, pressure drop required to drive the flow reduced by almost 40% if in-plane permeability increased from  $10^{-11}$  to  $10^{-10} m^2$ . Therefore, the in-plane permeability plays a significant role for pressure driven flows.

Pharoah et al. [27] used Bruggeman, and, isotropic and anisotropic percolation models to study the current distribution at the membrane-catalyst interface for two different load conditions. The current distribution under the channels is virtually unchanged while current distribution varied significantly under the land at both load conditions. The maximum difference under land was found at 8% and 16% at lower and higher load, respectively. Results showed that onset of limiting current occurs sooner for the isotropic case than the anisotropic case since through plane conductivity is higher than in plane conductivity, hence overall conductivity is underestimated in isotropic case.

The above discussion show that GDLs are anisotropic in nature, hence the transport properties should be measured in both in-plane and through-plane directions. However, most reported values in literature are in through-plane direction due to the incorrect perception that permeability of GDLs are isotropic [28]. Another reason behind this perception is the ease in measuring the parameters in through-plane direction [26].

### 1.3.1.1 Mathematical prediction of permeability

In the creeping flow regime, viscous interactions between the flow and the porous media contributes to the pressure drop of the flow. Permeability is the measurement of geometric nature of the porous media that directly affects the pressure loss. For sufficiently low velocities, Darcy's law is commonly used to estimate permeability:

$$\nabla p = -\frac{\eta}{B_v}v, \quad (1.5)$$

where  $\nabla p$  is the pressure gradient across porous media,  $v$  is the velocity,  $\eta$  is the dynamic viscosity and  $B_v$  is the porous media permeability.

At higher velocities, additional pressure loss is incurred as flow travels through the tortuous path of the porous media [14]. This is known as Forcheimer effect. In such cases, Darcy's law is modified to include the Forcheimer effect [14]:

$$\nabla p = -\frac{\eta}{B_v}v - \frac{\rho}{B_l}v^2, \quad (1.6)$$

where  $B_l$  is known as the inertial permeability.

The accurate prediction of permeability has always been a subject of interest for researchers in the area of mathematical modelling. Many attempts have been made to predict the permeability of GDLs. The widely accepted model for permeability is the Carman - Kozeny relation [29]:

$$B_v = \frac{\epsilon}{K_{CK}} \left( \frac{V_p}{S_p} \right)^2 = \frac{\epsilon \bar{r}^2}{4K_{CK}} = \frac{\epsilon \bar{r}^2}{8\tau} \quad (1.7)$$

where  $\epsilon$ ,  $V_p$ , and  $S_p$  are the porosity, total volume, and surface area of the pore space,

respectively,  $K_{CK}$  is the Carman - Kozeny constant,  $\bar{r}$  is the mean intercept half - length of the porous structure, a measure of the average of pore radius, and  $\tau$  is the tortuosity factor, related with Carman - Kozeny constant as  $K_{CK} = 2\tau$ . The mean intercept length of randomly overlapping fiber structures is given as [30]:

$$\bar{r} = \frac{-r}{\ln(\epsilon)} \quad (1.8)$$

where  $r$  is the fiber radius. After substituting in equation (1.7), the permeability is given as:

$$B_v = \frac{\epsilon r^2}{4K_{CK}[\ln(\epsilon)]^2} \quad (1.9)$$

For random non-overlapping fibers, the mean intercept length is given as [31]:

$$\bar{r} = \frac{\epsilon r}{1 - \epsilon} \quad (1.10)$$

Again substituting in equation (1.7), the permeability becomes:

$$B_v = \frac{\epsilon^3 r^2}{4K_{CK}(1 - \epsilon)^2} \quad (1.11)$$

Johnson et al. [32] proposed a transport parameter,  $\Lambda$ , to link to the permeability. The equation is based on an analogy of the electrical conduction principles. The permeability is then,

$$B_v = \frac{\Lambda^2}{8F} \quad (1.12)$$

where  $\Lambda$  is defined as,

$$\frac{\Lambda}{2} = \frac{\int |E(r)|^2 dV_p}{\int |E(r)|^2 dS_p} \quad (1.13)$$

where  $E(r)$  is the local electric field, integrated over pore volume and surface area, and  $F$  is the formation factor, defined as the ratio of bulk to effective molecular

diffusivity of porous media. Johnson et al. [32] modified equation (1.13) by including the formation factor as:

$$\frac{2}{\Lambda} = -\frac{S_p}{V_p} \frac{d \log F}{d \log \epsilon} \quad (1.14)$$

Substituting  $\frac{V_p}{S_p} = \frac{\bar{r}}{2}$ , equation (1.14) results in:

$$\Lambda = -\bar{r} \left( \frac{d \log F}{d \log \epsilon} \right)^{-1} \quad (1.15)$$

Tomadakis and Sotirchos [33] used random walk simulation results to relate the tortuosity with the percolation threshold  $\epsilon_p$  of randomly overlapping fiber structures as:

$$\tau = \left( \frac{1 - \epsilon_p}{\epsilon - \epsilon_p} \right)^\alpha \quad (1.16)$$

The tortuosity, porosity and formation factor are related as [34]:

$$F = \frac{\tau}{\epsilon} \quad (1.17)$$

Equations (1.16) and (1.17) are substituted in equation (1.15) to find the final permeability function as [29]:

$$B_v = \frac{\epsilon}{8(\log \epsilon)^2} \frac{r^2(\epsilon - \epsilon_p)^{\alpha+2}}{(1 - \epsilon_p)^\alpha [(1 + \alpha)\epsilon - \epsilon_p]^2} \quad (1.18)$$

The estimated parameters  $\alpha$  and  $\epsilon_p$  for different flow directions and fiber structures are given in Table 1.1 [29].

Equations (1.11) and (1.18) are the widely accepted models to predict the permeability of the porous media. Feser et al. [15] performed in-plane permeability experiments for SGL 31BA and TGP-60-H samples at different compression levels or porosity levels, and used results to fit equation (1.11) to extract the Carman-Kozeny constant. A similar study was done by Gostick et al. [14] for various carbon cloth and fiber based samples. The fitting is done for samples cut in two perpendicular directions in the plane of the paper. The Carman-Kozeny parameter,  $K_{CK}$  was estimated in the range of 1.446 - 43.5.

**Table 1.1** – The parameters  $\alpha$  and  $\epsilon_p$  for different flow directions and fiber structures

Structure	Flow	$\epsilon_p$	$\alpha$
1-d	Parallel to fibers	0	0
1-d	Perpendicular to fibers	0.33	0.707
2-d	Parallel to fibers	0.11	0.521
2-d	Perpendicular to fibers	0.11	0.785
3-d	All directions	0.037	0.661

Tamayol et al. [35] proposed a blending approach to predict the in-plane permeability. First, models were developed assuming flow being parallel and perpendicular to the fiber alignment. Then, different blending techniques were used to find the best model fit in the experimental data.

For unidirectional fibers, a parabolic velocity profile is assumed within square arrangement of equally sized fibers. Continuity and momentum equations are integrated to form the analytical solution for parallel and normal permeability as [35]:

$$K_{norm} = \left[ \frac{12(\sqrt{\varphi'} - 1)}{\varphi' \sqrt{\varphi'}} \left( \frac{2 - g(\epsilon)}{2} \right) + \frac{18 + 12(\varphi' - 1)}{\sqrt{\varphi'(1 - \varphi')^2}} + \frac{18\sqrt{\varphi'} \left( \tan^{-1} \left( \frac{1}{\sqrt{\varphi' - 1}} \right) + \frac{\pi}{2} \right)}{(\varphi' - 1)^{5/2}} \right]^{-1} d^2 \quad (1.19)$$

where  $\varphi' = \frac{\pi}{4(1 - \epsilon)}$ ,  $g(\epsilon) = 1.274\epsilon - 0.274$

$$K_{par} = \frac{d^2}{16\varphi} \left[ -1.479 - \log\varphi + 2\varphi - \frac{\varphi^2}{2} - 0.0186\varphi^4 \right] \quad (1.20)$$

where  $\varphi$  is the fiber volume fraction and  $\epsilon$  is the porosity of the porous media.

The fiber volume fraction and porosity are related as,  $\varphi = 1 - \epsilon$ . The fiber volume fraction of parallel and normal fibers are assumed to be equal and half of the total fiber volume fraction, i.e.,  $\varphi_{par} = \varphi_{norm} = \varphi_{tot}/2$ . The porosity of the media is defined as [35]:

$$\epsilon = 1 - \frac{\pi d}{4 S_d} \quad (1.21)$$

where  $d$  is the fiber diameter and  $S_d$  is the space between two consecutive fibers.

A number of blending techniques are proposed to blend the normal and parallel permeabilities calculated using equations (1.19) and (1.20) to find the overall effective permeability of the porous media. Table 1.2 shows the proposed techniques [35].

**Table 1.2** – Blending techniques to estimate the effective in-plane permeability

Blending Model	Relationship
Volume-weighted resistivity	$\frac{1}{K_{eq}(\varphi)} = \frac{\varphi_{par}}{\varphi} \frac{1}{K_{par}(\varphi)} + \frac{\varphi_{norm}}{\varphi} \frac{1}{K_{norm}(\varphi)}$
Unweighted resistivity	$\frac{1}{K_{eq}(\varphi)} = \frac{1}{K_{par}(\varphi_{par})} + \frac{1}{K_{norm}(\varphi_{norm})}$
Volume-weighted permeability	$K_{eq}(\varphi) = \frac{\varphi_{par}}{\varphi} K_{par}(\varphi) + \frac{\varphi_{norm}}{\varphi} K_{norm}(\varphi)$
Geometric mean	$K_{eq}(\varphi) = (K_{par}(\varphi))^{\varphi_{par}/\varphi} + (K_{norm}(\varphi))^{\varphi_{norm}/\varphi}$

The blending techniques showed in Table 1.2 were fit in the experimental data available in literature, analysis showed that volume weighted permeability model best agreed with the data. The volume weighted permeability model is used to find the overall permeability, and in simplified form, given as [35]:

$$B_v = \exp\left(\frac{-12.95 + 13.9\epsilon}{1 + 1.57\epsilon - 2.22\epsilon^2}\right) d^2 \quad (1.22)$$

The same analysis was done for 3-D fibrous structures with fibers having random distribution and orientation. In the 3-D case, 1/3 of fibers were assumed in parallel and 2/3 perpendicular to the flow, i.e.,  $\varphi_{par} = \varphi_{tot}/3$  and  $\varphi_{norm} = 2\varphi_{tot}/3$ . The volume-weighted resistivity blending technique showed the best agreement with the data, the equation in simplest form is given as [35]:

$$B_v = \exp\left(\frac{-43.25 + 46.6\epsilon}{1 + 10.56\epsilon - 10.5\epsilon^2}\right) d^2 \quad (1.23)$$

### 1.3.1.2 Experimental studies of permeability

Apart from the simulations and modelling studies discussed above, many researchers have studied the anisotropic permeability of the porous media experimentally. Different experimental setups have been proposed to measure the permeability in different

directions. Gostick et al. [14] measured the permeability for fiber and cloth type samples in 3 orthogonal directions, where two perpendicular directions were chosen in in-plane direction of the paper while the third was the through plane direction. To measure in-plane permeability, air was flowed in an inlet header, passed through the sample, and exhausted to the ambient via an outlet header. The pressure drop was measured across the sample, and the flow rate at the outlet header was measured using a volumetric flow meter. Through plane permeability was measured by installing a circular GDL sample in between two plates. Air is introduced at different flow rates and pressure drop is measured across the sample. In-plane permeability was measured at different compressions and found to decrease as compression increases. Permeability was measured in the range of  $4 \times 10^{-13}$  to  $4 \times 10^{-11}$  m<sup>2</sup>, and  $5.7 \times 10^{-12}$  to  $69.4 \times 10^{-12}$  m<sup>2</sup> for in plane and through plane direction, respectively. Permeability for cloth type GDL was estimated an order higher than fiber based samples

Hussaini et al. [36] measured the in-plane and through-plane permeability for fibrous and cloth type carbon papers. A test rig was implemented for measurement in both directions. During in plane measurements, a circular sample was cut of 12.7 mm diameter. The sample was secured in a donut shaped Teflon gasket and flanked between two identical upstream and downstream cups made of polycarbonate. Cylindrical pieces of porous plastic were inserted into those cups to provide support to the GDL samples. Pressure probes were inserted into the porous plastic to measure pressure drop across the sample at various velocities. To measure the through plane permeability, the same methodology was used except the flow was made to travel in the in-plane direction of the sample by blocking the inlet channel from the other end. Results showed permeability for cloth type to be higher than fibrous in both directions, and measured in the range of  $11.5 \times 10^{-12}$  to  $37.2 \times 10^{-12}$  m<sup>2</sup>, and  $12.4 \times 10^{-12}$  to  $64.6 \times 10^{-12}$  m<sup>2</sup> for in plane and through plane direction, respectively.

As discussed in sections 1.2.2 and 1.2.3, the GDL is often treated with PTFE and coated with an MPL to facilitate liquid water transport. Lobato et al. [37] studied the effect of PTFE on through plane permeability in Toray graphite paper (TGP-H-120) with 0, 10, 20 and 40% PTFE. To measure the permeability, air was flowed through the sample and pressure drop was measured with a water column. The permeability was measured to decrease from  $9.21 \times 10^{-12}$  at 0% PTFE to  $3.46 \times 10^{-12}$  m<sup>2</sup> at 40% PTFE. Lobato et al. [37] also studied the polarization curves at different PTFE loadings and found that performance was similar in the kinetics region. In ohmic region, performance was slightly poor as PTFE content increased due to the additional

ohmic resistance offered by PTFE particles. At high current densities, i.e., in the mass transport region, the differences became more notable as high PTFE content decreased the permeability and diffusivity hence creating an early onset of limiting current. Lobato et al. [37] suggests 10% PTFE as the optimized Teflon content since it does not significantly affect the transport properties compared to 0% but inclusion of this level of Teflon gives better mechanical support.

Prasanna et al. [38] studied the polarization curves with GDLs loaded with different PTFE content. They found the optimized performance at 20% Teflon content, and suggested the inefficient water removal for low PTFE, and, low permeability and diffusivity at high PTFE content. Prasanna et al. [38] also studied the effect of GDL thickness on the cell performance with PTFE content fixed at 20%. Thickness of the GDL was tested at 108, 175, 290, and 386  $\mu\text{m}$ . The thickness of 175  $\mu\text{m}$  showed the optimum performance. Thinner GDL was found more vulnerable to water flooding. As thickness increases, effect of water condensation becomes profound thereby hinders the transport of reactants.

Tamayol et al. [39] studied the effect of PTFE on through plane permeability using an air permeability test bed. The high pressure air was supplied from an air tank, and controlled using a digital air pressure regulator. The output pressure of the regulator was fixed at 6 psi. The sample was fixed in between two aluminium plates, machined and drilled with a 25 mm diameter hole. The pressure drop across the sample was measured using a pressure transducer, and flow rate was measured downstream using a flow meter. The PTFE content was varied in Toray-H-120 carbon paper. The permeability was found to decrease with PTFE.

Ismail et al. [40] also studied the effect of PTFE on through plane permeability by fixing a GDL sample in between upstream and downstream fixtures. Air was flowed through the sample at a fixed rate and the resulting pressure drop was measured. The PTFE content was varied from 0 to 30% in SGL 10 series samples. The permeability was measured to vary from  $2.72 \times 10^{-11} \text{ m}^2$  at 5% PTFE to  $2.19 \times 10^{-11} \text{ m}^2$  at 20% PTFE. The results made no particular trend with PTFE content.

Gurau et al. [41] studied the effect of PTFE and MPL on through plane permeability with a cloth type carbon substrate. A sample was clamped between an upstream and downstream fixture, each of them containing a cylindrical and an annular compartment. Nitrogen was introduced in the annular compartment of upstream fixture,

and forced through the GDL sample into the compartments of the downstream fixture. Pressure differential gages were used to measure the pressure drop across the sample, and a rotameter was used to measure the flow rate downstream. The PTFE content was kept at 30 and 70% in GDL + MPL sample. The permeability was measured in the range of  $0.44 \times 10^{-12}$  to  $8.5 \times 10^{-12}$  m<sup>2</sup> for GDL-MPL entity, while permeability for substrate alone was measured as  $13 \times 10^{-12}$  m<sup>2</sup>. The permeability was found to increase by one order with high PTFE content. The permeability for substrate alone was also an order of magnitude higher than a GDL + MPL assembly.

Similar results were also found by Ismail et al. [13, 28]. Through plane permeability was measured using the same technique adopted by Ismail et al. [40]. To measure in plane permeability, the sample was secured between two steel plates. High pressure air was first made available to a mass flow controller, and then entered in the inlet chamber. The inlet and outlet chambers are separated by a GDL sample. As the air passed from inlet to outlet chamber via GDL, pressure drop across the sample is measured using a differential pressure sensor. The thickness of the sample was controlled using a feeler gauge placed at the edges of the steel plates. The experiments were done on SGL 10 series samples. The in-plane permeability was measured in the order of  $10^{-12}$  -  $10^{-11}$  m<sup>2</sup>, and through plane permeability was measured in the order of  $10^{-13}$  m<sup>2</sup>. They measured higher through plane [13] and in-plane permeability [28] at higher PTFE content in the presence of an MPL. The results were explained using the findings of Uchida et al. [42] that carbon powder - PTFE mixture consists of carbon grains which in turn form larger agglomerates. The primary pores of size 20-40 nm existed in between carbon grains, and secondary pores of size 40-1000 nm existed in between carbon agglomerates. As PTFE increases, it mostly blocked the large secondary pores which effectively increased the agglomerates size, and in turn increased the size of the secondary pores. Therefore, increasing PTFE increased the porosity in a GDL-MPL sample.

Park et al. [43] studied the effect of PTFE and MPL on cell performance by analyzing the polarization curves. The performance of the cell became stable and enhanced in the presence of an MPL. The driving force of water removal from catalyst layer to GDL was found to be the capillary force but within the GDL the driving force was shown to be either, shear force or evaporation.

Williams et al. [44] measured the through-plane permeability of bare carbon paper, with and without an MPL. Nitrogen was made available to an inlet flow channel,

forced through the sample, and passed to an outlet channel. The outlet channel is connected to a flow meter to measure the flow rate before the gas is exhausted to ambient. The pressure difference between the channels is measured by a differential pressure gauge. The through plane permeability decreased from  $8.7 \times 10^{-12}$  for a TGP-H-120 carbon paper to  $0.7 \times 10^{-13} \text{ m}^2$  with an MPL. Similarly, permeability decreased from  $3.1 \times 10^{-11}$  to  $5.8 \times 10^{-13} \text{ m}^2$  as the sample changed from SGL 10BA (bare paper) to SGL 10BB (with an MPL).

Ihonen et al. [45] measured through and in-plane permeability for carbon paper (SGL 10BA) with and without MPL. To measure permeability, annulus shaped GDL sample was compressed between current collector. Air was fed to a cell at a controlled rate, and the pressure loss between gas inlet and outlet was measured with a manometer. The in-plane permeability decreased from  $3.3 \times 10^{-11}$  to  $2.2 \times 10^{-11} \text{ m}^2$ , while through-plane permeability decreased from  $1.8 \times 10^{-11}$  to  $3.3 \times 10^{-13} \text{ m}^2$  in the presence of an MPL.

None of the studies discussed above for an GDL+MPL assembly considered Knudsen slip. However, Carrigy et al. [46] noted that Knudsen slip is significant in the presence of an MPL. Due to the small pore size of an MPL (10 - 100 nm), the flow no longer belongs to the continuum regime. Knudsen number is used to know the validity of continuum approach. Depending on the Knudsen number, the flow can be defined in different regimes. Mathematically, Knudsen number is defined as:

$$K_n = \frac{\lambda}{d_p} \quad (1.24)$$

where  $\lambda$  is the mean free path of the gas and  $d_p$  is the average pore diameter of porous media. Mean free path for a gas is mathematically defined as [47]:

$$\lambda = \frac{M}{\pi \rho \sigma^2 \sqrt{2}} \quad (1.25)$$

where  $M$  is the molecular mass of the gas,  $\rho$  is the density and  $\sigma$  is the collision diameter. The flow regime in which a gas belongs is decided by its Knudsen number. Table 1.3 [48] shows the different flow regimes and the range of corresponding Knudsen number.

Recently Carrigy et al. [46] studied the effect of PTFE in a GDL+MPL assembly on through plane permeability considering Knudsen slip. Contrary to the results dis-

**Table 1.3** – Flow regimes and the corresponding Knudsen number

Knudsen number	Flow regime
$K_n < 0.001$	The continuum regime where molecule - molecule collisions predominate
$0.001 < K_n < 0.1$	Slip flow exists, fluid velocity on the wall differs from wall velocity
$0.1 < K_n < 10$	The transition regime where both diffusion types occur simultaneously
$K_n > 10$	The Knudsen regime where molecule - wall collisions predominate

cussed above, permeability was measured to decrease with high PTFE as the average pore diameter also decreased. Pant et al. [49] also measured the Knudsen slip to be significant for a GDL+MPL assembly.

### 1.3.2 Diffusivity

Diffusion is the primary gas transport mode in the porous media of fuel cells [15]. In-plane diffusion is responsible for providing a uniform reactant distribution under the land area of the bipolar plate and through plane diffusion is responsible for providing enough reactant to the reaction side. It is important to study the diffusion of gases in both directions.

#### 1.3.2.1 Mathematical modelling of diffusivity

Many attempts have been made to develop models to predict the effective diffusion coefficient ( $D_{eff}$ ) of porous media. The effective diffusion coefficient is considered to be a product of the bulk diffusion coefficient between a pair of gases and functions to link with the geometry and liquid water saturation of porous media, i.e.,

$$D_{eff} = D_{bulk}a(\epsilon)b(S) \quad (1.26)$$

where  $a(\epsilon)$  and  $b(S)$  are the unknown functions which define the impact of the porous and tortuous geometry, and the impact of liquid water saturation on diffusion,  $S$  is the saturation in the porous media,  $\epsilon$  is the porosity, and  $D_{bulk}$  is the bulk diffusivity of a pair of gases.

Many correlations are available in literature to define  $a(\epsilon)$  and  $b(S)$ . Bruggeman correlation [50] is a widely used model in PEM fuel cells diffusion media. The correlation was derived using the effective medium approximation. Bruggeman correlation

was derived for electrical conductivity and dielectric constant of a medium composed of uniformly distributed spheres [10]. Mathematically, the model is defined as

$$D_{eff} = D_{bulk}(\epsilon)^{1.5}(1 - S)^{1.5} \quad (1.27)$$

Though, equation (1.27) is widely used for porous media, recently, it has been experimentally proved that the correlation overpredicts the diffusivity by a factor of 3-4 in the through plane direction.

The effective medium approximation is also implemented by Neale and Nadar [51] to develop an analytical expression for an isotropic porous media composed of spherical particles. Mathematically, the effective diffusivity is estimated as:

$$D_{eff} = D_{bulk} \frac{2\epsilon}{3 - \epsilon} \quad (1.28)$$

Das et al [52] used effective medium approximation and included the functions to consider liquid water saturation:

$$D_{eff} = D_{bulk} - \frac{3(1 - f_g)D_{bulk}}{3D_{bulk} - \frac{3(1 - f_l)D_l}{f_l - 3(1 - f_g)} - f_g} \quad (1.29)$$

where  $f_g$  and  $f_l$  are the volume fractions of the gas and liquid phase, respectively, and  $D_l$  is the diffusion coefficient of the gas in liquid water.

Percolation theory has also been employed to predict the effective diffusion coefficient in porous media. Tomadakis and Sotirchos [33] used random walk simulation results to predict the exponent,  $\alpha$ , and the percolation threshold,  $\epsilon_p$ , of randomly overlapping fiber structures. They proposed the following equation to compute the effective diffusion coefficient:

$$D_{eff} = D_{bulk} \epsilon \left( \frac{\epsilon - \epsilon_p}{1 - \epsilon_p} \right)^\alpha \quad (1.30)$$

where parameters  $\epsilon_p$  and  $\alpha$  are given in Table 1.1.

Percolation theory is also implemented by Nam and Kaviani [53] to estimate the effective diffusion coefficient. They assumed the porous media as 2 dimensional carbon fiber mats which have a solid structure of a stack of continuously overlapping fiber screens. After inclusion of liquid water, the final mathematical expression is given as:

$$D_{eff} = D_{bulk} \left( \frac{\epsilon - 0.11}{1 - 0.11} \right)^{0.785} (1 - S)^2 \quad (1.31)$$

The correlations for effective diffusivity defined above are known to overpredict the diffusion coefficient [54]. Zamel et al. [54] compared the diffusivity obtained from experiments and estimated from the models discussed above. The models overpredicted the effective diffusivity by a factor of 2 - 4. This over-prediction is mostly attributed to the significant differences in the structure of the GDL which has cylindrical carbon fibers and to the spherical particles that are assumed in the derivation of these correlations.

The effective diffusion coefficient of porous media can also be estimated numerically by modelling an accurate pore size distribution. The methods that are commonly employed to reconstruct the pore size distribution are: a) 3D volume imaging, and b) digitally stochastic models. In 3D volume imaging, the porous media is repeatedly sectioned and imaged automatically using X-ray or magnetic resonance. For digitally stochastic models, a pore distribution and pore structure is usually first obtained from mercury porosimetry.

A digital stochastic model was implemented by Zamel et al. [55] to estimate the effective in-plane and through-plane diffusivity. The tortuosity for in-plane and through-plane was estimated as 1.67 and 1.83 respectively, and the correlations are given as:

$$\frac{D_{eff}}{D_{bulk}} = \begin{cases} 1 - 2.76\epsilon \cosh(3\epsilon - 1.92) \left[ \frac{3(1 - \epsilon)}{3 - \epsilon} \right] & \text{(For through-plane)} \\ 1 - 1.72\epsilon \cosh(2.07\epsilon - 2.11) \left[ \frac{3(1 - \epsilon)}{3 - \epsilon} \right] & \text{(For in-plane)} \end{cases}$$

Zamel et al. [56] modified the above correlations to include the effect of liquid water. The porosity of the porous media was assumed to be reduced in the presence of liquid water. Hence, to estimate the effective diffusion coefficient, the porosity in

equation (1.3.2.1) is modified as:

$$\epsilon_{wet} = \epsilon_{dry}(1 - S) \quad (1.32)$$

where  $\epsilon_{wet}$  and  $\epsilon_{dry}$  are the porosities of porous media in wet and dry state, respectively.

### 1.3.2.2 Experimental studies of diffusivity

Several experimental techniques have been developed to study gas diffusivity. Marrero and Mason [57] compiled the available experimental techniques proposed in last decades based on their reliability, accuracy and use in literature. A compilation of the recent mass transport setups is also presented in Landolt Bornstein Series [58]. Nay and Armistead developed the two bulb method in 1947 [57]. The setup consists of two bulbs separated by a narrow tube or porous media as shown in Figure 1.9. The bulbs are filled with two different gases of interest. The tube is kept empty if bulk diffusivity is estimated or filled with a porous media to estimate the effective diffusion coefficient. The setup is flexible to run the experiment at various temperatures. The assumptions in the experiments are quasi-steady state, constant temperature and pressure. Fick's second law is used for data processing. The sources of error in the setup are the assumptions used for data analysis. To assume quasi steady-state, bulb sizes need to be large compared to the connecting tube. The composition gradient need to remain nearly constant during the experiment at tube ends hence an end correction length is implemented. The accuracy of diffusion coefficients in this setup has been estimated in the range of 0.1-0.2%. The setup has been used for temperatures range from 350-1300K [58].

The closed tube method, also known as Loschmidt cell method, was developed by Loschmidt in 1870 [57]. The setup has two chambers, containing two different gases, connected by a tube and/or porous media (see Figure 1.10). The chambers are isolated by a valve initially. Then, the valve is opened, and gases are allowed to diffuse. Gas concentration in one chamber is measured using sensors. Fick's transient law is used to estimate the effective diffusion coefficient. The measured parameters in the setup are concentration, time, pressure, temperature, and geometry. The source of error in this setup is the convective flow due to buoyancy effects. The convection due to buoyancy is minimized by using the lighter gas in the upper chamber. Using this setup, the diffusion coefficients have been estimated with accuracy in the range of 1 to

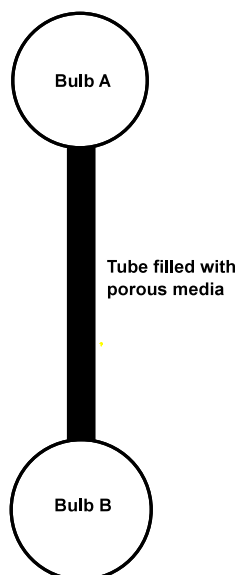


**Figure 1.9** – Two bulb setup

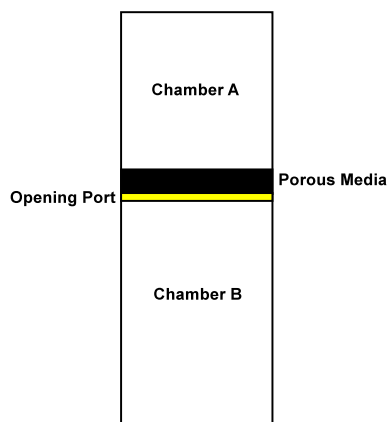


**Figure 1.10** – Closed tube setup

3% while some studies have been able to estimate diffusion coefficients with accuracy of  $\pm 0.7\%$  [58]. This setup has been used recently by many laboratories [16, 54, 59, 60]

The diffusion bridge setup (refer Figure 1.11), developed by Bendt [61], consists of two flow channels for two gases. The channels are separated by a porous media or capillary to allow gases to diffuse. The diffused gas is measured in the channel of the other gas using a concentration sensor. The driving force can be concentration or pressure gradient or both. The sources of error in this setup are the flow rate fluctuations and gas pressure in the channel. The setup has been used by various groups [61–67]. Evans III et al. [65] found that measurements are inaccurate at high pressure gradients using this setup. This however was due to the absence of

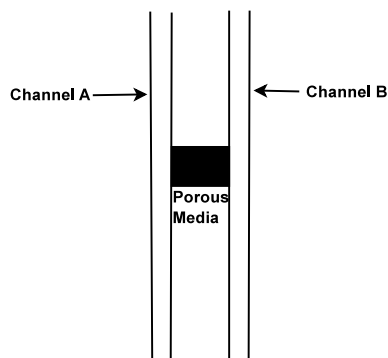


**Figure 1.11** – Diffusion bridge setup

pressure gradient term in the mathematical model to account for the viscous effects. Henry et al. [66] introduced nitrogen and helium in the channels and diffused through porous alumina. The thermal conductivity of the output streams was measured and compared with the conductivities of pure nitrogen and helium. The accuracy of the results were within the range of 5 to 30%. At higher pressures, the errors reduced to 6.29%. Reist [67] in his experiments found results within an accuracy of 10%. The advantage of this method is that both permeability and diffusivity can be obtained simultaneously.

The point source method to measure mass transport, shown in Figure 1.12, was developed by Westenberg and Walker [68]. The porous media is installed in a tube and a carrier gas entrains a tracer gas, supplied separately by an injector, through porous media. The mixture concentration is measured by a probe at various distances downstream. The assumptions in the setup is the axially symmetric concentration profile, infinitely dilute mixture, steady flow and uniform velocity. The sources of error are the difference in density of carrier and tracer gas, flow rate fluctuations and wake caused by the injector. The measurements have been done using this setup within an accuracy of 4% [57].

The evaporation tube method, also known as Stefan Tube Method was developed by Stefan (refer Figure 1.13). A liquid and carrier gas are separated by a porous media or a capillary. The rate of evaporation of liquid is controlled by diffusion. The carrier gas entrains the liquid vapours and swipes it away. The liquid level in the tube is measured for long durations. The setup is highly sensitive to temperature and pressure, small fluctuations result in large error. The temperature range is limited by the volatility of the liquid used. The results need to be end corrected for the tube length. This method is known to have high uncertainties in the measurement.

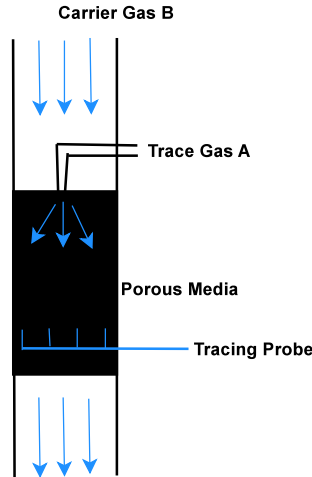


**Figure 1.12** – Point source setup

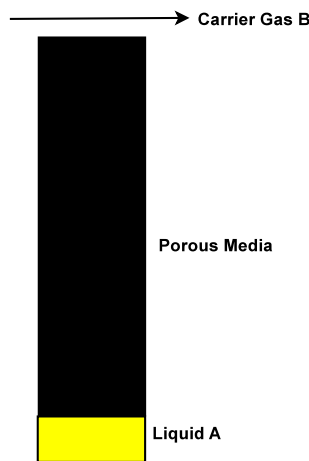


**Figure 1.13** – Evaporation tube setup

Whitaker [69] showed that assumptions of stagnant gas layer is invalid in the Stefan tube. Due to the momentum transfer across the tube, a velocity profile develops and causes circulations in the gas layer.

Through plane molecular diffusivity in fuel cell materials has been estimated using different methods by various groups. LaManna et al. [70] studied the effect of MPL, GDL thickness and PTFE experimentally in through-plane direction for 3 different GDL types, i.e., Grafil U-105, SGL (10, 25, 35), and Toray 120. A diffusion test cell was used to develop a water vapor concentration gradient in air streams across the porous media. The flow rates of the air streams were controlled by mass flow controllers. A dual stream humidifier controlled the relative humidity of each stream. Channel differential pressure measurements ensured zero differential pressure and no

bulk flow influences on diffusion. The effective diffusion coefficient decreased linearly with increasing PTFE content from 0.089 to 0.026 cm<sup>2</sup>/s while the introduction of an MPL reduced the coefficient by 26 - 38%. Thickness had no effect on GDL's but lower thickness resulted in low diffusion coefficients for MPL coated GDLs.

Hwang et al. [71] utilized a electrochemical limiting-current method to measure the effective diffusivity in the through-plane direction for uncompressed, partially saturated and unsaturated samples. Hydrogen was used as reactant. The limiting current for hydrogen supply was about 5 mA. The measured current was checked to ensure that diffusion-controlled limiting current was measured and not limited by hydrogen supply. Three different types of GDLs were studied, i.e. Toray-H-120, SGL 10 series, and Freudenberg H2315 with various PTFE loadings from 0-20 wt%. Diffusibility (defined as the ratio of effective to molecular diffusivity) was measured in the range of 0.247-0.584, and found to decrease with PTFE for unsaturated GDLs.

Zamel et al. [54] used a modified Loschmidt cell to estimate the through-plane diffusion coefficient for various Toray samples with different PTFE loadings, ranging from 0-40 wt%. Diffusibility was measured in the range of 0.13-0.33. Results showed a linear decreasing trend with PTFE loadings.

Chan et al. [16] also utilized a Loschmidt cell and studied the effect of PTFE, MPL and thickness on the through-plane diffusion coefficient. GDLs effective diffusivities were found in the order of 10<sup>-6</sup> m<sup>2</sup>/s while MPL reduced the diffusibility by around 42%.

The direct measurements of in-plane GDL molecular diffusivity with and without compression have not yet been reported in the literature. Kramer et al. [72] used electrochemical diffusimetry to measure the effective ionic conductivity of Toray - 060 at various porosities. In electrochemical diffusimetry, at high frequencies, the charge is transferred to the highly conductive carbon fibers. At low frequencies, the charge is transported through electrolyte filled pores in the sample. The pure electrolyte conductivity is modified by the geometric influence of the sample, i.e., porosity and tortuosity. The ratio of porosity to tortuosity was estimated for porosities in the range of 0.5 to 0.8 to be in the range of 0.2 to 0.6, and 0.1 to 0.3 for in-plane and through-plane directions respectively.

Fluckiger et al. [73] extended the study done by Kramer et al. [72], by studying

the effect of PTFE. The diffusivity was found to decrease with increasing PTFE content in both in-plane and through-plane directions. The experiments were further analyzed by implementing a unit cell model and conformal mapping.

Becker et al. [74] also measured conductivity in both in-plane and through-plane direction at various compression levels for Toray-H-060. A clamping force on GDL was applied, and voltage and current were measured across the GDL. Diffusibility was estimated in the range of 0.3 to 0.6 for in-plane, and 0.2 to 0.35 for through-plane respectively, for porosities in the range of 0.6 to 0.78. Further, 3D images were built using X-ray tomography under three compression levels, and used to validate the experiments.

Zamel et al. [75] used stochastic models to estimate in-plane and through-plane effective diffusion coefficients for GDL coated with MPL and calculated values in the range of  $10^{-6}$  to  $10^{-5}$  m<sup>2</sup>/s where in-plane values were higher by a factor of approximately 1.5 to 4 depending on the porosity.

## 1.4 Contributions

This research focuses on experimental measurement of mass transport properties in different directions of porous media. A diffusion bridge based setup is proposed to measure the transport properties. Due to the flexibility of diffusion bridge technique, it was chosen to use for the experiments. The setup is built flexible to subsequently test for permeability, Knudsen diffusivity and effective diffusivity in any direction of porous media. Using diffusion bridge, diffusion and advection can be studied simultaneously. Due to the steady state models, data analysis is easier. The setup can also be used to test with any pair of gases.

The contribution of this work is:

1. Development of a diffusion bridge based experimental setup to measure transport properties of porous media
2. Measurement of transport properties in through and in plane direction of porous media. The diffusion bridge is modified to make the flow direction appropriate

## 1.5 Thesis Outline

The thesis is divided into four chapters:

1. Chapter 1 focuses on motivation of research and literature review.
2. Chapter 2 focuses on measurement of mass transport properties of gas diffusion layers in in-plane direction. The measurements are done at four different compression levels and the effect of PTFE on transport parameters is studied.
3. Chapter 3 focuses on measurement of transport properties of gas diffusion layers and micro porous layer coated gas diffusion layers in through-plane direction. The effect of PTFE on transport properties is studied in GDL and GDL+MPL assembly.
4. Chapter 4 focuses on conclusions and future work

## Chapter 2

# Experimental study of in-plane mass transport properties of PEM fuel cell porous media

### 2.1 Introduction

Mass transport is one of the key factors limiting polymer electrolyte membrane fuel cell (PEMFC) performance, especially at high current densities. Mass transport in the gas diffusion layers of PEMFCs occurs mainly by molecular diffusion. However, both convection and Knudsen diffusion might become important under some circumstances. For example, in fuel cells with interdigitated channels, convection can be the dominant mode of mass transport. Pharoah [26] showed that, in serpentine fuel cells, convection might be important at the channel bends. Knudsen diffusion might also have a small role in gas transport for cases where, due to high PTFE loading and high compression, the average pore size in the GDL is reduced.

Permeability and effective molecular diffusivity are usually measured separately. An experimental method to concurrently measure permeability and diffusivity has not yet been proposed in the literature. Furthermore, even though there are many studies in the literature that have measured in-plane permeability, experimental studies measuring in-plane effective gas diffusivity of compressed and uncompressed GDLs by direct gas transport measurements are not available. The assessment of GDL effective diffusivity under compression is a critical parameter because the GDL is always under compression under the land area of the fuel cell. Reduced diffusivity in this area might lead to non-uniform reactant distribution in the catalyst layer in the in-plane direction and, at high current densities, severe reactant starvation.

In this chapter, a technique is proposed to measure in-plane permeability and effective molecular diffusivity concurrently thereby reducing the level of uncertainty when estimating these parameters because the setup is only assembled once and the same GDL sample is used for both measurements. The setup is based on a diffusion bridge previously proposed by Pant et al. [49]. The setup has been extensively modified by developing new testing hardware that allows for compression of the sample and by using a different arrangement of pressure controllers. Using the newly proposed setup, in-plane permeability and effective molecular diffusivity values are obtained for the same sample without having to open/close the hardware, thereby providing more reliable data.

Section 2.2 describes the experimental setup for both in-plane permeability and effective molecular diffusivity. The experimental conditions used in the experiment are also discussed. Section 2.3 provides the theory and mathematical models used to estimate the transport properties. In Section 2.4, the methodology used in this study is validated and transport parameters obtained for various commercialized samples are discussed.

## 2.2 Materials and Methods

This section describes the experimental setup for both in-plane permeability and effective molecular diffusivity.

### 2.2.1 Experimental Setup

The porosity of the samples in uncompressed state was measured by mercury intrusion porosimeter. Hence, the porosimeter is discussed before the mass transport setup. The experimental setup proposed in this article is based on a diffusion bridge setup. Therefore, the diffusion bridge is described followed by a description of the piping network and sensors used to control and measure mass flow rates, pressure difference, and oxygen concentration.

#### 2.2.1.1 Mercury Intrusion Porosimeter

Porosimetry tests were performed using a PoreMaster 33 Mercury Porosimeter manufactured by Quantachrome Instruments, 20 cm<sup>2</sup> of GDL was used for each test, cut

into strips measuring 2.24 cm by 0.56 cm.

To perform the intrusion test, the sample is placed inside the bulb of a glass penetrometer cell with 0.5 cc stem volume. The penetrometer cell is evacuated to an absolute pressure of 26.91 Pa (0.0039 psi) and then further evacuated for 30 minutes. The cell is filled with mercury and the mercury is then pressurized, up to a maximum pressure of  $2.277 \times 10^8$  Pa (33000 psi). The change in volume of mercury is measured as the pressure is raised.

Porosity of each sample is calculated using the following equation:

$$\epsilon_o = \frac{V_{pore}}{V_{total}} \quad (2.1)$$

where  $\epsilon_o$  is porosity,  $V_{pore}$  is the intruded pore volume and  $V_{total}$  is the total volume of the sample (both solid and void-space),  $V_{pore}$  is measured directly from the mercury intrusion test. Total volume of the sample is calculated by measuring the outer dimensions of the sample using a digital micrometer (Mitutoyo, Japan). The pressure at which intrusion occurs can be related to the presence of pores within the sample using the Washburn equation:

$$P \times D = -4\gamma\cos(\theta) \quad (2.2)$$

where  $P$  is the applied pressure,  $D$  is the pore diameter,  $\gamma$  is the surface tension of mercury and  $\theta$  is the contact angle between the mercury and the sample material. For the tests of the GDL samples  $\gamma$  was taken as  $480 \text{ dyne/cm}^{-1}$  and  $\theta$  as  $140^\circ$ .

The logarithmic pore size distribution,  $\frac{DX}{D(\ln(r))}$ , for a given pressure  $P_i$  normalized with respect to total sample volume, is calculated using the following equation:

$$\frac{DX}{D(\ln(r))} = \frac{(V_i - V_{i-1})/V_{pore}}{\ln(P_i) - \ln(P_{i-1})} \quad (2.3)$$

where  $X$  is the cumulative pore volume fraction,  $V_i$  is the absolute intruded volume measured up to pressure  $P_i$ , and  $V_{pore}$  is the total measured intruded volume,  $\frac{DX}{D(\ln(r))}$  is plotted with respect to pore radius to produce the pore size distribution curve for each sample. Figure 2.1 show the pore size distribution for Toray090 samples with different PTFE content. The higher PTFE content reduces the porosity and the effective pore diameter due to the penetration of PTFE in the available pores as shown in Table 2.1.

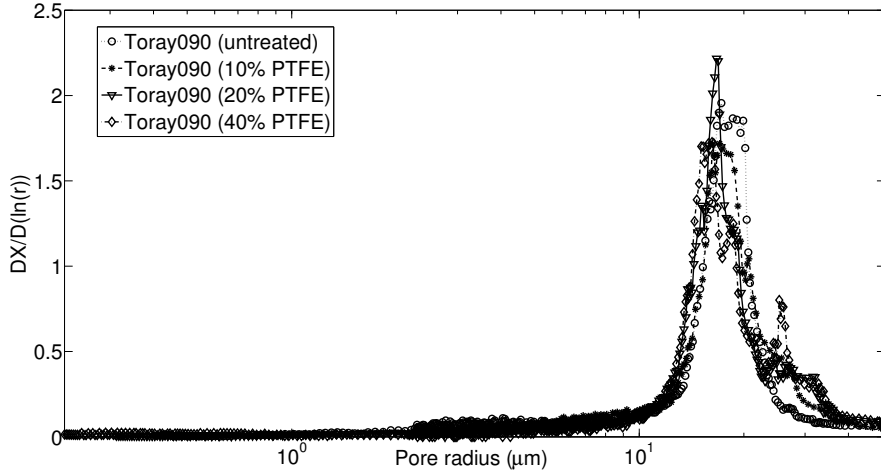


**Figure 2.1** – Pore size distribution of Toray 090 samples with different PTFE content

**Table 2.1** – Thickness and Porosity (MIP) data of GDL samples

Sample	Thickness ( $\mu\text{m}$ )	Porosity
SGL 34BA	$267 \pm 5$	$0.77 \pm 0.03$
Toray090 (untreated)	$273 \pm 6$	$0.76 \pm 0.02$
Toray090 (10% PTFE)	$290 \pm 4$	$0.76 \pm 0.01$
Toray090 (20% PTFE)	$283 \pm 5$	$0.69 \pm 0.01$
Toray090 (40% PTFE)	$282 \pm 4$	$0.54 \pm 0.01$

### 2.2.1.2 Diffusion bridge

A diffusion bridge is created by combining two stainless steel plates with two circular channels and a porous media between them. Figure 2.2 shows the exploded view of the diffusion bridge. The two circular channels of dimensions 8.8 mm diameter and 50 mm in length, are machined into the plate. The dimensions of the channels are selected such that high flow rates can be used without entering the transition or turbulent flow regimes. High flow rates are required to minimize any diffusion boundary layer effects.

In order to test a GDL, the diffusion bridge is assembled as follows. First, a sample of dimension  $10 \times 50 \text{ mm}^2$  is cut from the master sheet using an X-Acto knife and placed in between the channels. Then, a 10 mil (0.01 inch) thick silicon gasket is placed on the channel plates to prevent any gas leakage. The interface between the two side plates and channel plates (top and bottom) are connected through a 5

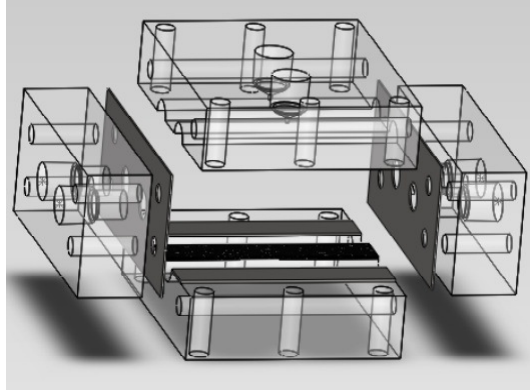


**Figure 2.2** – Exploded view of in-plane diffusion bridge

mm thick silicon gasket. Pressure films are used at both interfaces to ensure uniform pressure and a good seal. In order to test for leaks, the assembled diffusion bridge was pressurized at 50 psig for 12 hours, and no leakage was detected.

The top and bottom plates in the diffusion bridge were secured using bolts that are tightened in a cross cyclic manner to create a uniform compression. The bolts were tightened using a torque wrench. The effect of the applied torque was studied for the range of 5 to 15 Nm. A torque of 15 Nm provided repeatable results and ensured that the bolts did not enter the non-elastic deformation region. Therefore, a torque of 15 Nm is used for assembling the diffusion bridge in all experiments shown in the article.

The effect of PTFE loading and compression on in-plane permeability and effective diffusivity are studied. In order to study the effect of PTFE loading, GDL samples with different PTFE loading are analyzed, namely Toray 090 samples with 0, 10, 20 and 40% wtPTFE. In order to analyze compression, all samples are tested at 4 different compression levels. In order to control compression, the samples are compressed to a known thickness of  $262\pm 3$ ,  $249\pm 7$ ,  $228\pm 5$  and  $204\pm 3$   $\mu\text{m}$ . To control the GDL thickness, shims (ARTUS) of the desired thickness are placed at the edge of the diffusion bridge plates. The shims thickness were measured using a micrometer (Mitutoyo, Japan). The standard deviation in the thickness was obtained by measuring three samples of each shim. The same GDL sample is analyzed from lowest to highest compression. Conversion of thickness to porosity is performed by assuming that compression only reduces the volume of the pores. Then, the porosity

is calculated as a function of thickness with

$$\epsilon = 1 - (1 - \epsilon_o) \frac{t_o}{t}, \quad (2.4)$$

where  $\epsilon_o$  and  $t_o$  are the porosity and thickness of the uncompressed sample respectively and,  $t$  is the GDL thickness in its compressed state. The latter value is assumed to be equal to the thickness of the shims. Also, based on MIP data, the porosity in uncompressed state and PTFE content is linearly fitted as,  $\epsilon_o = 0.835 - 0.0074 \times (PTFE\%)$ . This expression is valid only for PTFE content between 10 - 40%.

The thickness of the samples in uncompressed state was measured using a micrometer. Table 2.1 show the data for the GDL samples used in this study. The average readings for both thickness and porosity are used to analyze the results.

The error in the porosity of the samples in compressed state is estimated by taking logarithm and differentiating both sides of equation (2.4). The final expression for the maximum error in the porosity is given by

$$\left| \frac{d\epsilon}{1 - \epsilon} \right| \leq \left| \frac{d\epsilon_o}{1 - \epsilon_o} \right| + \left| \frac{dt_o}{t_o} \right| + \left| \frac{dt}{t} \right| \quad (2.5)$$

where  $d\epsilon$  and  $d\epsilon_o$  are the error in the porosity, and  $dt$  and  $dt_o$  are the error in the thickness of the samples in compressed and uncompressed states respectively,  $d\epsilon_o$  corresponds to the error estimated by mercury intrusion porosimeter,  $dt$  corresponds to the error in the shims thickness, and  $dt_o$  corresponds to the error in the thickness of the GDL samples in uncompressed state, both were measured by a micrometer. The maximum error for porosity is estimated as 5% for sample SGL 34BA at 204  $\mu\text{m}$  thickness.

### 2.2.1.3 In-plane permeability setup

The diffusion bridge contains two channels. During in-plane permeability test, one channel, i.e., the low pressure channel, is open to atmosphere at both ends. One end of the high pressure channel, is connected to a mass flow controller (MFC). The other end is closed, thereby forcing the flow from the high pressure channel, through the porous media, to the low pressure channel, and to ambient (see Figure 2.3).

Compressed nitrogen (Praxair, UHP 5.0) is decompressed using a pressure regulator. Nitrogen at  $4.46 \times 10^5$  Pa (50 psig) is then made available to the MFC. The MFC (Cole-Parmer, model: RK-32907-69, range: 0-5 lpm) is used to control the

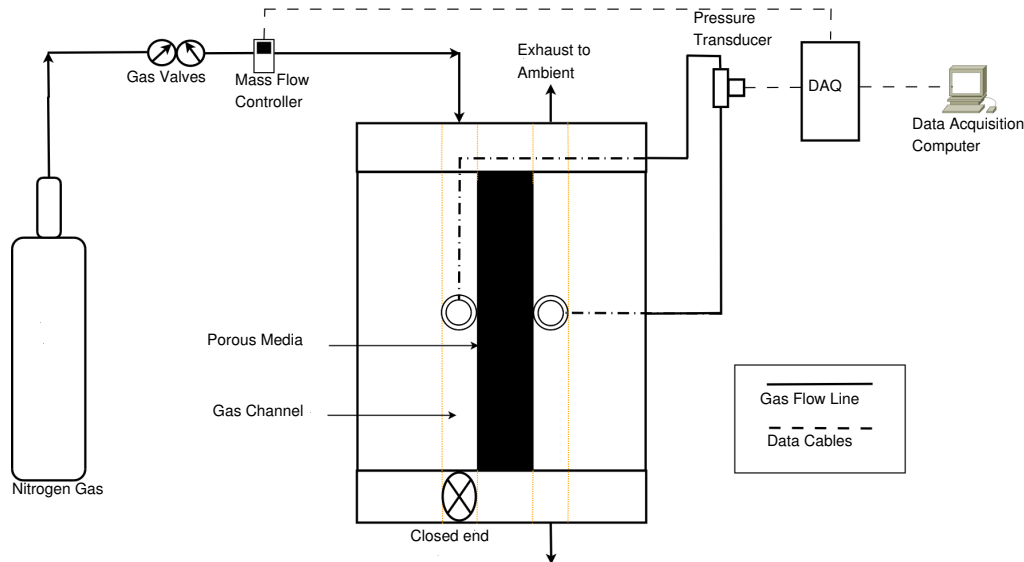


**Figure 2.3** – Experimental set-up to measure in-plane permeability

flow rates. The MFC is connected to a computer via an RS-232 communication port. The gas experiences certain pressure drop as it travels through the porous media. The channels are connected to a pressure transducer (OMEGA, Model: -MMDDB050BIV10B2C0T3A6) to measure the real time static pressure gradient at various flow rates. Data from the pressure transducer and mass flow controller is read via a data acquisition card (National Instruments USB 6221). LabWindows/CVI is used to communicate with the mass flow controller and log data from the mass flow controller and pressure transducer. The data is logged for 5 minutes (60 readings) for all flow rates to ensure steady state. Steady state is confirmed by ensuring that the standard deviation for pressure and mass flow rate is less than 3.0%.

#### 2.2.1.4 In-plane diffusivity setup

For in-plane diffusivity experiments, the inlet of each channel in the diffusion bridge is connected to a different gas cylinder, i.e., one containing oxygen and an other nitrogen. The two compressed gases, i.e., oxygen and nitrogen, are decompressed before passing through the mass flow controllers. Two mass flow controllers (Cole-Parmer, model: RK-32907-69, range: 0 - 5 lpm) are used to control the flow rate of gas in each channel. The outlet of the nitrogen channel is connected to a back pressure controller (Cole-Parmer, model: RK-00307OX, range: 0 - 100 psig) that is used to control the static pressure of the system. The oxygen channel outlet is connected to a differential pressure controller (Cole-Parmer, model: RK-00307TX, range: 0 - 500 Pa) which controls the static pressure difference between the two gas channels

using a differential pressure gauge connected to each channel (see Figure 2.4). The differential pressure controller can be used to control convection. Even though the differential pressure controller is rated to a higher resolution, experiments showed that the controller was capable of controlling the pressure difference within 7 Pa where oscillations are observed.

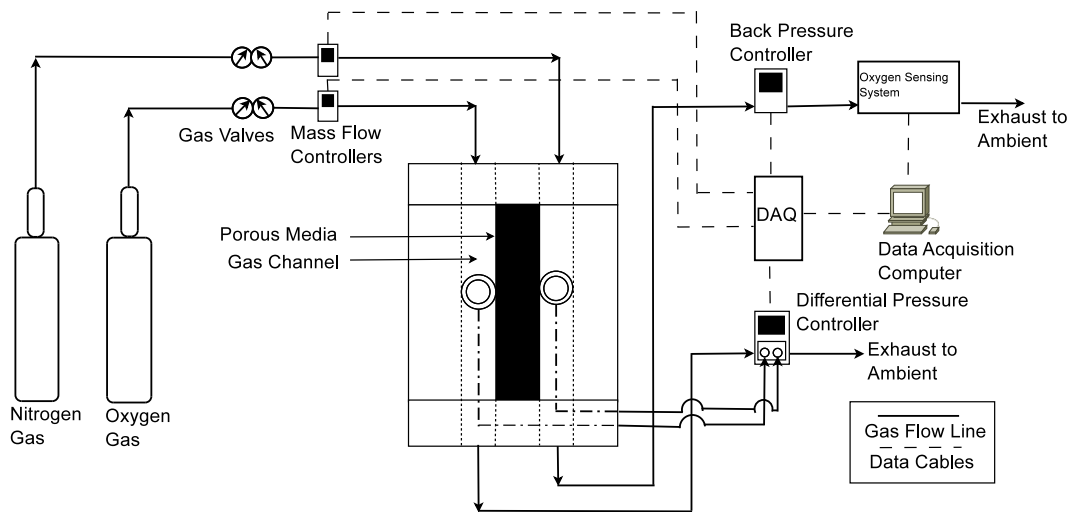


**Figure 2.4** – Experimental set-up to measure in-plane diffusivity

Oxygen levels are measured at the outlet of the nitrogen channel downstream of the back pressure controller using a NEOFOX oxygen sensor (Ocean Optics, Model: FOSPOR-600-32MM, range: 0 - 10% in gas). The sensor is factory calibrated for a range of 0-10 %  $O_2$  and temperature 0-80 °C. The range of temperature covered for calibration ensures consistent readings during day to day temperature fluctuations. The calibration file is uploaded in the NEOFOX software before experiments are started. One point calibration is performed in-house, after the multi-point calibration file is uploaded. Pure nitrogen gas (UHP 5.0) is exposed to the sensor and the reading is recorded as zero. One point calibration is done every time before the experiments are started. Figure 2.5 shows the physical picture of the setup.

The convection to diffusion transport is controlled by controlling the pressure difference between nitrogen and oxygen channels with the differential pressure controller. The oxygen channel is set at higher pressure than the nitrogen channel in order to enhance oxygen mass transport through the porous media via convective transport. The absolute pressure in the setup is also controlled using a backpressure controller in the nitrogen channel.

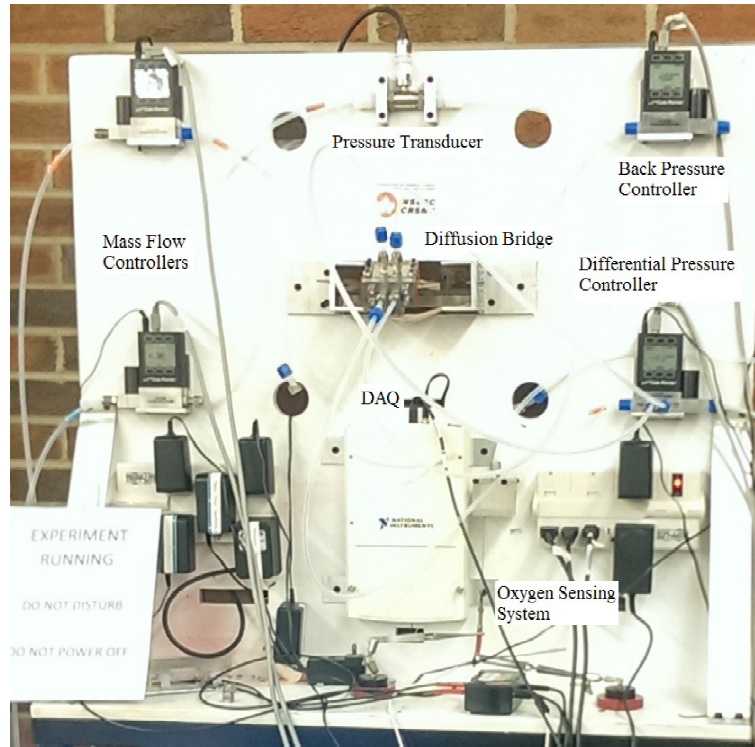


**Figure 2.5** – Experimental setup picture

Mass flow controllers and pressure controllers are connected to a computer via RS-232 communication port. The data from pressure and mass flow controllers is read via a data acquisition card. LabWindows/CVI is used for data logging, storing the data in a Excel file. Data for every set-point is logged, at a rate of one reading every 5 seconds, for 5 minutes to ensure steady state. The software provided by the NEOFOX sensors also stores the detected oxygen mole fraction with time, temperature and pressure in a CVS file every 2 seconds. Therefore, for every differential pressure, 150 readings for oxygen mole fraction are logged approximately. The average of the last twenty readings is used further. The data from Excel and CVS files are merged manually and used for further analysis.

## 2.2.2 Experimental Conditions

For in-plane permeability experiments, the volume flow rate of nitrogen gas was varied from 0-1 liters per minute (lpm) in 10 even intervals. The ‘zeroth interval’, which corresponds to zero flow rate, is run for 5 minutes to estimate the offset of the pressure transducer. The offset was eliminated from the average readings at non zero flow rates. The set-points were used for the mass flow rates, and the average of all

the pressure gradient data (60 readings) was used for further analysis. The average standard deviation for the selected flow rates from the MFC and pressure transducer is observed to be less than 3.0%.

For in-plane diffusivity experiments, the volume flow rate of both gases is set at 1 liters per minute (lpm). High flow rates are used to ensure the oxygen flux is quickly swept away in the nitrogen channel and the effects of diffusive boundary layers are minimized. The back pressure of the system is maintained at a gauge pressure 10 psig unless otherwise stated. The pressure difference between the two channels is varied from 20 - 100 Pa in 5 even intervals. The noise in the differential pressure controller is measured to be approximately  $\pm 7$  Pa. The noise in the differential pressure controller is the standard deviation of the last 40 readings at each setpoint. Oxygen mole fraction is recorded at every pressure differential. The temperature of the system in both cases is ambient.

### 2.2.3 Testing Protocol

Unless otherwise stated, in order to obtain permeability and diffusibility, permeability and diffusivity experiments are performed three times using three different samples cut randomly from the same master sheet, i.e., the samples were cut in random directions as it will be shown that fibers have no preferential orientation. For each sample, the diffusion bridge is opened and a new sample is installed. Permeability and diffusibility experiments are performed in each sample sequentially without opening/closing the diffusion bridge. The values reported are the average and standard deviation from the three samples tested. Therefore, the standard deviations account for sample-to-sample variability and setup variability. An analysis of the experimental error from various sources, i.e. experimental setup, sample-to-sample and directionality, is also provided in section 3.4.

## 2.3 Theory and Data Analysis

### 2.3.1 Mathematical models

#### 2.3.1.1 Governing equation for in-plane permeability

Darcy's law is commonly used to estimate the permeability of a porous media. Mathematically it is defined as

$$\nabla p = -\frac{\eta}{B_v} \vec{v}, \quad (2.6)$$

where  $\nabla p$  is the pressure gradient across porous media,  $\vec{v}$  is the velocity,  $\eta$  is the dynamic viscosity and  $B_v$  is the porous media permeability.

The fluid is assumed to flow only in the longitudinal direction of the porous media. A minimum of 22 fibers are calculated to be present between the top and bottom plates of the diffusion bridge for the chosen range of compression levels of the tested samples, hence the wall effects are neglected.

Darcy's law accurately quantifies porous media permeability for Stokes flow, also known as creep flow. At high flow rates, the fluid experiences various accelerations and decelerations as it flows through the porous media. This effect, known as Forcheimer effect, is considered to be negligible for sufficiently low velocities but can play a significant role when the velocities are high. In such cases, Darcy's law can be extended in order to obtain the Forcheimer equation, which in one dimension is given by

$$\frac{dp}{dx} = -\frac{\eta}{B_v}v - \frac{\rho}{B_l}v^2, \quad (2.7)$$

where  $x$  is the direction following the flow direction and  $B_l$  is known as the inertial permeability. Assuming the fluid is an ideal gas and replacing velocity with molar flux, equation (2.7) can be written as:

$$\frac{dp}{dx} = -\frac{RT}{p} \left( \frac{\eta}{B_v}N + \frac{M}{B_l}N^2 \right). \quad (2.8)$$

In the absence of a chemical reaction, the molar flux is constant. Then, integrating equation (2.8) for 0 to  $L$  and  $p_1$  to  $p_2$ . The compressible form of the Darcy-Forcheimer equation becomes

$$\frac{p_1^2 - p_2^2}{2RTL} = \frac{\eta}{B_v}N + \frac{M}{B_l}N^2, \quad (2.9)$$

where  $p_1$  and  $p_2$  are the pressures of the gas across the porous media,  $T$  is the temperature,  $R$  is the gas constant,  $L$  is the width of the sample,  $M$  is the molecular weight and  $N$  is the molar flux of the gas. In terms of mass flux,  $n$ , the Darcy-Forcheimer equation can be written as,

$$\frac{p_1^2 - p_2^2}{2RTL/M} = \frac{\eta}{B_v}n + \frac{1}{B_l}n^2. \quad (2.10)$$

### 2.3.1.2 Governing equations for in-plane diffusivity

Fick's first law is commonly used for analyzing the transport of a solute in an infinitely dilute mixture. Mathematically, it is defined as,

$$\vec{n}_i^D = -D_{ij}\nabla\rho_i, \quad (2.11)$$

where  $\vec{n}_i^D$  is the mass flux of the species  $i$  with respect to a frame of reference moving with mixture velocity  $\vec{v}$ . Equation (2.11) can also be written as

$$\rho_i(\vec{v}_i - \vec{v}) = -D_{ij}\nabla\rho_i, \quad (2.12)$$

where  $\vec{v}$  is the average mass velocity, defined as

$$\vec{v} = \frac{\Sigma\rho_i\vec{v}_i}{\Sigma\rho_i} = \frac{\Sigma\rho_i\vec{v}_i}{\rho_t} = \Sigma\omega_i\vec{v}_i. \quad (2.13)$$

Equation (2.12) can be simplified to

$$\vec{n}_i = \rho_i\vec{v}_i = \rho_i\vec{v} - D_{ij}\nabla\rho_i, \quad (2.14)$$

where  $\vec{n}_i$  is the mass flux of species  $i$ . In the absence of a chemical reaction, the mass flux of any species  $i$  is constant, and the divergence of equation (2.14) should be zero, i.e.

$$\nabla \cdot \vec{n}_i = \nabla \cdot (\rho_i\vec{v}) - D_{ij}\nabla^2\rho_i = 0 \Rightarrow \rho_i\nabla \cdot \vec{v} + \vec{v} \cdot \nabla\rho_i - D_{ij}\nabla^2\rho_i = 0. \quad (2.15)$$

Applying mass conservation on the mixture of gases, and assuming the density of the mixture is constant across porous media, the term  $\rho_i\nabla \cdot \vec{v}$  is zero. Since the pressure difference between the two channels is less than 100 Pa during diffusion experiments, the assumption is valid.

Then, equation (2.15) can be simplified as:

$$\vec{v} \cdot \nabla\rho_i = D_{ij}\nabla^2\rho_i, \quad (2.16)$$

Assuming one dimensional flow, equation (2.16) can be written as:

$$v\frac{d\rho_i}{dx} = D_{ij}\frac{d^2\rho_i}{dx^2}, \quad (2.17)$$

Integrating Equation (2.17) twice gives,

$$\rho_i = C_1\frac{D_{ij}}{v}e^{\frac{v}{D_{ij}}x} + C_2, \quad (2.18)$$

where  $C_1$  and  $C_2$  are the integration constants introduced. Applying ideal gas law and assuming the partial pressure of gas  $i$  is  $p_i^A$  in channel A ( $x=0$ ) and  $p_i^B$  in channel B ( $x=L$ ), equation (2.18) yields

$$\rho_i = \frac{M_i}{RT} \left[ p_i^A - (p_i^A - p_i^B) \left( 1 - e^{\frac{v}{D_{ij}}L} \right)^{-1} + (p_i^A - p_i^B) \left( 1 - e^{\frac{v}{D_{ij}}L} \right)^{-1} e^{\frac{v}{D_{ij}}x} \right]. \quad (2.19)$$

The density profile from equation (2.19) can be used in equation (2.14) for mass flux such that

$$n_i \Big|_{x=0} = \frac{M_i}{RT} \left[ p_i^A v - (p_i^A - p_i^B) v \left( 1 - e^{\frac{v}{D_{ij}}L} \right)^{-1} \right]. \quad (2.20)$$

where  $v$  is the velocity of the mixture which is constant. Similarly the molar flux is calculated as:

$$N_i \Big|_{x=0} = \frac{1}{RT} \left[ p_i^A v - (p_i^A - p_i^B) v \left( 1 - e^{\frac{v}{D_{ij}}L} \right)^{-1} \right]. \quad (2.21)$$

The flux calculated from equation (2.21) is the local pore flux, i.e., it is not averaged over the entire porous media. The tortuosity and porosity of the porous media are used to calculate the effective flux, equation (2.21) is then modified to:

$$N_i^{eff} \Big|_{x=0} = \frac{1}{RT} \left[ p_i^A \bar{v} - (p_i^A - p_i^B) \bar{v} \left( 1 - e^{\frac{\bar{v}}{D_{ij}^{eff}}L} \right)^{-1} \right], \quad (2.22)$$

where  $\bar{v} = \epsilon v$ ,  $N_i^{eff} = \epsilon N_i$  and  $D_{ij}^{eff} = \frac{\epsilon}{\tau} D_{ij}$ . The ratio of effective diffusivity to molecular diffusivity is defined as diffusibility. The mixture mass averaged velocity  $\bar{v}$  is calculated using Darcy's law,

$$\bar{v} = -\frac{B_v}{\eta} \frac{dp}{dx} \approx \frac{B_v}{\eta} \frac{\Delta P}{L} \quad (2.23)$$

where  $B_v$  is the viscous permeability of the porous media and  $\eta$  is the dynamic viscosity of the gas mixture. The mixture viscosity,  $\eta$ , is used as the average of the viscosity of oxygen and nitrogen,  $\eta = \frac{\eta_{O_2} + \eta_{N_2}}{2}$ . Since the velocity through the porous media is small for the diffusion experiments, the Forcheimer term is neglected.

### 2.3.2 Model implementation

In the permeability experiments, the inlet velocity and pressure drop are obtained experimentally. The molar flux is obtained using  $N = \frac{pv}{RT}$ , where  $v$  is the inlet velocity and  $p$  is the inlet pressure. Then, the experimental data is fit to equation (3.5) using MATLAB to extract transport parameters, i.e.,  $B_v$  and  $B_l$ . The function `fittype` is used for fitting. `fittype` uses a least squares regression technique to minimize the residual. The coefficient of regression for all the fittings is found to be greater or equal to 0.99.

In the effective diffusivity experiments, the oxygen molar fraction,  $x_{O_2}^{out}$ , and the pressure difference between channels are recorded directly. In order to estimate the oxygen flux across the porous media,  $N_{O_2}$ , the molar flux in the nitrogen gas channel and the molar flux across the porous media are calculated. The molar flux in the nitrogen gas channel is given by

$$N_{Ch} = \frac{\rho_{N_2} \dot{V}}{M_{N_2}} \quad (2.24)$$

where  $\rho_{N_2}$  is the density of nitrogen at 10 psig and  $\dot{V}$  is the volume flow rate set by mass flow controller. The molar flux through the porous media are calculated as

$$N_p = \frac{p}{RT} Av, \quad (2.25)$$

where  $p$  is the pressure in the oxygen channel, i.e.  $p_{O_2}$ ,  $A$  is the cross-sectional area of the GDL sample, and  $v$  is the superficial gas velocity in porous media

$$v = \frac{B_v \Delta p}{\eta_{O_2} L}. \quad (2.26)$$

where  $\Delta p$  is the pressure difference between channels and  $B_v$  is the GDL permeability. Then,  $N_{O_2}$  is estimated as,

$$N_{O_2} = x_{O_2}^{out} \times \frac{N_p + N_{Ch}}{A}. \quad (2.27)$$

Equations (2.22) and (2.23) are used to fit the experimental data to extract the effective diffusion coefficient, i.e.  $D_{ij}^{eff}$ . The permeability value,  $B_v$ , is obtained from the previous in-plane permeability experiments. The function `lsqcurvefit` in MATLAB is used for fitting. `lsqcurvefit` also uses a least squares regression technique to minimize the residual. The mathematical model requires four boundary conditions, which are the densities of gases in the channels, i.e.,  $\rho_{O_2} = \frac{p_{O_2} M_{O_2}}{RT}$ ,  $\rho_{N_2} = 0$  in the oxygen channel, and  $\rho_{N_2} = \frac{p_{N_2} M_{N_2}}{RT}$ ,  $\rho_{O_2} = 0$  in the nitrogen channel.

## 2.4 Results and discussion

### 2.4.1 In-plane permeability

Various commercial GDLs are tested, i.e., SGL 34BA, Toray 090 (untreated) and Toray 090 samples treated with 10, 20 and 40% PTFE.

#### 2.4.1.1 Error analysis

**2.4.1.1.1 Sensor error** The error in the permeability results is determined based on the sensors error data published by the manufacturers. To maximum the error in the viscous permeability results, the inertial permeability is neglected in the compressible form of Darcy - Forcheimer equation (equation (2.9)). The equation is reduced to,

$$\frac{p_1^2 - p_2^2}{2RTL} = \frac{\eta}{B_v} N, \quad (2.28)$$

The molar flux of the gas is calculated as,

$$N = \frac{pv}{RT}, \quad (2.29)$$

where  $v$  is the velocity of the gas. Velocity of the gas at the inlet of the sample is calculated as,

$$v = \frac{V}{wt}, \quad (2.30)$$

where  $V$  is the volume flow rate,  $w$  and  $t$  is the width and thickness of the GDL sample, respectively.

Taking the logarithm and differentiating both sides of equation (2.28), and terms are rearranged with the assumption,  $p_1^2 - p_2^2 \simeq p_1^2$ . Equation (2.28) reduces to,

$$2 \left| \frac{dp_1}{p_1} \right| = \left| \frac{dN}{N} + \frac{dL}{L} - \frac{dB_v}{B_v} \right| \leq \left| \frac{dN}{N} \right| + \left| \frac{dL}{L} \right| + \left| \frac{dB_v}{B_v} \right| \quad (2.31)$$

To find the error in the molar flux, equation (2.29) and (2.30) are rearranged and differentiated both sides. The expression for error in molar flux is substituted in equation (2.31). The final expression for the maximum error in the viscous permeability is

$$\left| \frac{dB_v}{B_v} \right| \leq 3 \left| \frac{dp_1}{p_1} \right| + \left| \frac{dV}{V} \right| + \left| \frac{dw}{w} \right| + \left| \frac{dt}{t} \right| + \left| \frac{dL}{L} \right| \quad (2.32)$$

The error in the GDL dimensions is assumed as 10 microns. The error in the inlet pressure  $p_1$ , and volume flow rate  $V$  correspond to the error in the readings by pressure

transducer and mass flow controller, respectively. The error in pressure transducer and mass flow controller from their manufacturers are given as  $\pm 0.05\%$  and  $\pm 0.8\%$ , respectively. The width and length of the GDL sample are 50 and 10mm, respectively, The minimum thickness of the sample is considered i.e. 204.33 microns. Substituting the errors in equation (2.32),

$$\left| \frac{dB_v}{B_v} \right| \leq 3 \times 0.0005 + 0.008 + \frac{10}{50000} + \frac{10}{204.33} + \frac{10}{10000} \Rightarrow \left| \frac{dB_v}{B_v} \right| \leq 0.05964 \quad (2.33)$$

The maximum error from the experimental setup in the viscous permeability results is calculated as 5.964%.

**2.4.1.1.2 Test variability** The reliability of the setup is determined by assembling a diffusion bridge with a SGL 34BA sample. The thickness was set at  $262\mu\text{m}$ . The experiments were run for three times without opening/closing the diffusion bridge. The pressure gradient versus velocity data is obtained from the setup for three sets of readings. The standard deviation in the viscous permeability results is estimated as 0.84%. Figure 2.6 shows the actual and average flow rate, and pressure gradient readings measured by MFC and pressure transducer, respectively. Clearly, steady state is observed at each setpoint, and fluctuations are small compared to the changes observed due to the selected setpoints.

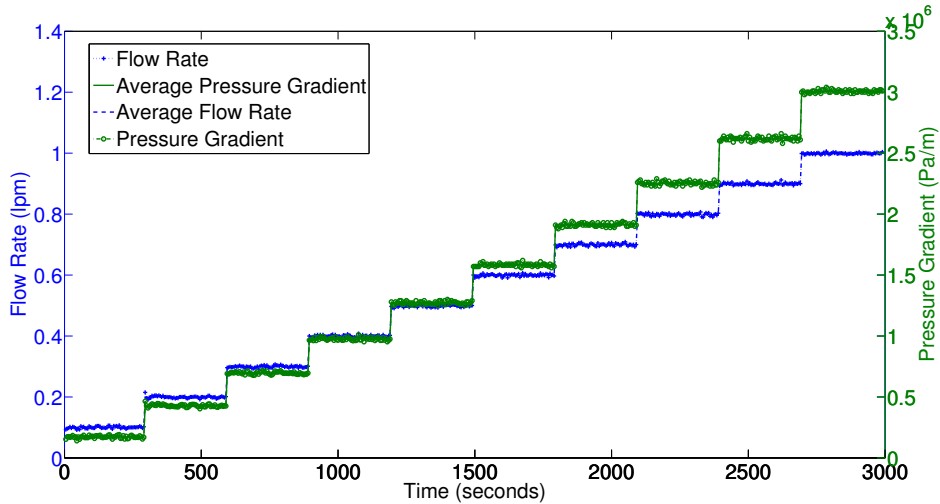


**Figure 2.6** – Oscillatory and average volume flow rate, and pressure gradient readings for a Toray 090 (untreated) sample at  $262\pm 3$  thickness

**2.4.1.1.3 Variation within sample of the same master sheet** GDLs are spatially anisotropic hence samples are cut off the master sheet at  $0^\circ$  with reference

to the edge of the sheet chosen randomly. Three replicates of sample SGL 34BA are cut and tested. The samples are tested for permeability at four compression levels. The standard deviation in the viscous permeability results for samples cut in the same direction is estimated as 39.44%, 42.86%, 15.58% and 13.21% for thickness corresponding to 262, 249, 228 and 204 $\mu\text{m}$  respectively.

**2.4.1.1.4 Variation within the sample in different direction** To study the spatial anisotropic nature of the sample SGL 34BA, samples are cut in four different angles from 0° to 90°, with respect to an edge of the sheet chosen randomly. Thickness of the samples is set at 262  $\mu\text{m}$ . Results are shown in Table 2.2.

**Table 2.2** – In-plane permeability for sample SGL 34BA at various angles

Angle	$B_v \times 10^{-11}(\text{m}^2)$
0°	2.06
30°	1.89
60°	1.63
90°	2.48

The standard deviation in the viscous permeability results for sample-to-sample variation cut in different direction from the same master sheet is estimated at 17.6% assuming thickness of 262  $\mu\text{m}$ .

GDL spatial anisotropy was observed in paper based samples in previous work [14, 28]. Results show a variation in permeability of a factor of 1.3-2 in two in-plane orthogonal directions. Results in Table 2.2 show no trend due to non preferential fiber alignment in sample SGL 34BA. The standard deviation in the permeability results for samples cut in different directions is estimated to be similar to that of the samples cut in the same direction. Therefore, it is concluded that direction has no effect on mass transport parameters, and the spatial anisotropy of the chosen samples is considered uniform in the plane of the paper. The SEM images of Toray 090 samples are also shown to have non-preferential alignment of fibers [14] (also see Figure 2.10), therefore they are cut in the random directions of the same master sheet for the results in this article.

### 2.4.1.2 Effect of compression on in-plane permeability and validation

The effect of compression on permeability is studied by controlling the thickness of the GDL samples using shims. Pressure vs molar flux curves are drawn for each compression. The mass transport parameters are estimated using the compressible form of the Darcy-Forcheimer equation (equation (2.9)). The inlet pressure vs molar flux curves for sample Toray 090 (untreated) are shown in Figure 2.7 at different flow rates and at four different compression levels. The error bars in Figure 2.7 represent the standard deviation for inlet pressure from the pressure transducer. The higher inlet pressure at higher compression is due to the reduction of average pore diameter.

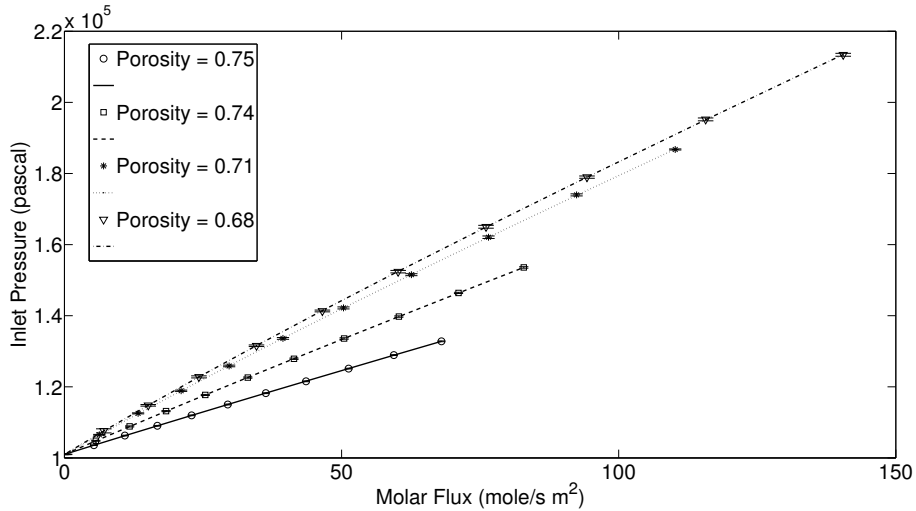


**Figure 2.7** – Inlet pressure versus molar flux curves for a Toray090 (untreated) sample at various compression levels

Viscous and inertial permeability results for Toray 090 (untreated) are shown in Table 2.3, and compared with literature. Results are found in good agreement with literature thereby supporting the validity of the experimental apparatus. The slight difference in the results are due to the samples being from different master sheets, errors influenced by the thickness of the shims used, and the measurement of the porosity of the samples in uncompressed state from MIP. Results show that the viscous and inertial permeability decreases with compression. The pore diameter reduces with compression thereby increasing the flow resistance of the porous media.

The dependence of permeability on porosity in porous media is often described by the Carman-Kozeny equation [14]

**Table 2.3** – In-plane permeability for sample Toray090 (untreated)

Porosity	$B_v \times 10^{-11}(m^2)$	$B_l \times 10^{-5}(m)$	Literature ( $B_v \times 10^{-11}(m^2)$ )
0.75±0.029	0.95 ± 0.03	0.80 ± 0.04	(1.46 ± 0.2) [36], 0.89 [14]
0.74±0.035	0.68 ± 0.11	0.49 ± 0.14	0.72 [14]
0.71±0.037	0.50 ± 0.03	0.33 ± 0.03	-
0.68±0.039	0.44 ± 0.04	0.30 ± 0.04	0.43 [14]

$$K = \frac{d_f^2 \epsilon^3}{16K_{CK}(1 - \epsilon)^2}, \quad (2.34)$$

where  $d_f$  is the fiber diameter,  $\epsilon$  is the porosity and  $K_{CK}$  is known as the Carman-Kozeny constant which is considered a fitting parameter for a particular sample. A more comprehensive model to predict permeability is proposed by Tomadakis and Sotirchos (TS). The Tomadakis - Sotirchos model [76] predicts the anisotropic permeability through 1D, 2D and 3D fiber beds for flow being parallel or perpendicular to fiber alignment. Using the model, the in-plane permeability can be estimated as:

$$K = \frac{\epsilon}{8(\log \epsilon)^2} \frac{(\epsilon - \epsilon_p)^{\alpha+2} r_f^2}{(1 - \epsilon_p)^\alpha [(1 + \alpha)\epsilon - \epsilon_p]^2} \quad (2.35)$$

where  $\alpha$  and  $\epsilon_p$  are the model parameters depending on fiber alignment and flow direction. This model is shown to overpredict the permeability at high porosities [35]. The parameters  $\alpha$  and  $\epsilon_p$  in TS model for 3D fiber alignment in all directions is given as 0.661 and 0.037 respectively.

The Carman-Kozeny constant  $K_{CK}$  is fitted with the permeability values at four

**Table 2.4** – Data fit for Carman-Kozeny Parameter

Sample	$K_{CK}$	Literature [14]
SGL 34BA	3.90 ± 1.12	4.06 ± 16.1% , 5.6 ± 21.1%
Toray090 (untreated)	4.10 ± 0.22	4.07 ± 6.3%
Toray090 (10% PTFE)	3.9 ± 0.64	-
Toray090 (20% PTFE)	2.26 ± 0.09	-
Toray090 (40% PTFE)	0.67 ± 0.09	-

compression levels. The fiber diameter is used as 7.5 and 9.2  $\mu\text{m}$  for sample SGL 34BA and Toray090 (0, 10, 20 and 40% PTFE) respectively. Table 2.4 shows the

Carman-Kozeny parameter for various tested samples as well as the values obtained by Gostick et al. [14]. The parameter values are in good agreement for sample Toray090 (untreated) and SGL 34BA. Figure 2.8 and 2.9 show the comparison of Carman-Kozeny and TS model with permeability for SGL 34BA and Toray090 (untreated) samples.

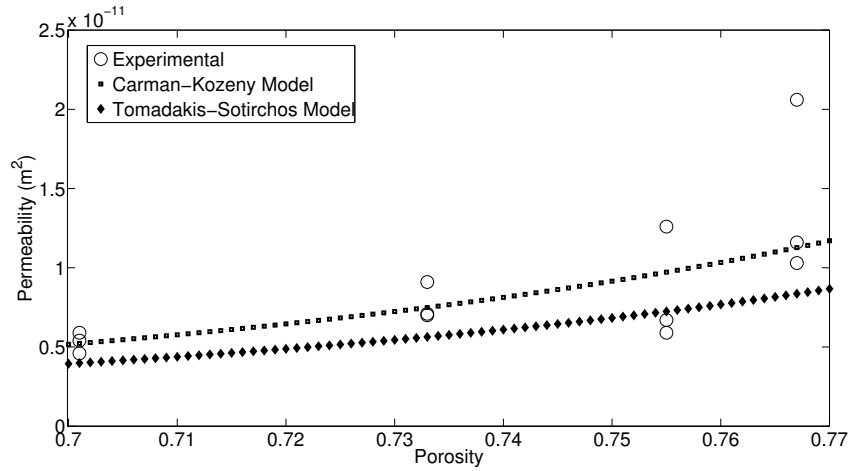


**Figure 2.8** – Comparison of permeability results with Carman-Kozeny and T-S Model for SGL 34BA sample

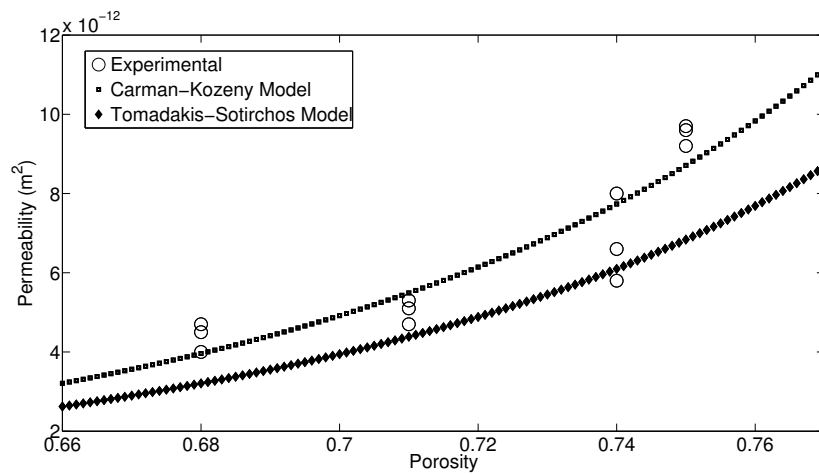


**Figure 2.9** – Comparison of permeability results with Carman-Kozeny and T-S Model for Toray090 (untreated) sample

### 2.4.1.3 Effect of PTFE on in-plane permeability

The effect of PTFE is studied by testing Toray 090 samples with 0, 10, 20 and 40% PTFE. All the samples are tested at four different compression levels. Top views of

the GDLs are obtained via SEM imaging (JEOL 6301F, Field Emission SEM). Figure 2.10 shows the SEM images for Toray090 samples loaded with different PTFE content.

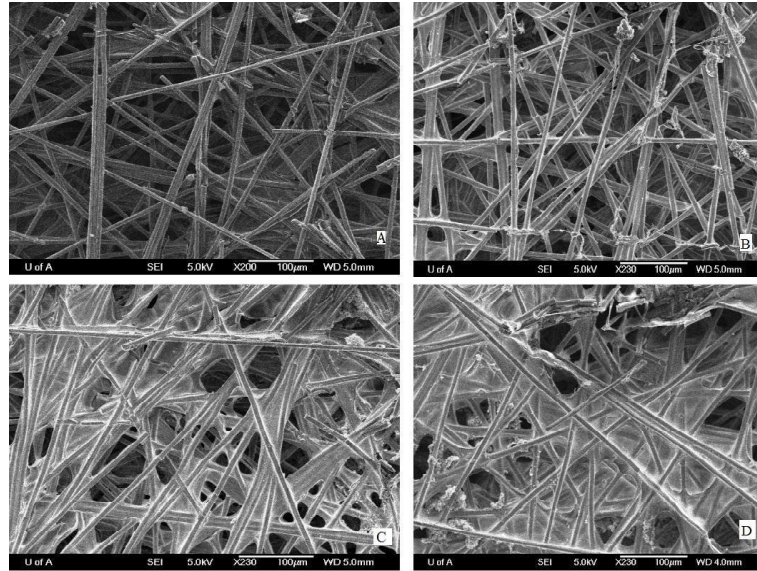


**Figure 2.10** – SEM image for Toray090 samples with (A) 0, (B) 10, (C) 20 and (D) 40% PTFE loadings

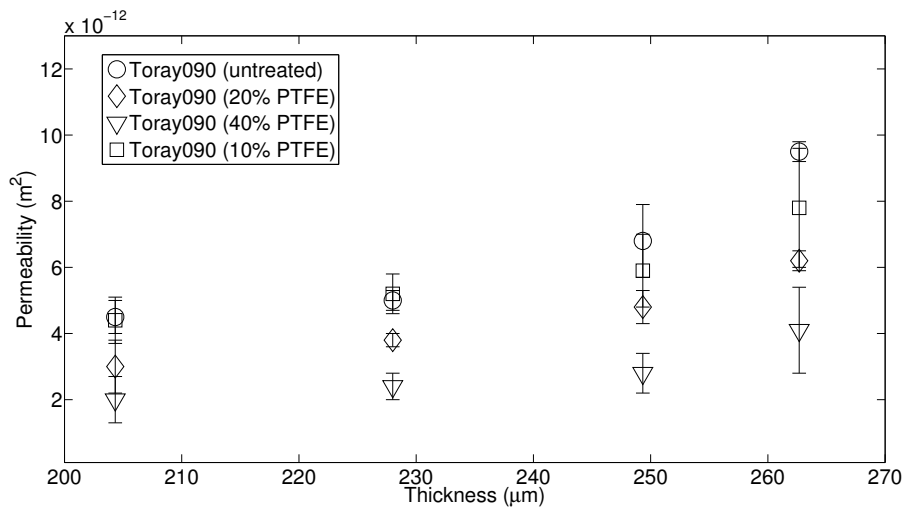


**Figure 2.11** – Permeability results for different PTFE loadings at various thickness

The Carman-Kozeny constant is estimated for Toray 090 samples with high PTFE content (10, 20 and 40% PTFE). Table 2.4 shows the constant for the samples. Figure 2.11 and 2.12 shows the viscous permeability results for different PTFE loadings at different thickness and porosity, respectively. The error bars in the results represent

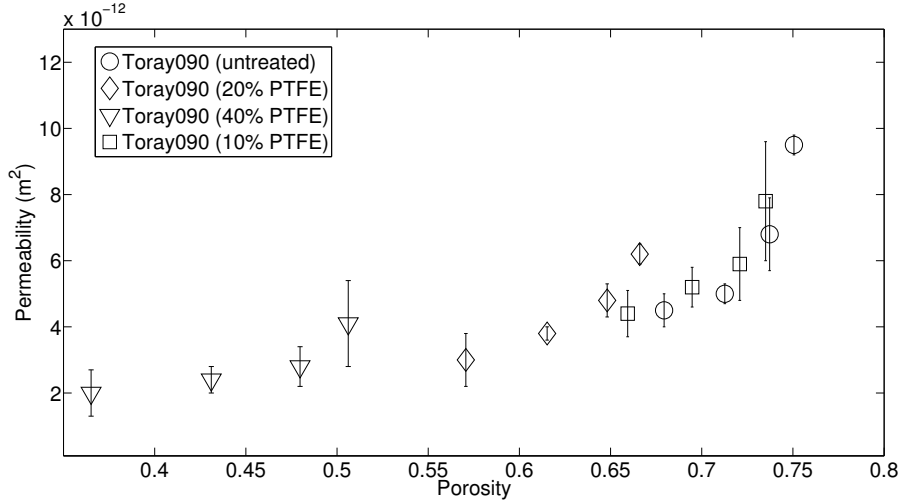


**Figure 2.12** – Permeability results for different PTFE loadings at various porosities

the standard deviation estimated by testing three replicates of each sample (see section 2.2.3). The permeability is observed to decrease with PTFE content. SEM images show the PTFE binders spread over the intersection of fibers thereby reducing pore size. Figure 2.12 shows that compression and PTFE loading have a similar effect on permeability.

#### 2.4.1.4 Knudsen effects

Flow in porous media are classified in different regimes based on Knudsen number. The Knudsen number is mathematically defined as [46],

$$K_n = \frac{\lambda}{d_p} \quad (2.36)$$

where  $\lambda$  is the mean free path length of the gas and  $d_p$  is the average pore diameter of porous media. As discussed in section 2.3.1.1, Darcy’s law is able to predict the permeability for Stokes flow with no-slip boundary condition, and is valid only in the continuum regime, when Knudsen number is less than 0.001. A slip boundary condition is required between continuum and free molecular flow, i.e.  $0.001 \leq K_n \leq 10$  [46]. Carrigy et al [46] studied the Knudsen effect for GDLs, with and without MPLs, in the through-plane direction, by measuring gas permeability with two gases of very different mean free paths. Deviations in permeability predictions with different gases were attributed to Knudsen effects. Results showed that Knudsen effects are negligible for carbon substrates but become significant with MPLs due to their pore diameters around nm in size. Since PTFE reduces the pore diameters in GDLs, 40% PTFE by

weight showed different permeability results for helium and nitrogen. Based on the results obtained by Carrigy et al [46], which showed no Knudsen effects for Toray samples with 0 - 20% PTFE, only the sample with 40% PTFE is investigated in this study. The sample is tested with helium and nitrogen gases without opening/closing the diffusion bridge. Table 2.5 shows the viscous and inertial permeability for helium and nitrogen gases estimated using equation (3.5).

**Table 2.5** – In-plane permeability for sample Toray 090 with 40 % PTFE

Thickness	$B_v \times 10^{-11} (m^2) (N_2)$	$B_v \times 10^{-11} (m^2) (He)$	$B_l \times 10^{-5} (m) (N_2)$	$B_l \times 10^{-5} (m) (He)$	$B_v (He)/B_v (N_2)$
262	0.75±0.08	0.78±0.09	0.23±0.05	0.20±0.11	1.04±0.02
249	0.41±0.06	0.43±0.04	0.11±0.02	0.09±0.03	1.06±0.08
228	0.27±0.02	0.29±0.02	0.06±0.01	0.05±0.01	1.04±0.02
204	0.23±0.03	0.25±0.03	0.05±0.01	0.04±0.01	1.06±0.02

For 95% confidence interval, a Student’s t-test was performed on the results shown in Table 2.5. The t-test was done by comparing the ratio of the viscous permeability data for helium and nitrogen to 1. The t-tests showed that the viscous permeability for helium and nitrogen are not significantly different from each other except at 204 $\mu$ m thickness. The p-value for 204 $\mu$ m thickness was calculated as 0.0156. Therefore, the Knudsen slip might become significant at high compression (27.65% or more). Given that Knudsen effects only appear to be significant for high PTFE and high compression, Knudsen diffusivity effects are neglected for all GDLs.

## 2.4.2 In-plane effective molecular diffusivity

A diffusion bridge is created between the pair of oxygen and nitrogen gas. Various commercial GDL samples are tested including sample SGL 34BA and Toray 090 with 0, 10, 20 and 40% PTFE loadings.

### 2.4.2.1 Error analysis

**2.4.2.1.1 Test variability** The reliability of the setup is determined by assembling a diffusion bridge with a Toray 090 (untreated) sample. The thickness was set at 262  $\mu$ m. The experiments were run three times without opening/closing the diffusion bridge. The oxygen molar flux versus differential pressure data is obtained from the setup for all three sets of readings. Figure 2.13 shows the three set of readings, and fit with Fick’s and Darcy’s model. The standard deviation for diffusibility is estimated as 3.84%.

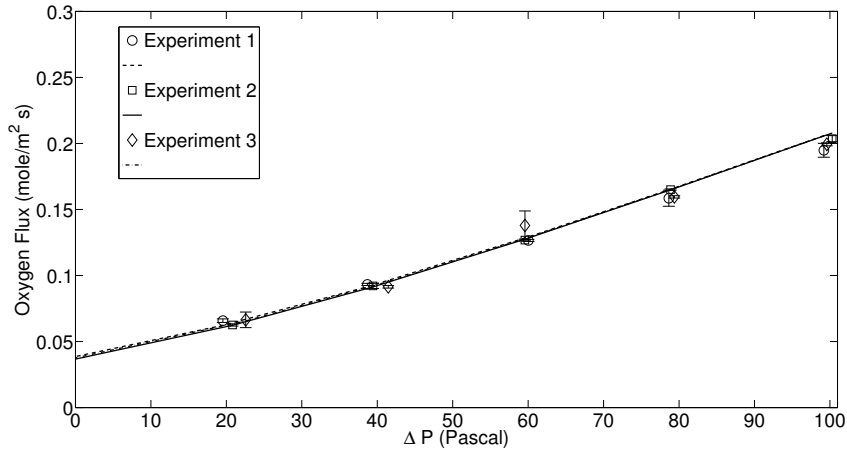


**Figure 2.13** – Test repeatability for a Toray 090 (untreated) sample at  $262\pm 3$  thickness

Figure 2.14 shows the actual, and average differential pressure and oxygen mole fraction measurements from the differential pressure controller, and oxygen sensor, respectively. The fluctuations from the differential pressure controller led fluctuations in oxygen sensor measurements. However, the fluctuations from both the sensors are small compared to the changes observed due to the selected setpoints. Even with the fluctuations, the results were found repeatable.

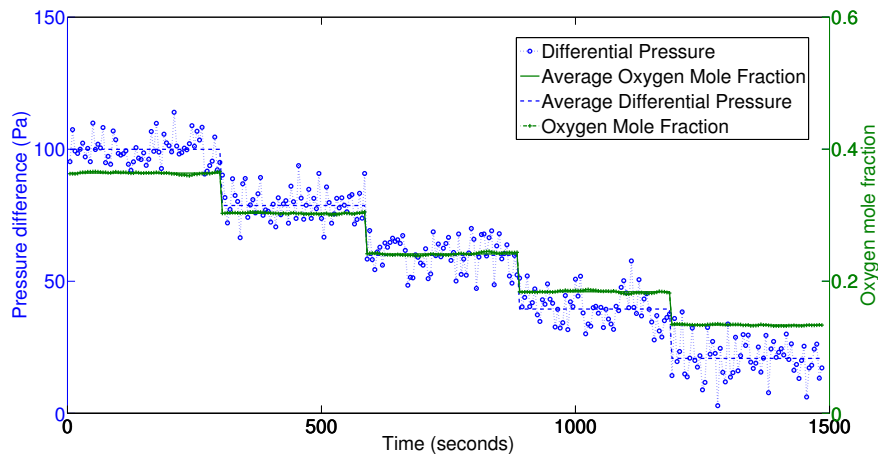


**Figure 2.14** – Oscillatory and average differential pressure, and oxygen concentration readings for a Toray 090 (untreated) sample at  $262\pm 3$  thickness

**2.4.2.1.2 Variation between samples** As already shown in the results section of permeability, GDLs used in this study are spatially anisotropic but do not have a preferential orientation of fibers. Hence, for diffusion experiments, samples are

cutoff from a master sheet in random directions to take into account the effect of directionality. Three Toray 090 (untreated) samples are cut from the same master sheet at random directions. The standard deviation for diffusibility for sample-to-sample variation is estimated as 12.5%, 9.3%, 32.26% and 19.23% for thickness is corresponding to 262, 249, 228 and 204  $\mu\text{m}$  respectively.

**2.4.2.1.3 Variation with channel flow rate** Diffusion experiments were performed at three different flow rates, i.e. 0.5, 1.0 and 1.5 lpm, for a Toray090 (20% PTFE) sample at 204  $\mu\text{m}$  thickness to ensure the results are consistent with the assumption that diffusive boundary layer effects in the nitrogen channel are negligible. Higher flow rates are not considered to avoid any turbulent flow in the channels. The standard deviation for diffusibility for the selected range of flow rates is estimated as 5.83%. For the selected range of differential and absolute pressures, the oxygen concentration and molar flux in the nitrogen channel were low enough for any boundary layer effects, hence results were found consistent with different flow rates.

#### 2.4.2.2 Validation studies

**2.4.2.2.1 Effect of absolute pressure** Kinetic theory of gases predicts that the product of absolute pressure and molecular diffusivity is constant. Mathematically,

$$P \times D_{bulk} = constant. \quad (2.37)$$

The experimental setup predictions are verified by changing the absolute pressure of the diffusion bridge to 10, 15 and 20 psig using the back pressure controller for a Toray 090 (untreated) sample at 249  $\mu\text{m}$  thickness. The tests are run three times at each absolute pressure. Table 2.6 shows the variation of diffusibility with absolute pressure of the system. The molecular diffusivity at atmospheric pressure for  $N_2 - O_2$  is used as  $2.065 \times 10^{-5} m^2/s$ . The molecular diffusivity at higher pressure is calculated using the equation from kinetic theory of gases (equation (2.37)). Since diffusibility is a geometric property of porous media, it is not expected to vary with absolute pressure. Results shown in Table 2.6 confirms that the results are consistent with absolute pressure of the system. For 95% confidence interval, a Student's t-test on the measured data justifies that the results are not significantly different from each other.

#### 2.4.2.3 Effect of compression on in-plane diffusivity

The effect of compression on diffusivity is studied by controlling the thickness of samples using shims. At each compression, the molar flux of oxygen is estimated, based

**Table 2.6** – Effect of absolute pressure on diffusivity

Pressure (psig)	Diffusibility
10	$0.45 \pm 0.02$
15	$0.44 \pm 0.04$
20	$0.41 \pm 0.02$

on the measured oxygen molar fraction, and plotted against the pressure difference set across the porous media. The mathematical models depend on the effective diffusivity and the porous media permeability. The permeability values for the mathematical model are the values obtained in section 2.4.1. Then, the diffusibility is estimated by minimizing the least squares error between the model and the experimental data. The error bars in the diffusibility results show the standard deviation in the results obtained by testing 3 replicates of the sample from same master sheet.

Figure 2.15 shows the estimated oxygen flux at different differential pressure for Toray 090 (untreated) at four different levels of compression. The error bars for the oxygen flux represent the standard deviation in the readings measured by the oxygen sensor. The oxygen flux data is fitted into the Fick - Darcy model, i.e. equation (2.22) and (2.23). The oxygen flux is found to decrease with increasing compression at any differential pressure. As discussed in section 2.4.1, the reduction of average pore diameter at higher compression reduces the permeability of the porous media thereby reducing the oxygen flux. At zero differential pressure, the convective flux is zero, hence all the oxygen flux corresponds to pure diffusion. Interpolating the lines in Figure 2.15 to the y-axis shows the pure diffusive flux at four levels of compression. The pure diffusive flux is also shown to decrease with increasing compression.

The diffusibility is estimated for Toray090 (untreated) using the Fick - Darcy model and MBFM at different levels of compression, i.e., different porosities. Table 2.7 shows the numerical values of diffusibility. The diffusibility is found to decrease with higher compression. The reduced porosity and increased tortuosity with higher compression decrease diffusibility. The results are compared with the results obtained by Becker et al. [74] and Kramer et al. [72] for Toray060 (untreated) sample. Toray090 (untreated) and Toray060 (untreated) samples are known to have equal porosities, hence comparable transport properties. The samples differ only in physical properties, i.e., tensile strength and thickness. Results are found in good agreement with

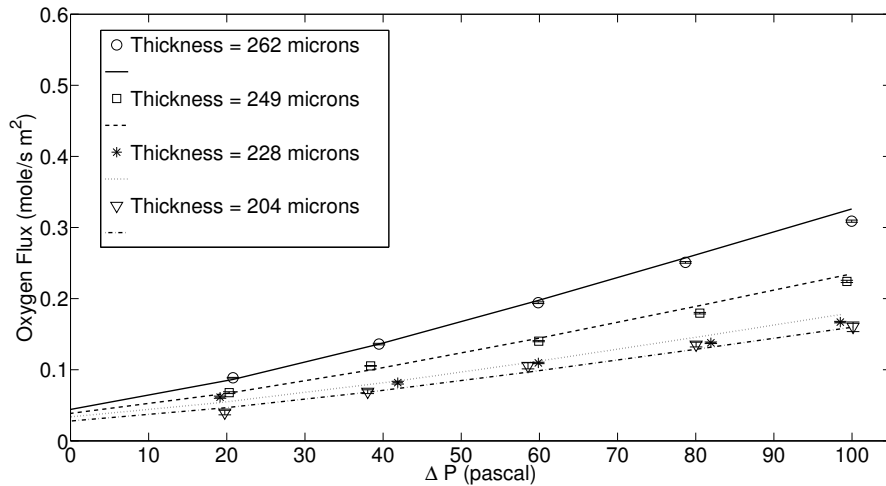


**Figure 2.15** – Experimental data fit to Fick - Darcy model for a Toray090 (untreated) sample

literature at low compression levels but differ as compression increases. The reasons might be due to errors in the thickness and porosity measurements of the sample in compressed and uncompressed state. The standard deviation in the diffusibility results is obtained by testing three replicates of the same sample.

**Table 2.7** – In-plane diffusibility for Toray 090 (untreated) at different compression

Porosity	Diffusibility	Literature (Toray 060)
$0.75 \pm 0.029$	$0.48 \pm 0.06$	0.53 [74], 0.49 [72]
$0.74 \pm 0.035$	$0.43 \pm 0.04$	0.51 [74], 0.48 [72]
$0.71 \pm 0.037$	$0.31 \pm 0.10$	0.47 [74], 0.44 [72]
$0.68 \pm 0.039$	$0.26 \pm 0.05$	0.43 [74], 0.39 [72]

#### 2.4.2.4 Effect of PTFE on in-plane diffusivity

The effect of PTFE is studied by testing Toray 090 samples with 0, 10, 20 and 40% PTFE. All the samples are tested at 4 different compression levels. Figures 2.16 and 2.17 show the results obtained from Fick - Darcy model at different porosities and thickness, respectively. As already discussed, PTFE binders block the pores of the porous media, thereby reducing the available pore space for gas transport. Figure 2.16 shows that increasing PTFE loading has a similar effect as reducing the porosity of the sample, therefore, it can be concluded that PTFE does not substantially

modify the gas transport pathways in the GDL.

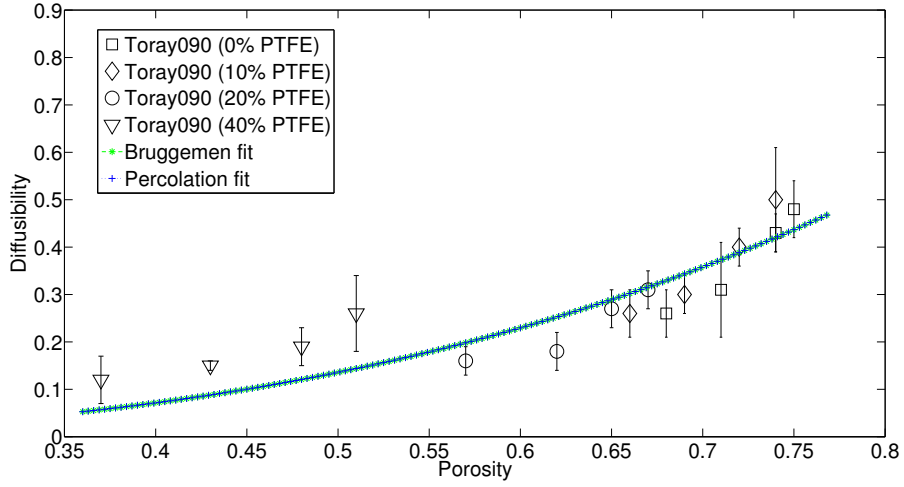


**Figure 2.16** – Diffusibility results from Fick-Darcy Model for different PTFE loadings at various porosities

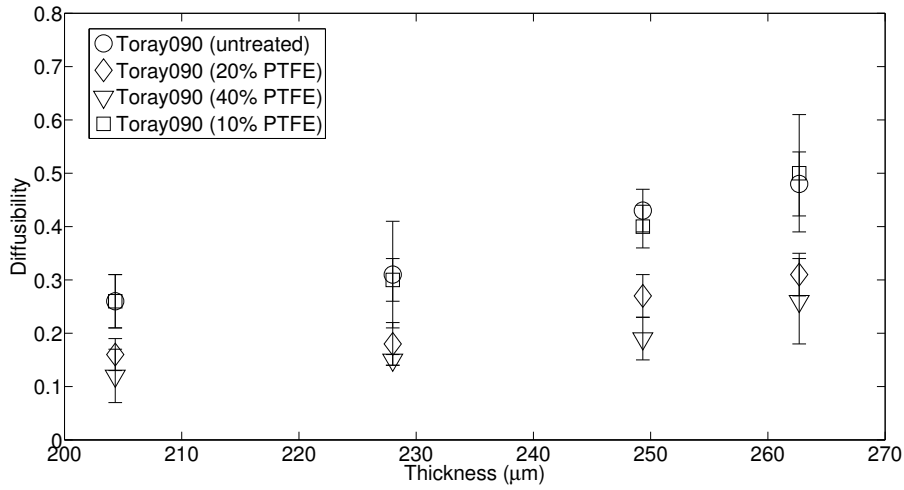


**Figure 2.17** – Diffusibility results from Fick-Darcy Model for different PTFE loadings at various thickness

To predict the tortuosity of the porous media, diffusibility obtained from Fick - Darcy model is fitted to two empirical equations: a) Bruggeman's equation, and b) Tomadakis and Sotirchos' equation [33], i.e.

$$D^{eff}/D = \frac{\epsilon}{\tau} = \epsilon^{\gamma_b} \quad (2.38)$$

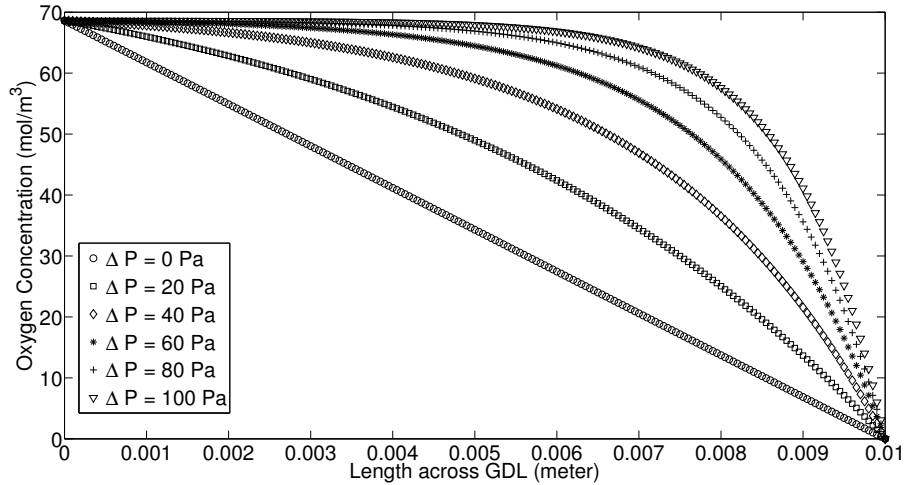
and

$$D^{eff}/D = \frac{\epsilon}{\tau} = \epsilon \left( \frac{\epsilon - \epsilon_p}{1 - \epsilon_p} \right)^{\gamma_t} \quad (2.39)$$

respectively, where  $\epsilon$  is the porosity, and  $\gamma_b$ ,  $\gamma_t$  and  $\epsilon_p$  are fitting parameters. The function `fittype` in MATLAB is used for fitting. For Bruggeman's model, the fitted parameter  $\gamma_b$  is 2.88. For Tomadakis and Sotirchos' equation, the fitting parameters  $\gamma_t$  and  $\epsilon_p$  are 1.88 and  $4.71 \times 10^{-13}$ , respectively.

#### 2.4.2.5 Mathematical model of Oxygen flux across porous media

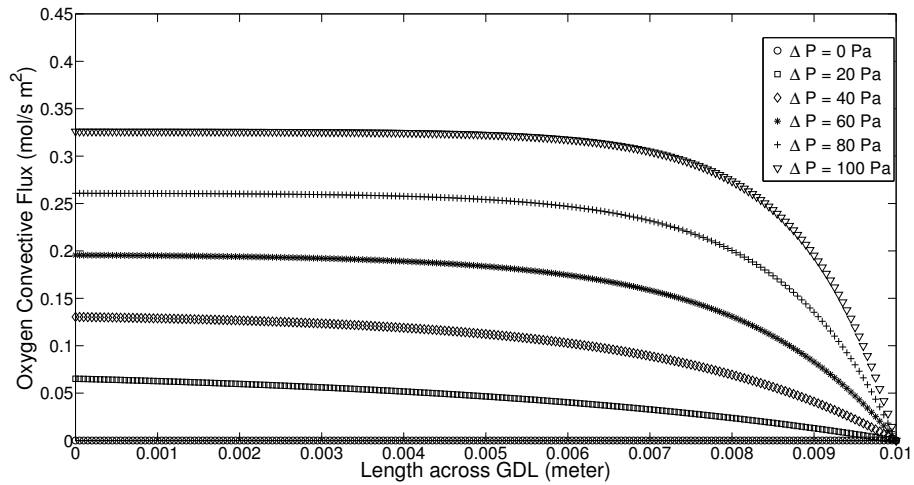
In order to understand the effect of convection and diffusion during transport, oxygen concentration curves are obtained for a Toray090 (untreated) sample at  $262 \mu\text{m}$  thickness using the Fick - Darcy model, and permeability and diffusivity values of  $0.92 \times 10^{-11} \text{m}^2$  and  $0.52 \times 10^{-5} \text{m}^2/\text{s}$ , respectively. Figure 2.18 shows the oxygen concentration curves across the GDL sample at various differential pressures. The oxygen flux is measured to be less than 1% in the nitrogen channel for the selected GDL samples and experimental conditions. Therefore, the oxygen concentration is approximated as zero at the end of the porous media.



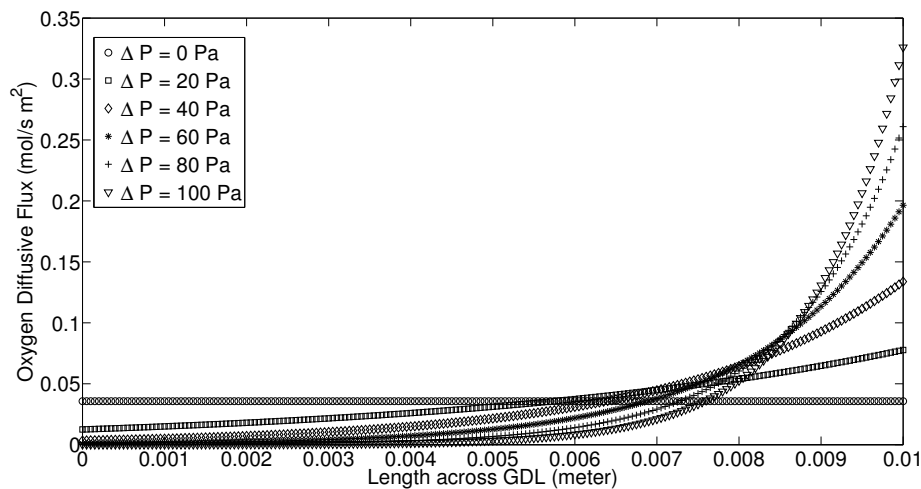
**Figure 2.18** – Estimated oxygen concentration across Toray 090 (untreated) at various differential pressure

Figure 2.19 and 2.20 show the convective and diffusive oxygen molar flux at different differential pressures, respectively. For zero differential pressure, convective flux is zero, and diffusive flux is constant across the porous media. The convective

flux dominates the diffusive flux significantly at the inlet of the porous media as differential pressure increases. For the minimum non zero differential pressure, i.e., 20 Pa, the diffusive flux contribution is 16.09% at the inlet of the porous media. As the differential pressure increases to 100 Pa, the diffusive flux contribution drops to 0.011%.



**Figure 2.19** – Oxygen convective flux across Toray 090 (untreated) at various differential pressure



**Figure 2.20** – Oxygen diffusive flux across Toray 090 (untreated) at various differential pressure

As differential pressure increases, the oxygen concentration profiles are pushed to the right. Therefore, the slope of oxygen concentration profile decreases at the inlet

of the porous media. Hence, the diffusive flux decreases. The concentration of the oxygen at the end of the porous media is approximated as zero, hence convective flux is zero at any differential pressure, and the total flux corresponds to the diffusive flux. At any location in porous media, the sum of convective and diffusive flux remains constant. The total oxygen flux increases from 0.036 to 0.326  $mol/sm^2$  as differential pressure increases from zero to 100 Pa. Based on these results, the experimental conditions of tests are appropriate since both convection and diffusion are relatively modified.

## 2.5 Conclusion

A novel experimental setup is proposed based on a diffusion bridge to determine the effective transport properties of gas diffusion layers. The proposed setup is flexible to subsequently test for permeability, Knudsen diffusivity and effective molecular diffusivity of the layers. The permeability is estimated by measuring the pressure drop across porous media at various flow rates set by a mass flow controller. The experimental data is fit in the compressible form of Darcy - Forcheimer equation to extract transport parameters, i.e., viscous and inertial permeability. The Knudsen diffusivity is estimated by running the permeability experiments using different gases with very different mean free paths, i.e., nitrogen and helium. The difference in the permeability estimated for two gases, was attributed to Knudsen slip. The effective molecular diffusivity was measured by running two gases in two channels separated by the porous media. The flow rates, absolute pressure, and pressure difference between the channels was controlled by mass flow controllers, back pressure controller, and differential pressure controller, respectively. The moles of oxygen in the nitrogen channel were measured by an oxygen sensor at various differential pressures. Fick - Darcy model was used to fit the experimental data, and effective molecular diffusivity was computed.

The effect of PTFE over permeability was studied by testing Toray 090 samples with 0, 10, 20 and 40% wt PTFE. Samples were also tested at four compression levels corresponding to the thickness of 262, 248, 228, and 204  $\mu m$ . The viscous permeability was estimated in the range of  $0.98 - 0.13 \times 10^{-11} m^2$ . The Knudsen diffusivity was estimated to be negligible for a Toray 090 (40% PTFE) sample except for high compressions (27.65% or more). Hence, the Knudsen diffusivity was assumed to be negligible in the samples with less PTFE content. The viscous permeability results were fitted with Carman-Kozeny model. The Carman-Kozeny parameter was esti-

mated for various GDL samples which could be used for 2D or 3D simulations.

The effect of PTFE and compression was also studied on diffusibility by testing Toray 090 samples with 0, 10, 20 and 40% PTFE . The diffusibility was estimated between 0.52-0.09, and found to make an inverse relationship with PTFE and compression. An empirical equation was proposed for in-plane diffusibility by fitting the experimental results. The proposed empirical equation for diffusibility should be useful for simulations of gas transport in the gas diffusion layers.

# Chapter 3

## Experimental study of through-plane mass transport properties of PEM fuel cell porous media: Permeability, and Knudsen and molecular diffusivity

### 3.1 Introduction

In this chapter, a diffusion bridge based experimental technique is proposed to measure the permeability, Knudsen diffusivity and effective molecular diffusivity in through plane direction of the porous media. The setup was originally proposed by Pant et al. [49] and Carrigy et al. [46]. However, the setup is extensively modified by introducing a different set of pressure sensors, controllers to control convection and oxygen sensors. The diffusion test is subsequently conducted after permeability or permeability-Knudsen diffusivity tests without opening/closing the diffusion bridge, thereby ensuring accurate results.

Section 3.2 discusses the samples tested, diffusion bridge, experimental setups to measure permeability. Knudsen diffusivity and effective molecular diffusivity, and experimental conditions. Section 3.3 focuses on the theoretical models, assumptions and their implementation. Section 3.4 discuss the results for the tested samples and their validation with the literature.

## 3.2 Materials and Methods

This section explains the experimental setup for permeability, Knudsen diffusivity and effective molecular diffusivity.

### 3.2.1 Experimental Setup

The experimental setup proposed in this article is based on a diffusion bridge setup. Therefore, the diffusion bridge is described first followed by a description of the piping network and sensors used to control and measure mass flow rates, pressure difference and oxygen concentrations.

#### 3.2.1.1 Diffusion bridge

A pair of acrylic plates are assembled to effectively create a diffusion bridge between two gases. Figure 3.1 shows the exploded view of the bridge. Two rectangular channels of dimensions  $15 \times 2 \text{ mm}^2$  are machined in the plates. The length of the channels is 150 mm. The channel lengths are designed to make sure the gases are fully developed prior to their exposure to the porous media.

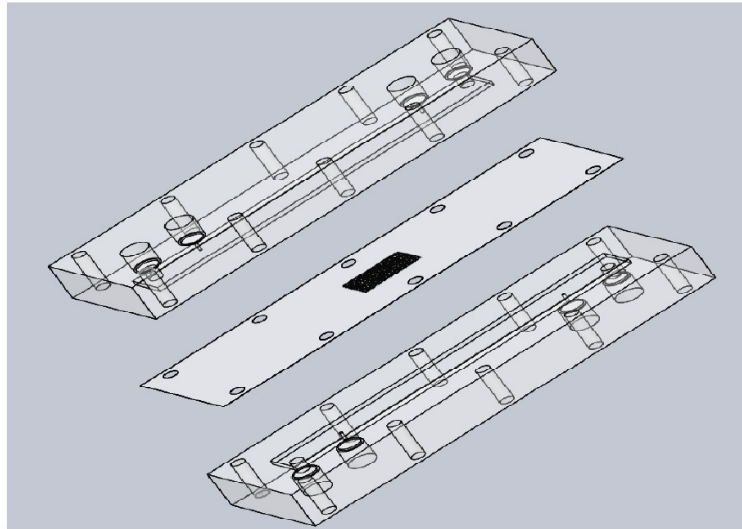


**Figure 3.1** – Exploded view of through-plane diffusion bridge

In order to test a GDL, a sample of dimension  $20 \times 25 \text{ mm}^2$  is prepared by cutting from a master sheet using an X-Acto knife. Three layers of samples of equal dimensions are stacked upon each other in all the experiments. The prepared samples are shown in Figure 3.2. A hole of diameter 9.5mm is punched in the center of

the lamination sheet to allow the gas to pass through the porous media. The sample is laminated (HeatSeal H220 laminator) in a 3mil lamination sheet. The thickness of the layers are measured using a micrometer (Mitutoyo, Japan) at a load of 0.5N. The layers are assumed to be compressed during the lamination. The amount of compression is estimated by measuring the thickness of sample before and after lamination, and calculated to be less than 5% for Toray 090 samples. The GDLs coated with MPL were prepared by stacking two layers with MPLs facing each other. This arrangement of the GDL-MPL layers is selected to ensure the ink of the MPL is not damaged during the lamination.

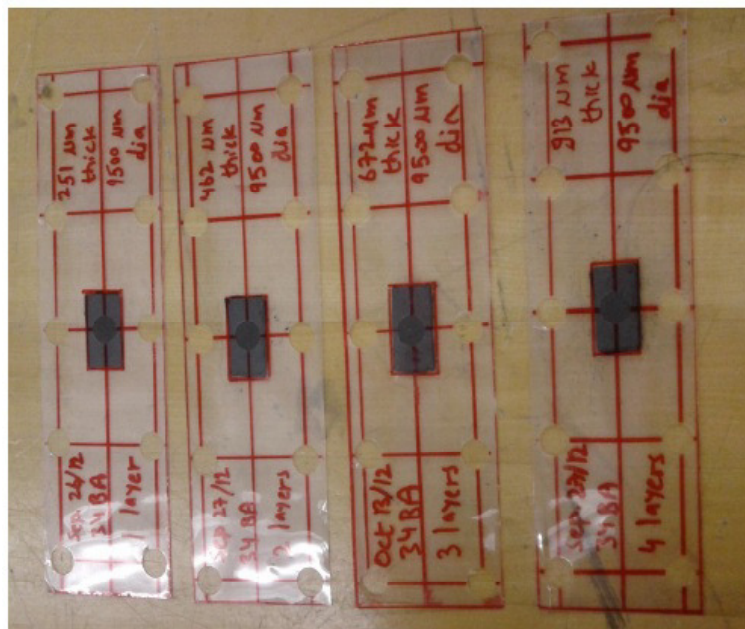


**Figure 3.2** – Laminated GDL samples

The top and bottom plates in the diffusion bridge were secured using bolts that are tightened in cross cyclic manner to create a uniform compression. The bolts were tightened using a torque wrench. A torque value of 10 N-m was found sufficient for assembly without damaging or bending the acrylic plates. A 10 mil (0.01 inch) silicon gasket is placed around all the edges of the diffusion bridge to prevent any leakage. The bridge was pressurized at 40 psig for 12 hours to detect leakage. No leakage was observed.

### 3.2.1.2 Through-plane permeability and Knudsen diffusivity setup

The diffusion bridge contains two channels. Each channel is designed to have four ports. One end of the high pressure channel, is connected to a mass flow controller. The other ports are closed, thereby forcing the flow from the high pressure channel, through the porous media, to the low pressure channel. The low pressure channel is open to atmosphere at one port. A schematic of the setup is shown in Figure 3.3.

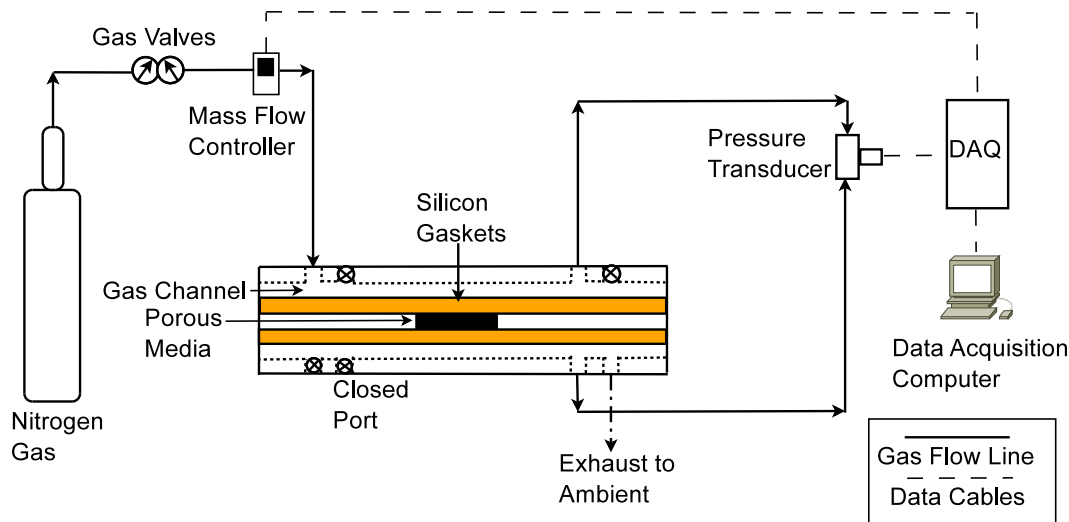


**Figure 3.3** – Experimental set-up to measure through-plane permeability

Compressed nitrogen (Praxair, UHP 5.0) is decompressed using a pressure regulator. Nitrogen at 50 psig is then made available to the mass flow controller. The mass flow controller (Cole-Parmer, model: RK-32907-69, range: 0-5lpm) is used to control the flow rates. The mass flow controller is connected to a computer via an RS-232 communication port. The gas experiences certain pressure drop as it travels through the porous media. The channels are connected to a pressure transducer (OMEGA, Model: - MMDDDB001BIV10H2A0T1A2) to measure the real time static pressure gradient at various flow rates. Data from the pressure transducer and mass flow controller is read via a data acquisition card (National Instruments USB 6221). LabWindows/CVI is used to communicate with the mass flow controller and log data from the mass flow controller and pressure transducer. The data is logged for 5 minutes (60 readings) for all flow rates to ensure steady state. Steady state is confirmed by ensuring that the standard deviation for pressure and mass flow rate is less than 3%.

Knudsen diffusivity is measured for GDL+MPL samples by conducting the permeability experiments with gases of very different mean paths, i.e., nitrogen and helium.

The permeability experiments are conducted subsequently without opening/closing the diffusion bridge. The pressure drop measured in both cases is different hence different permeability results. Since permeability is a geometric property of the porous media, it does not depend on the gas. The difference in the permeability results was attributed to Knudsen slip [46].

### 3.2.1.3 Through-plane diffusivity setup

For through-plane diffusivity experiments, the inlet of each channel in the diffusion bridge is connected to a different gas cylinder, i.e., one containing oxygen and another nitrogen. The two compressed gases, i.e., oxygen and nitrogen, are decompressed before passing through the mass flow controllers. Two mass flow controllers (Cole-Parmer, model: RK-32907-69, range: 0 - 5 lpm) are used to control the flow rate of gas in the channels. The outlet of the nitrogen channel is connected to a back pressure controller (Cole-Parmer, model: RK-00307OX, range: 0 - 100 psig) that is used to control the static pressure of the system. The oxygen channel outlet is connected to a differential pressure controller (Cole-Parmer, model: RK-00307TX, range: 0 - 500 pascals) which controls the static pressure difference between the two gas channels using a differential pressure gauge connected to each channel (See Figure 3.4). The differential pressure controller can be used to control convection.

Oxygen levels are measured at the outlet of the nitrogen channel downstream of the back pressure controller using a NEOFOX oxygen sensor (Ocean Optics, Model: FOSPOR-600-32MM, range: 0 - 10% in gas). The sensor is factory calibrated for a range of 0-10 %  $O_2$  and temperature 0 – 80° C. The range of temperature covered for calibration ensures the consistent readings during day to day temperature fluctuations. The calibration file is uploaded in the NEOFOX software before experiments are started. One point calibration is performed in-house, after the multi-point calibration file is uploaded. Pure nitrogen gas (UHP 5.0) is exposed to the sensor and the reading is recorded as zero. One point calibration is done every time before the experiments are started. Figure 3.5 shows the physical picture of the setup.

The convection to diffusion transport is controlled by controlling the oxygen gas channel pressure. The oxygen channel is set at higher pressure than the nitrogen channel in order to enhance oxygen mass transport through the porous media via convective transport. To control the differential pressure between channels, a differential pressure controller is installed in the nitrogen channel. The absolute pressure

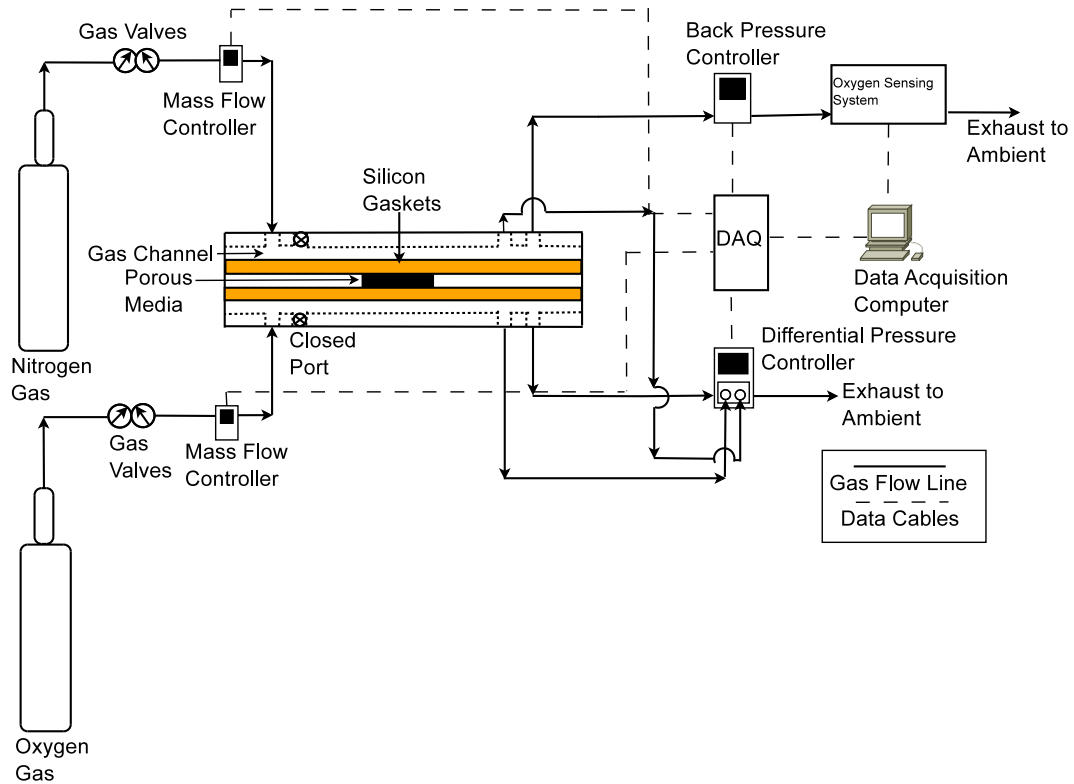


**Figure 3.4** – Experimental set-up to measure through-plane diffusivity

in the setup is controlled by a backpressure controller in the oxygen channel.

Mass flow controllers and pressure controllers are connected to a computer via RS-232 communication port. The data from pressure and mass flow controllers is read via a data acquisition card. LabWindows/CVI is used for data logging, storing the data in a Excel file. Data for every set-point is logged, at a rate of one reading every 5 seconds, for 5 minutes to ensure steady state. The software provided by the NEOFOX sensors also stores the detected oxygen mole fraction with time, temperature and pressure in a CVS file every 2 seconds. For every differential pressure, 150 readings for oxygen mole fraction are logged approximately. The average of the last eighty readings is reported. The real time is also recorded simultaneously from both CVI and NEOFOX software to map the data accurately for oxygen mole fraction to its corresponding differential pressure. The data from Excel and CVS files are merged manually and used for further analysis.

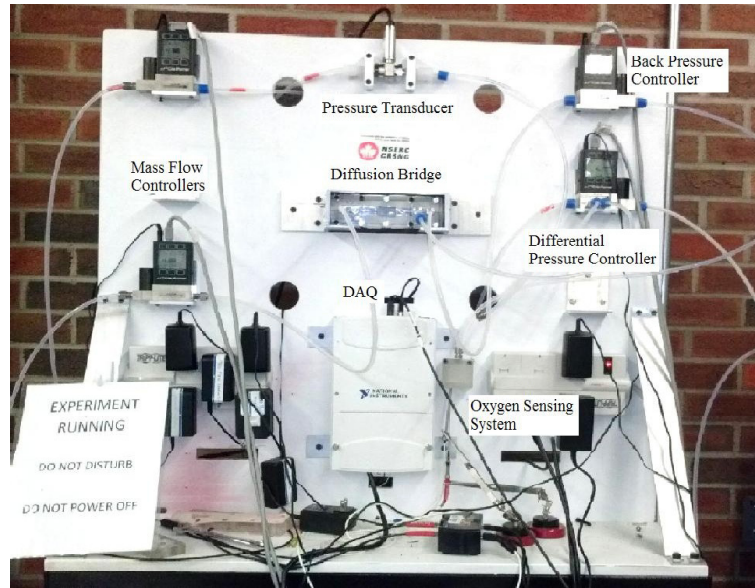


**Figure 3.5** – Experimental set-up

### 3.2.2 Experimental Conditions

For permeability and Knudsen diffusivity experiments, the mass flow rate of nitrogen gas is varied from 0-2 liters per minute (lpm) in 10 even intervals for a GDL sample, and 0.05-0.09 lpm in 5 even intervals for a GDL+MPL assembly. The low flow rates are maintained for a GDL+MPL assembly to be able to neglect any inertial effects. The ‘zeroth interval’, which corresponds to zero flow rate, is run for 5 minutes to estimate the offset of the pressure transducer. The offset is eliminated from the average readings at non zero flow rates. The average standard deviation for the selected flow rates from the MFC and pressure transducer is observed to be less than 3.0%.

For through-plane diffusivity experiments, the mass flow rate of both gases is set at 1 liters per minute (lpm). High flow rates are used to ensure the oxygen flux is quickly swept away in the nitrogen channel and the effects of diffusive boundary layers are minimized. The back pressure of the system is maintained at a gauge pressure 10 psig unless otherwise stated. The pressure difference between the two channels is varied from 2 - 10 Pa in 5 even intervals for a GDL sample and 20 - 100 Pa in 5 even intervals for a GDL+MPL sample. The low differential pressures are selected for GDLs to ensure the oxygen concentrations are into the limiting range of the oxygen sensor. The noise of differential pressure controller is estimated less than 2 Pa for GDLs, and less than 4 Pa for GDL+MPL assembly. The noise of differential pressure controller is the standard deviation of the last 40 readings at each setpoint.

Oxygen mole fraction is recorded at every pressure differential. The temperature of the system in both cases is ambient.

### 3.2.3 Materials

The effect of PTFE loading on through-plane permeability, and effective molecular and Knudsen diffusivities are studied. In order to study the effect of PTFE, GDL samples with different PTFE loading are analyzed, namely Toray 090 samples with 0, 10, 20 and 40% PTFE. The effect of an MPL on GDLs with different PTFE content is studied by testing Toray 090 samples with 10, 20 and 40% PTFE coated with the same MPL ink.

The porosity and pore size distribution of the samples was measured using a PoreMaster 33 Mercury Intrusion Porosimeter (Quantachrome Instruments). Figure 3.6 shows the pore size distribution of the samples. The average pore size of the GDL samples coated with an MPL is reduced. However, a distinct peak for an MPL in GDL-MPL samples is not clearly visible. The reason might be the significant intrusion of an MPL into the carbon substrate. To study the intrusion, side view of the GDL-MPL samples was obtained via SEM imaging (JOEL 6301F, Field Emission SEM). Figure 3.7 shows the image of a Toray 090(20% PTFE)+MPL sample. Clearly, the intrusion of MPL is through the whole GDL sample. Hence, an MPL cannot be isolated from the GDL, and a GDL-MPL assembly is considered one entity. Table 3.1 show the data for the GDL and GDL+MPL samples used in this study. The average readings for both thickness and porosity are used to analyze the results.

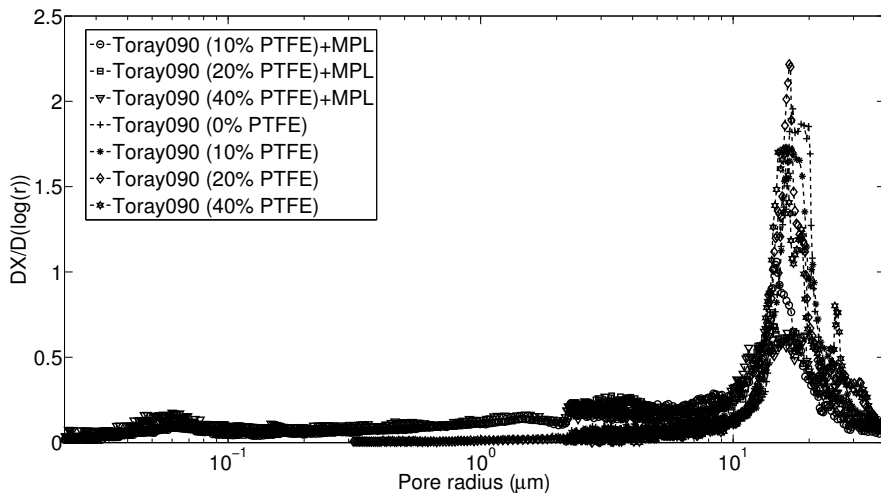


**Figure 3.6** – Pore size distribution of GDL and GDL-MPL samples

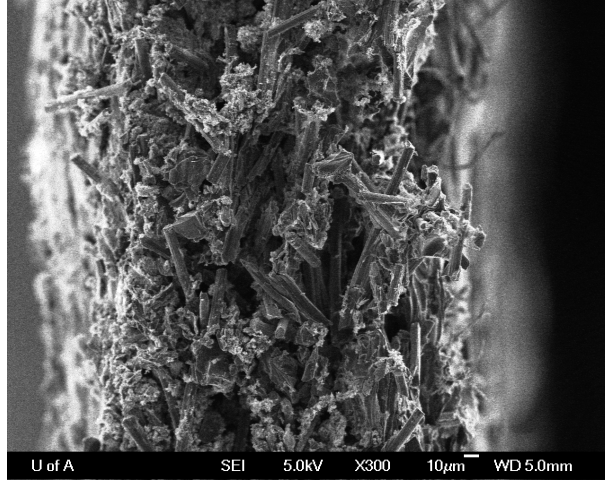


**Figure 3.7** – SEM of a Toray090 (20% PTFE)-MPL sample

**Table 3.1** – Thickness and Porosity (MIP) data of GDL samples

Sample	Thickness ( $\mu\text{m}$ )	Thickness after lamination ( $\mu\text{m}$ )	Porosity
SGL 34BA	$267 \pm 5$	$725 \pm 41$ (3 layers)	$0.77 \pm 0.03$
Toray090 (untreated)	$273 \pm 6$	$830 \pm 4$ (3 layers)	$0.76 \pm 0.02$
Toray090 (10% PTFE)	$290 \pm 4$	$874 \pm 19$ (3 layers)	$0.76 \pm 0.01$
Toray090 (20% PTFE)	$283 \pm 5$	$824 \pm 2$ (3 layers)	$0.69 \pm 0.01$
Toray090 (40% PTFE)	$282 \pm 4$	$814 \pm 16$ (3 layers)	$0.54 \pm 0.01$
Toray090 (10% PTFE)+MPL	$266 \pm 6$	$552 \pm 2$ (2 layers)	$0.75 \pm 0.02$
Toray090 (20% PTFE)+MPL	$269 \pm 7$	$549 \pm 10$ (2 layers)	$0.70 \pm 0.02$
Toray090 (40% PTFE)+MPL	$259 \pm 5$	$531 \pm 17$ (2 layers)	$0.58 \pm 0.01$

Unless otherwise specified, samples are tested with 3 layers stacked over each other. The aperture diameter is fixed as  $9.5\mu\text{m}$ . The results shown in section 3.4 are the average of three specimens cut from the same master sheet in random directions. The standard deviation corresponds to sample-to-sample variation in transport properties cut from same master sheet. Hence, results consist of errors from experimental equipments, directionality of fibers, and sample-to-sample effects.

### 3.3 Theory and Data Analysis

#### 3.3.1 Modified binary friction model

Pant et al. [77] recently proposed a modified version of the binary friction model proposed by Kerkhof et al. [78]. In one dimension, under isothermal conditions, the modified binary friction model is given as,

$$\frac{dp_i}{dx} = RT \sum_{j=1}^n \left( \frac{p_i N_j^{eff} - p_j N_i^{eff}}{p_t D_{ij}^{eff}} \right) - RT \left( D_{i,K}^{eff} + \left( \frac{\chi_i}{B_v} + \frac{M_i N_i^{eff}}{p_i B_l} \right)^{-1} \right)^{-1} N_i^{eff}, \quad (3.1)$$

where  $p_i$  is the partial pressure,  $N_i$  is the molar flux,  $M_i$  is the molecular mass,  $T$  is the temperature,  $R$  is the gas constant,  $D_{ij}^{eff}$  is the effective diffusion coefficient,  $D_i^K$  is the Knudsen diffusivity of species  $i$ ,  $B_v$  is the viscous permeability,  $B_l$  is the inertial permeability of porous media, and  $\chi_i$  is used to account for viscous friction, defined as,

$$\chi_i = M_i^{1/2} \left[ \frac{1}{\sum_{j=1}^n p_j M_j^{1/2}} \right] \left[ \frac{\sum_{j=1}^n x_j \eta_j^o}{\sum_{k=1}^n x_k \xi_{jk}} \right], \quad (3.2)$$

where  $\eta_j^o$  is the viscosity,  $x_j$  is the mole fraction of species  $j$  and  $\xi_{jk}$  is the Lennard-Jones interaction parameter for the species  $j$  and  $k$ .

For the mixture or when only one species is present, the Maxwell Stefan term in MBFM cancels out and equation (3.1) can be re-written as,

$$\frac{dp}{dx} = -RT \left( D_K^{eff} + \left( \frac{\eta}{p B_v} + \frac{MN}{p B_l} \right)^{-1} \right)^{-1} N, \quad (3.3)$$

Equation (3.3) is derived by adding the flux contribution due to Knudsen slip to the flux contributed by the viscous and inertial friction. In the case of GDLs, the Knudsen slip is assumed to be negligible, as also studied by Carrigy et al. [46]. Hence,  $D_K^{eff} \approx 0$ , and equation (3.3) yields

$$p \frac{dp}{dx} = -RT \left( \frac{\eta}{B_v} + \frac{MN}{B_l} \right) N, \quad (3.4)$$

The molar flux is assumed constant across the porous media, equation (3.4) is integrated from  $p = p_1$  to  $p_2$ , and  $x = 0$  to  $L$  such that

$$\frac{p_1^2 - p_2^2}{2RTL} = \frac{\eta}{B_v} N + \frac{M}{B_l} N^2, \quad (3.5)$$

where  $p_1$  and  $p_2$  are the mixture pressures across the porous media, and  $L$  is the width of the sample. Equation (3.5), known as the compressible form of Darcy - Forcheimer equation, is used to estimate the viscous and inertial permeability of the porous media for species  $i$ .

For a GDL + MPL sample, the average pore diameter is reduced considerably due to the intrusion of MPL in the carbon substrate. Carrigy et al. [46] studied the effect of PTFE on GDL+MPL assembly, and showed the effect of Knudsen slip to be significant. For sufficiently low velocities, the inertial effect in the porous media can be neglected. Equation (3.3) can then be written as,

$$\frac{dp}{dx} = -RT \left( D^K + \frac{pB_v}{\eta} \right)^{-1} N \Rightarrow \left( D_K^{eff} + \frac{pB_v}{\eta} \right) dp = -NRT dx \quad (3.6)$$

Integrating equation (3.6) for  $p = p_1$  to  $p_2$ , and  $x = 0$  to  $L$ , and substituting molar flux,  $N = \frac{p_1 v_1}{RT}$ , equation (3.6) is solved to:

$$v_1 = \frac{B_v}{2\eta L} \left( \frac{p_1^2 - p_2^2}{p_1} \right) + \frac{D_K^{eff}}{L} \left( \frac{p_1 - p_2}{p_1} \right), \quad (3.7)$$

where  $v_1$  is the velocity of the gas at the inlet of the porous media. The Knudsen diffusivity,  $D_K^{eff}$ , is also mathematically defined as,

$$D_K^{eff} = \frac{\epsilon}{\tau} \frac{0.89d_p}{3} \sqrt{\frac{8RT}{\pi M}} = \frac{0.89d_p^{eff}}{3} \sqrt{\frac{8RT}{\pi M}}, \quad (3.8)$$

where  $d_p^{eff}$  is the average pore diameter of the porous media. Equation (3.7) and (3.8) are used to estimate the viscous permeability and Knudsen diffusivity for a GDL + MPL assembly.

In summary, equation (3.5) is used for a GDL sample, and, for sufficiently low velocities, equations (3.7) and (3.8) are used for a GDL + MPL sample.

### 3.3.2 Model implementation

To estimate viscous and inertial permeability of a GDL sample, the inlet velocity vs pressure drop data is obtained experimentally. The molar flux is obtained using  $N = \frac{p_1 v_1}{RT}$ , where  $v_1$  is the inlet velocity and  $p_1$  is the inlet pressure. The inlet velocity is calculated as,  $v = \frac{4\dot{V}}{\pi d_{ap}^2}$ . The volume flow rate,  $\dot{V}$ , is controlled by a mass flow controller, and  $d_{ap}$  is the aperture diameter, fixed as 9.5 mm. The experimental data is fit to equation (3.5) using MATLAB to extract transport parameters, i.e.,  $B_v$  and  $B_l$ . The function `fitype` is used for fitting. `fitype` uses a least squares regression technique to minimize the residual. The coefficient of regression for all the fittings is found to be greater or equal to 0.99.

To estimate Knudsen diffusivity and viscous permeability for a GDL + MPL sample, inlet velocity vs pressure drop data is obtained experimentally for two different gases with very different mean paths, i.e., nitrogen and helium. A loop is run for pore diameter  $d_p$ , and Knudsen diffusivity is calculated for both gases at each pore diameter. For every pore diameter, viscous permeability  $B_v$  is fitted in equation (3.7) using the combined experimental data measured for nitrogen and helium. The function `lsqcurvefit` in MATLAB is used for fitting. `lsqcurvefit` also uses a least squares regression technique to minimize the residual. The residual is minimized, and the corresponding  $d_p$  and  $B_v$  is accepted as a best fit.

For effective diffusivity, molar fraction vs  $\Delta p$  data is obtained experimentally. In order to estimate  $N_{O_2}$ , first, the moles of oxygen in the nitrogen channel are calculated by adding the moles of gas entering the nitrogen channel due to convection, and multiplying the summation with the molar fraction obtained from oxygen sensor. The moles of gas from nitrogen channel is calculated as,  $n_1 = \frac{\rho_{N_2} \dot{V}}{M_{N_2}}$ , where  $\rho_{N_2}$  is the density of nitrogen at 10 psig and  $\dot{V}$  is the volume flow rate set by mass flow controller. The moles of gas from porous media are calculated by,  $n_2 = \frac{p}{RT} Av$ , where  $p$  is the pressure in the oxygen channel,  $A$  is the area of the GDL, and  $v$  is the velocity of the oxygen across porous media, calculated as,  $v = \frac{B_v \Delta p}{\eta L}$  in GDL samples, where  $\eta \approx \eta_{O_2}$ , and  $v = \frac{B_v}{2\eta L} \frac{p_1^2 - p_2^2}{p_1} + \frac{D_K^{eff}}{L} \frac{p_1 - p_2}{p_1}$  in GDL-MPL samples, where  $p_1$  and  $p_2$  are the pressure of gas at inlet and outlet of the porous media. Then,  $N_{O_2}$  is estimated as,  $N_{O_2} = x \times \frac{n_1 + n_2}{A}$ .

For the MBFM, equations (3.1) and (3.2) are implemented in solver `bvp4c`. The ratio of effective to molecular diffusivity or diffusibility is considered a fitting parameter. A loop is run for a range of diffusibility, and residuals are plotted against each diffusibility. The residuals are estimated as the sum of the squares of the difference between the experimental and computed oxygen flux for each diffusibility. The residual is minimized and the corresponding diffusibility is accepted as a best fit. MBFM requires four boundary conditions, which are the densities of gases in the channels, i.e.,  $\rho_{O_2} = \frac{p_{O_2} M_{O_2}}{RT}$ ,  $\rho_{N_2} = 0$  in the oxygen channel, and  $\rho_{N_2} = \frac{p_{N_2} M_{N_2}}{RT}$ ,  $\rho_{O_2} = 0$  in the nitrogen channel.

## 3.4 Results and discussion

### 3.4.1 Through-plane permeability

Various commercial GDLs are tested, i.e., SGL 34BA, Toray 090 samples treated with 0, 10, 20 and 40% PTFE, and Toray 090 samples coated with MPL with 10, 20 and 40% PTFE loadings.

**3.4.1.0.1 Sensor error** A similar methodology, used in section 2.4.1.1.1, is implemented to estimate the error influenced by the different sensors used in experiments. To maximize the error in the viscous permeability results, the inertial permeability is neglected in the governing equation (equation (3.5)). The equation is reduced to,

$$\frac{p_1^2 - p_2^2}{2RTL} = \frac{\eta}{B_v} N, \quad (3.9)$$

The molar flux of the gas is estimated as,

$$N = \frac{pv}{RT}, \quad (3.10)$$

where  $v$  is the velocity of the gas. Velocity of the gas at the inlet of the sample is calculated as,

$$v = \frac{4V}{\pi d_{ap}^2}, \quad (3.11)$$

where  $V$  is the volume flow rate, and  $d_{ap}$  is the aperture diameter punched in the lamination sheet.

Equation (3.9) is differentiated both sides, and terms are rearranged with the assumption,  $p_1^2 - p_2^2 \simeq p_1^2$ , equation (3.9) reduces to,

$$2 \left| \frac{dp_1}{p_1} \right| = \left| \frac{dN}{N} \right| + \left| \frac{dL}{L} \right| + \left| \frac{dB_v}{B_v} \right| \quad (3.12)$$

To find the error in the molar flux, equations (3.10) and (3.11) are differentiated both sides, and terms are rearranged, the expression for error in molar flux is substituted in equation(3.12). The final expression for the maximum error in the viscous permeability reduces to,

$$\left| \frac{dB_v}{B_v} \right| = 3 \left| \frac{dp_1}{p_1} \right| + \left| \frac{dV}{V} \right| + 2 \left| \frac{dd_{ap}}{d_{ap}} \right| + \left| \frac{dL}{L} \right| \quad (3.13)$$

The error in the GDL thickness and aperture diameter is assumed as 10 microns. The error in inlet pressure  $p_1$ , and volume flow rate  $V$  are corresponds to the error in the readings by pressure transducer and mass flow controller, respectively. The error

in pressure transducer and mass flow controller from their manufacturers are given as  $\pm 0.05\%$  and  $\pm 0.8\%$  of their readings, respectively. Substituting the errors in the equation (3.13), the aperture diameter of the sample is 9.5mm, to maximize the error, minimum thickness of the sample is considered i.e. 826 microns.

$$\left| \frac{dB_v}{B_v} \right| = 3 \times 0.0005 + 0.008 + 2 \frac{10}{9500} + \frac{10}{826} \Rightarrow \left| \frac{dB_v}{B_v} \right| = 0.0237 \quad (3.14)$$

The maximum error in the viscous permeability results is calculated as 2.37%.

**3.4.1.0.2 Test variability** The reliability of the setup is determined by assembling a diffusion bridge with a SGL 34BA sample and running the same experiment three times without opening/closing the diffusion bridge. The pressure gradient versus velocity data is obtained from the setup for all three sets of readings. Figure 3.8 shows the three set of readings, and fit compressible form of Darcy - Forchheimer equation. The standard deviation in the viscous permeability results is estimated as 1.35%.

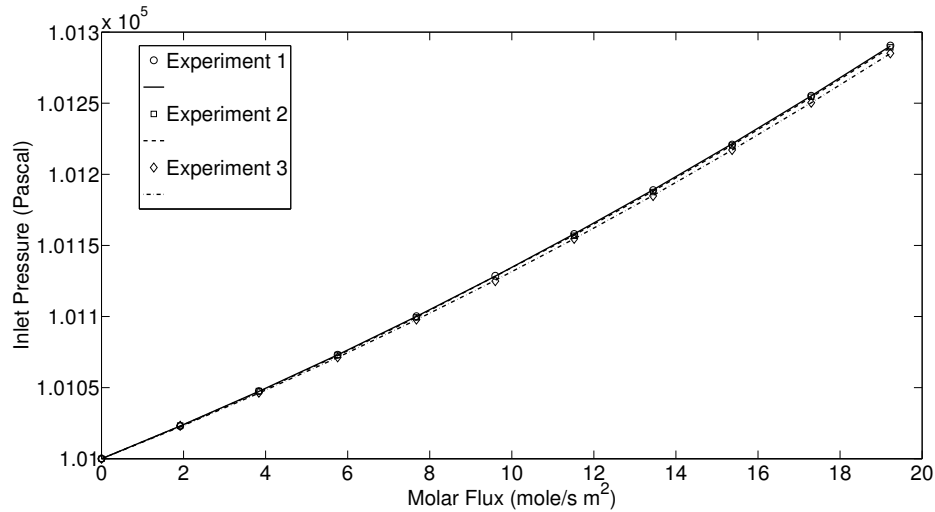


**Figure 3.8** – Test repeatability for a 34BA sample

Figure 3.9 shows the actual and average flow rate, and pressure gradient readings measured by MFC and pressure transducer, respectively. Clearly, steady state is observed at each setpoint, and fluctuations are small compared to the changes observed due to the selected setpoints.

**3.4.1.0.3 Variation within aperture diameter** The aperture diameter punched in the lamination sheet is varied to study the effects on the permeability results. The three layers of sample SGL 34BA were stacked over each other in each case, and

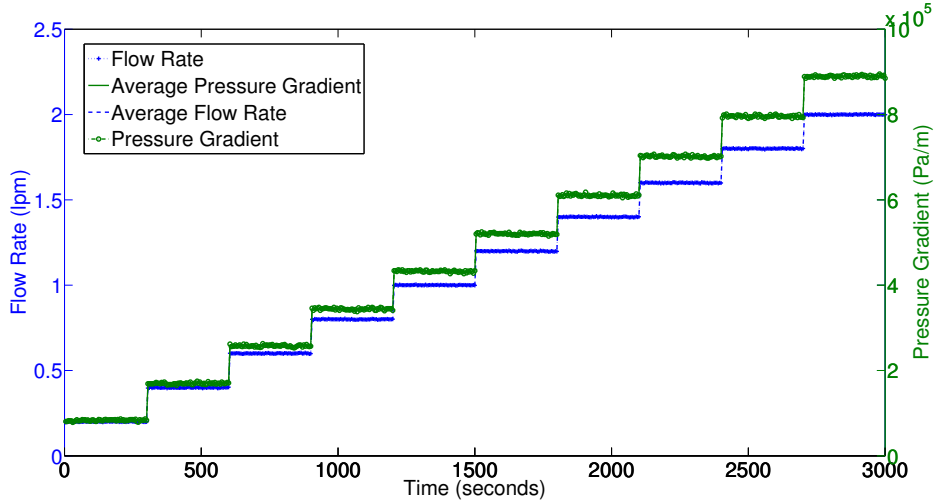


**Figure 3.9** – Oscillatory and average volume flow rate, and pressure gradient readings for a 34BA sample

four different aperture diameters were punched in the lamination sheet. Table 3.2 shows the results. The standard deviation of the viscous permeability results for diameters larger than 4mm is obtained as 14.46%. A similar standard deviation is obtained for sample-to-sample variation of SGL 34BA (see Table 3.4). Therefore, the difference from aperture diameters is within sample-to-sample variability. For 95% confidence interval, a Student’s t-test justifies that results obtained with different aperture diameter and sample-to-sample are not significantly different from each other. Therefore, the aperture diameter effect is considered insignificant. The aperture diameter was fixed as 9.5 mm for the results discussed in this article.

**Table 3.2** – Through-plane permeability for sample SGL 34BA at various aperture diameters

Diameter (mm)	$B_v \times 10^{-11}(m^2)$
4.69	2.0
6.80	1.42
7.80	1.62
9.50	1.59

**3.4.1.0.4 Variation with number of layers** The number of layers of a SGL 34BA were varied to study the effects on the permeability results. A SGL 34BA was tested with single, two, three and four layers stacked over each other. Three repli-

cates of each stack was tested. The aperture diameter was fixed as 9.5mm. Table 3.3 shows the results. The standard deviation for the replicates in the permeability results were obtained as 29.91%, 18.46%, 11.01% and 32.12% for single, two, three and four layers, respectively. A Student's t-test is performed to compare the results obtained for different number of layers. For 95% confidence interval, the results were not found to be significantly different. The three layers showed the best repeatability, hence three layers were stacked for all the GDL samples tested in this study.

Due to the unavailability of the same master sheet used to obtain results in Table 3.2 and 3.4 for SGL 34BA, different master sheet was used in this study. The difference in the results corresponds to the anisotropic nature of the GDL samples which is significant from one master sheet to another.

**Table 3.3** – Through-plane permeability for sample SGL 34BA for various layers

No of layers	$B_v \times 10^{-11}(m^2)$
1	1.07±0.32
2	1.30±0.24
3	1.09±0.12
4	1.37±0.44

### 3.4.1.1 Effect of PTFE on through-plane permeability for GDL samples

The effect of PTFE was studied by testing Toray 090 samples with 0, 10, 20 and 40% PTFE. Compressible form of Darcy - Forcheimer equation (equation (3.5)) is used to estimate the permeability. Figure 3.10 shows the inlet pressure vs molar flux curves for the Toray 090 samples. The inlet pressure increases with higher PTFE content at the same velocity. Table 3.4 shows the permeability results for the tested samples. The standard deviation was obtained by testing three replicates of the same sample cut from the same master sheet. The results are compared with our previous results and literature, and found in good agreement. The slight difference between the results is due to sample variability, and errors influenced by chip preparation. Results show that permeability decreases with increasing content of PTFE except for Toray 090 (10% PTFE) which showed higher permeability than untreated sample. The small amount of PTFE does not seem to vary the geometric properties significantly. The permeability decreases with high PTFE content due to the spread of PTFE binders over the intersection of fibers thereby reducing pore size and porosity.

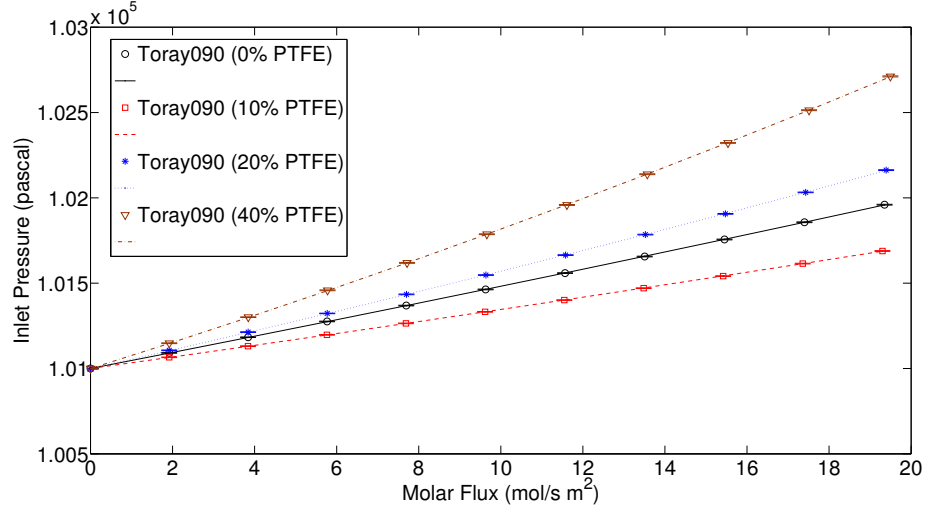


**Figure 3.10** – Inlet pressure vs molar flux for Toray 090 samples

**Table 3.4** – Through-plane permeability for sample SGL 34BA and Toray 090 (0, 10, 20 and 40% PTFE)

Sample	$B_v \times 10^{-11} (m^2)$	$B_l \times 10^{-5} (m)$	Literature ( $B_v \times 10^{-11}$ )
SGL 34 BA	$2.21 \pm 0.55$	$0.27 \pm 0.12$	1.54 [46], 1.63 [14], 2.50 - 2.74 [49]
Toray 090 (0% PTFE)	$0.80 \pm 0.05$	$0.39 \pm 0.11$	1.10 [46], 0.90 [14]
Toray 090 (10% PTFE)	$1.13 \pm 0.12$	$0.51 \pm 0.10$	0.90 [46]
Toray 090 (20% PTFE)	$0.66 \pm 0.06$	$0.22 \pm 0.04$	0.73 [46]
Toray 090 (40% PTFE)	$0.35 \pm 0.12$	$0.05 \pm 0.03$	0.27 [46]

The permeability is often predicted by Carman-Kozeny equation [29], i.e.

$$K = \frac{d_f^2 \epsilon^3}{16 K_{CK} (1 - \epsilon)^2}, \quad (3.15)$$

where  $d_f$  is the fiber diameter,  $\epsilon$  is the porosity and  $K_{CK}$  is known as the Carman-Kozeny constant which is considered a fitting parameter for GDL samples. The permeability results for Toray 090 (10, 20 and 40% PTFE) are fitted in equation (3.15) to extract Carman-Kozeny constant,  $K_{CK}$ . The fiber diameter for Toray 090 samples is used as  $9.2 \mu m$ . The constant is estimated as  $3.35 \pm 0.31$ . Figure 3.11 shows the comparison of Carman-Kozeny equation with the experimental data.

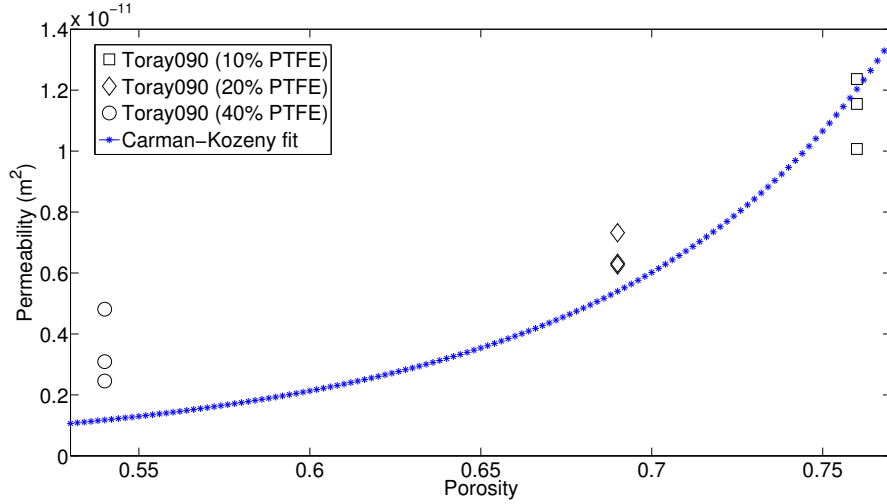


**Figure 3.11** – Carman-Kozeny fit to the experimental data

### 3.4.1.2 Effect of PTFE on through-plane permeability and Knudsen diffusivity for GDL + MPL samples

Based on Knudsen number, flow in porous media are classified in different regimes. The Knudsen number is mathematically defined as [46],

$$K_n = \frac{\lambda}{d_p} \quad (3.16)$$

where  $\lambda$  is the mean free path length of the gas and  $d_p$  is the average pore diameter of porous media.

No slip boundary condition is valid only in the continuum regime, when the Knudsen number is less than 0.001. A slip boundary condition is required between continuum and free molecular flow, i.e.  $0.001 \leq K_n \leq 10$  [46]. The Knudsen slip in GDLs was assumed to be negligible, as also shown by Carrigy et al. [46]. For GDLs coated with an MPL, the average pore diameter is comparable to the mean free path of the gas, and the Knudsen effects become important. The Knudsen slip in GDL+MPL assemblies in the through-plane direction was studied by measuring gas permeability with two gases of very different mean free paths, i.e. nitrogen and helium. Low flow rates were maintained in the experiments to ensure the inertial permeability effects were negligible. Maximum velocity used in the experiments is 0.02 m/s. For a Toray 090 (untreated) sample, the pressure drop contribution for nitrogen from Forcheimer effect at 0.02 m/s is estimated to be less than 0.5%. Hence, the Forcheimer effect can be neglected. Equations (3.7) and (3.8) are used to estimate the viscous permeability

and Knudsen diffusivity of the samples.

The effect of PTFE was studied by testing Toray 090 (10, 20 and 40% PTFE) coated with an MPL. Figure 3.12 shows the inlet velocity vs inlet pressure curves for nitrogen and helium for a Toray 090 (10% PTFE) coated with an MPL, obtained using experimental data fit with equation 3.7. Table 3.5 shows the viscous permeability and pore diameter results obtained for the samples, and compared with our previous results. The results are in good agreement. The slight difference in the results is due to the samples used from different master sheets. Since PTFE reduces the pore diameters in GDLs, as also shown in Table 3.5, the viscous permeability was found to decrease with PTFE.

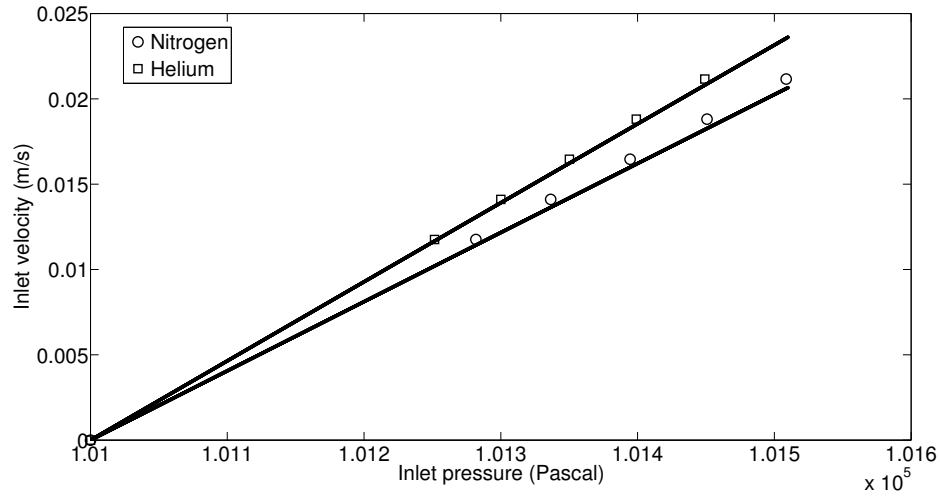


**Figure 3.12** – Inlet velocity vs inlet pressure for nitrogen and helium for a Toray 090 (10% PTFE)+MPL assembly

**Table 3.5** – Through-plane permeability and pore diameter for sample Toray 090 (10, 20 and 40 % PTFE) with MPL

Sample	$B_v \times 10^{-13} (m^2)$	$d_p (\mu m)$	Literature ( $B_v \times 10^{-13}$ )	Literature ( $d_p$ )
Toray 090 (10% PTFE)	$3.04 \pm 1.27$	$2.15 \pm 0.62$	$3.60 \pm 0.80$ [46]	$1.80 \pm 0.20$ [46]
Toray 090 (20% PTFE)	$1.98 \pm 0.54$	$1.47 \pm 0.22$	$1.10 \pm 0.20$ [46]	$0.90 \pm 0.10$ [46]
Toray 090 (40% PTFE)	$0.80 \pm 0.58$	$0.50 \pm 0.08$	$0.40 \pm 0.10$ [46]	$0.38 \pm 0.08$ [46]

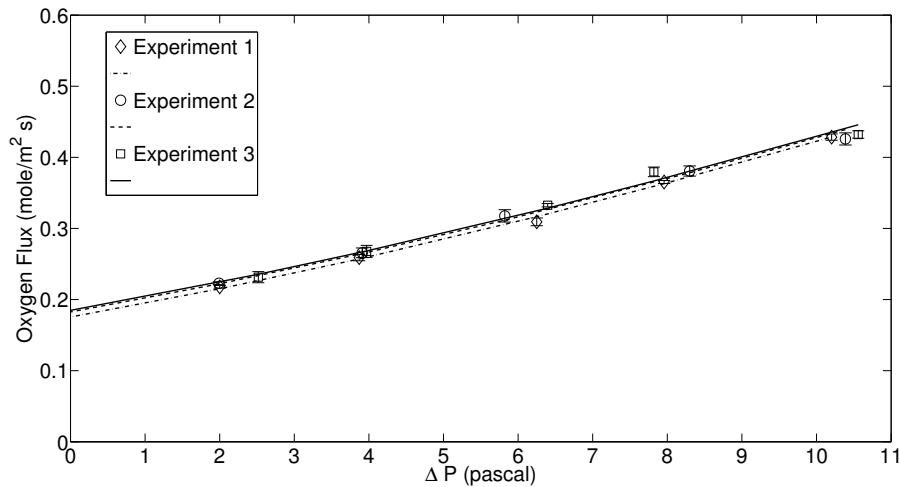
### 3.4.2 Through-plane effective diffusivity

A diffusion bridge is created between the pair of oxygen and nitrogen gas. Various commercial GDL samples are tested viz SGL 34BA and Toray 090 with 0, 10, 20 and

40% PTFE loadings, and Toray 090 with 10, 20 and 40% PTFE loadings coated with a MPL.

### 3.4.2.1 Error analysis

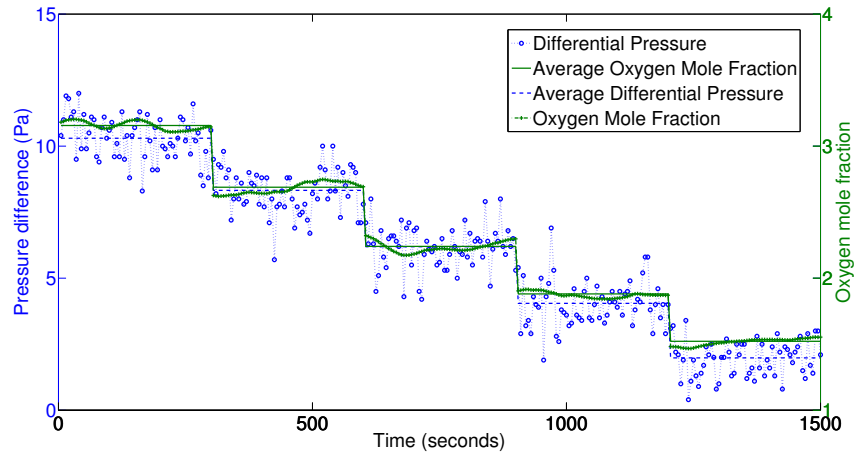
**3.4.2.1.1 Test variability** The reliability of the setup is determined by assembling a diffusion bridge with a Toray 090 (untreated) sample and running the same experiment 3 times without opening/closing the diffusion bridge. The oxygen molar flux versus differential pressure data is obtained from the setup for all three sets of readings. Figure 3.13 shows the three set of readings, and fit with Fick's and Darcy's model. The standard deviation for diffusibility is estimated as 2.71%.



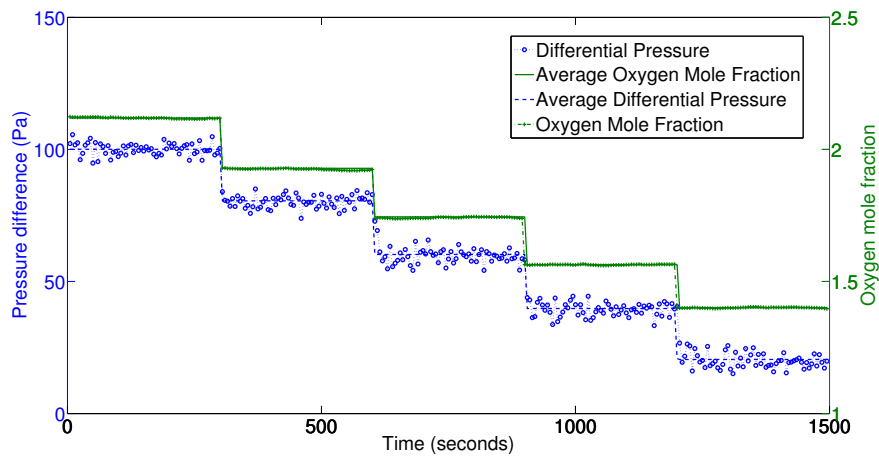
**Figure 3.13** – Test repeatability for a Toray 090 (10 % PTFE) sample

Figure 3.14 and 3.15 show the average and actual differential pressure, and oxygen concentration readings for a Toray 090 (10% PTFE) and Toray 090 (10% PTFE)+MPL sample, respectively. The average values are estimated by averaging the last sixty measured readings for oxygen sensor, and all the readings from differential pressure controller. Differential pressure fluctuations led to fluctuations in oxygen sensor. The fluctuations in a GDL sample are observed high than a GDL-MPL entity due to its high permeability. As shown in the figures, the fluctuations are small compared to the changes due to differential pressure setpoints. Even with the observed fluctuations, the results were found repeatable.

**3.4.2.1.2 Variation with channel flow rate** The boundary layer effects are studied by measuring diffusion at different flow rates without opening/closing the



**Figure 3.14** – Oscillatory and average differential pressure, and oxygen concentration readings for a Toray 090 (10% PTFE) sample



**Figure 3.15** – Oscillatory and average differential pressure, and oxygen concentration readings for a Toray 090 (10% PTFE)+MPL sample

diffusion bridge. Sample Toray 090 (10% PTFE) is tested at 0.5, 1, 1.5 and 2 lpm, and diffusibility is estimated. The diffusibility results at 0.5, 1, 1.5 and 2 lpm is estimated as  $0.200 \pm 0.013$ ,  $0.197 \pm 0.024$ ,  $0.215 \pm 0.002$ , and  $0.219 \pm 0.002$ , respectively. The standard deviation is obtained by repeating the experiment 5 times at each flow rate without opening/closing the diffusion bridge. A Student's t-test is performed to compare the results obtained for different flow rates. For 95% confidence interval, results were not found to be significantly different.

### 3.4.2.2 Validation studies

**3.4.2.2.1 Different pair of gases** The diffusibility is a geometric property of porous media, hence not expected to vary with a pair of experimental gases chosen. Sample Toray 090 (10% PTFE) is tested with two pair of gases i.e.  $N_2 - O_2$  and  $Ar - O_2$ . For each pair of gases, experiments are repeated 5 times. The bulk diffusion coefficient for  $N_2 - O_2$  and  $Ar - O_2$  at ambient conditions is used as  $2.065 \times 10^{-5}$  and  $1.95 \times 10^{-5}$  m<sup>2</sup>/s respectively. Diffusibility for  $N_2 - O_2$  and  $Ar - O_2$  is estimated as  $0.197 \pm 0.024$  and  $0.20 \pm 0.023$ , respectively. For 95% confidence interval, a Student's t-test justifies that diffusibility are not significantly different from each other.

A similar study was performed with  $He - O_2$ . The diffusibility results for  $He - O_2$  were found to be significantly different, which was unexpected. Further work is necessary to understand this effect.

**3.4.2.2.2 Effect of absolute pressure** Kinetic theory of gases predicts that the product of absolute pressure and molecular diffusivity is constant. Mathematically,

$$PD_{bulk} = constant. \quad (3.17)$$

The experimental setup is verified by changing the absolute pressure of the diffusion bridge in the nitrogen channel to 10, 15 and 20 psig using a back pressure controller for a Toray 090 (10% PTFE) sample. Diffusibility is a geometric property of porous media and it showed not vary with the absolute pressure. Experimentally, the diffusibilities at different pressures were obtained as  $0.197 \pm 0.024$ ,  $0.178 \pm 0.008$ , and  $0.186 \pm 0.023$  at 10, 15 and 20 psig, respectively. The standard deviation is obtained by repeating the experiment 5 times at each back pressure. For 95% confidence interval, a Student's t-test suggests that diffusibility results at 10, 15 and 20 psig are not significantly different from each other.

### 3.4.2.3 Effect of PTFE on through-plane diffusivity in GDL samples

The effect of PTFE on diffusivity is studied by testing Toray 090 samples with 0, 10, 20 and 40% PTFE. Diffusibility is estimated using MBFM (equation (3.1)). For GDLs, Knudsen diffusivity is assumed to be zero. The permeability values were used from the results section of the permeability for GDLs. Figure 3.16 shows the oxygen molar flux vs differential pressure curves obtained from MBFM for best fit of diffusibility. The flux was found to decrease with PTFE content at zero differential pressure suggesting that effective diffusivity decreases with PTFE content. At non-zero differential pressures, oxygen molar flux is measured lower as PTFE content increases. As discussed in section 3.4.1, high PTFE content decreases the permeability, hence the molar flux due to convection also decreases.

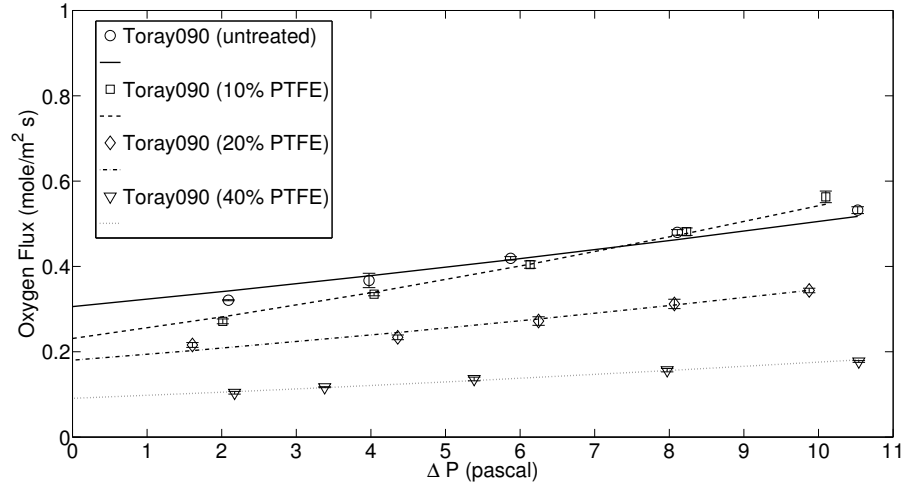


**Figure 3.16** – Oxygen molar flux vs differential pressure across porous media for GDL samples

Table 3.6 shows the diffusibility results, and a comparison to previous literature data. Though the tested samples are Toray 090, results are compared with Toray 060 and Toray 120. The Toray 060, 090 and 120 are known to have similar porosity, hence comparable transport properties. The samples differ only in physical properties such as thickness and tensile strength. The results were found in good agreement with literature. Note that the experimental setup used here is completely different than any of the previous methods used thereby validating previous results. The diffusibility was estimated to decrease with higher PTFE content. As already discussed, PTFE binders block the pores of the porous media, thereby reduces its size.

**Table 3.6** – Through-plane diffusibility for Toray 090 (0, 10, 20 and 40% PTFE)

Sample	Diffusibility	Literature (Toray 060 [16], Toray 120 [54, 70])
Toray 090 (0% PTFE)	$0.237 \pm 0.072$	0.24-0.34 [16], 0.25-0.33 [54], 0.27-0.42 [70]
Toray 090 (10% PTFE)	$0.209 \pm 0.064$	0.28-0.29 [54], 0.20-0.32 [70]
Toray 090 (20% PTFE)	$0.153 \pm 0.035$	0.14-0.19 (30% PTFE) [16], 0.23-0.25 [54], 0.19-0.30 [70]
Toray 090 (40% PTFE)	$0.073 \pm 0.026$	0.05 (60% PTFE) [16], 0.13-0.15 [54], 0.08-0.12 [70]

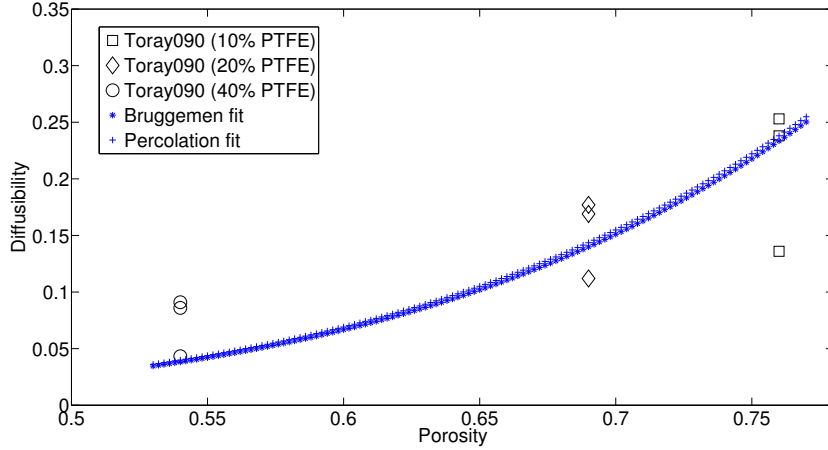


**Figure 3.17** – Bruggemen and percolation model fit in diffusibility results

To predict the diffusibility in porous media, various models have been proposed. A Bruggeman type correlation [50] and Tomadakis - Sotirchos's percolation theory [33] based models are widely accepted. Mathematically, the empirical correlations of the models are defined as:

$$D_{eff}/D_{bulk} = \epsilon^a \text{(Bruggeman Correlation)}, \quad (3.18)$$

and,

$$D_{eff}/D_{bulk} = \epsilon \left( \frac{\epsilon - \epsilon_{th}}{1 - \epsilon_{th}} \right)^\alpha \text{(Tomadakis - Sotirchos Model)}, \quad (3.19)$$

where  $a$ ,  $\epsilon_{th}$  and  $\alpha$  are considered fitting parameters. In the case of Bruggemen,  $a$  is usually taken as 1.5. The diffusibility results are fitted in equations (3.18) and (3.19) in MATLAB. The function `lsqcurvefit` is used for fitting. Figure 3.17 shows the fitting of the experimental data with the models. The fitting parameter  $a$  in Bruggmen correlation is estimated as  $5.3 \pm 0.81$ , and the percolation parameters,  $\epsilon_{th}$  and  $\alpha$  are estimated as  $(8.83 \pm 5.93) \times 10^{-8}$  and  $4.23 \pm 0.87$ , respectively. Note that the common value of 1.5 in Bruggemen correlation is not suitable.

### 3.4.2.4 Oxygen flux distribution in a GDL sample

Oxygen flux distribution is studied in a Toray 090 (untreated) sample. The thickness, permeability and effective molecular diffusivity of the sample was measured as  $826\mu\text{m}$ ,  $0.75 \times 10^{-11} \text{ m}^2$ , and  $0.33 \times 10^{-5} \text{ m}^2/\text{s}$ , respectively. Figure 3.18 shows the oxygen concentration curves across the sample at various differential pressure. At zero pressure difference, oxygen concentration decreases linearly. At non zero pressure difference, the concentration profiles are curved due to the additional flux via convection. The oxygen mole fraction is measured to be less than 2% in the nitrogen channel and quickly diluted due to the entrainment by the nitrogen flow, hence the oxygen partial pressure is approximated as zero as a boundary condition. Therefore, oxygen concentration and convective flux is zero at the outlet of the porous media.

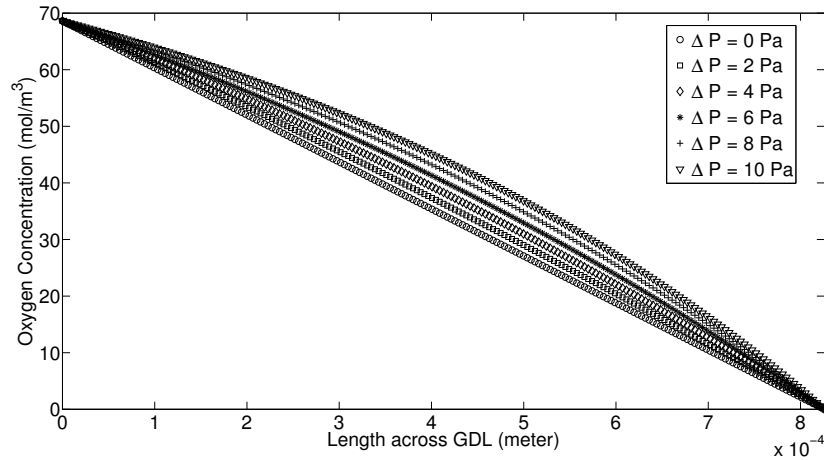


**Figure 3.18** – Oxygen concentration across porous media at various differential pressures

Figure 3.19 and 3.20 show the oxygen flux distribution via convection and diffusion, respectively. At zero differential pressure, convective flux is zero, hence total flux corresponds to pure diffusive flux. At the inlet of the porous media, diffusive flux dominates the convection for differential pressures less than 6 Pa. The diffusive flux contribution decreases from 79% to 31% as pressure difference increases from 2 to 10 Pa. The total oxygen flux increases from 0.27 to  $0.47 \text{ mol}/\text{m}^2\text{s}$  for pressure difference increasing from 0 to 10 Pa. At any point in the porous media, the total oxygen flux is constant. Due to the comparable contribution from both convective and diffusive flux, the experimental conditions chosen are suitable.

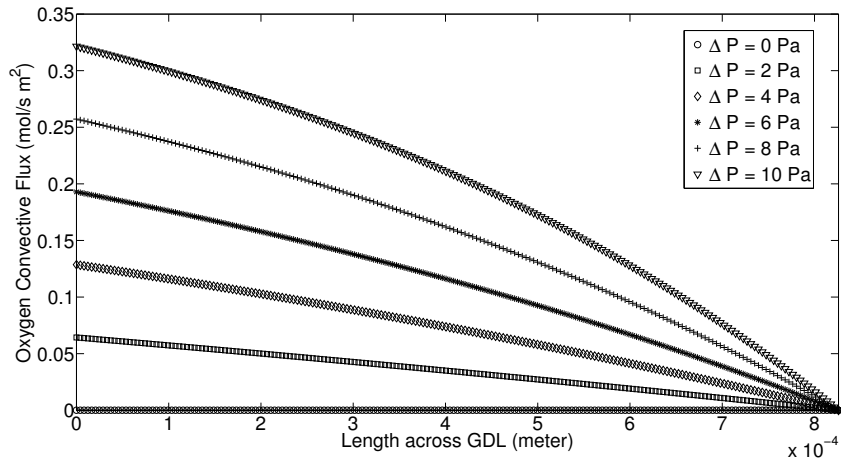


**Figure 3.19** – Oxygen convective flux across porous media at various differential pressures

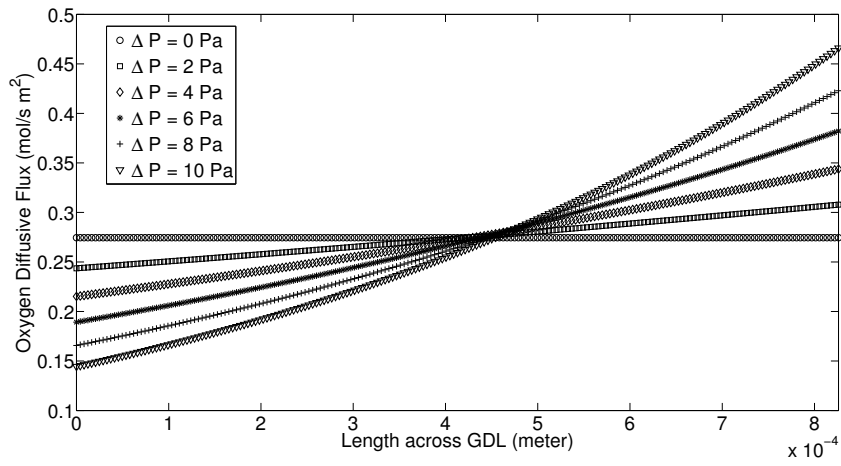


**Figure 3.20** – Oxygen diffusive flux across porous media at various differential pressures

### 3.4.2.5 Effect of PTFE on through-plane diffusivity in GDL-MPL samples

The effect of PTFE on GDL+MPL assemblies was studied by testing Toray 090 samples with 10, 20 and 40% PTFE coated with an MPL. Knudsen diffusivity plays an important role for GDL+MPL samples as discussed in section 3.4.1.2. Since Fick - Darcy model does not account for Knudsen slip, MBFM was implemented for a GDL+MPL assembly. The viscous permeability, and pore diameter to calculate Knudsen diffusivity was obtained in Table 3.5.

Figure 3.21 shows the oxygen molar flux vs differential pressure curves obtained from MBFM. The oxygen molar flux is measured to decrease at zero and non-zero pressure difference with high PTFE content. Low flux at zero pressure difference, also known as pure diffusive flux, suggests low diffusibility with higher PTFE content. Also, for non-zero differential pressures, low flux is measured due to low permeability and small pore diameter at higher PTFE content.

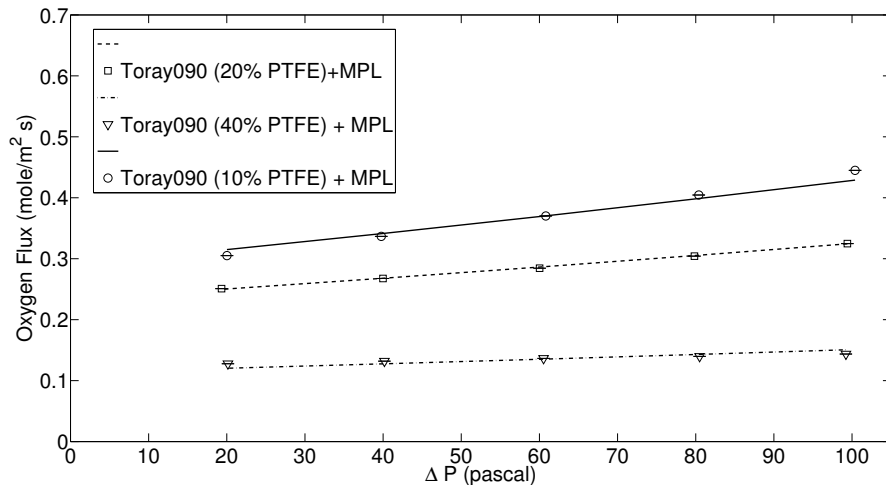


**Figure 3.21** – Oxygen molar flux vs differential pressure across porous media for GDL+MPL samples

In order to understand the contribution of Knudsen diffusion in the overall diffusion process, the best fit for diffusibility was obtained from MBFM assuming Knudsen diffusivity as zero. Figure 3.22 shows the comparison of the best fit of experimental data in MBFM, with and without Knudsen diffusion, for a Toray 090 (10% PTFE)+MPL sample. The estimated diffusibility is higher when Knudsen diffusion is not considered. The diffusibility increases from 0.15 to 0.16 due to the additional flux

**Table 3.7** – Through-plane diffusibility for Toray 090 (10, 20 and 40% PTFE) with MPL

Sample	Diffusibility
Toray 090 (10% PTFE)+MPL	$0.181 \pm 0.024$
Toray 090 (20% PTFE)+MPL	$0.145 \pm 0.006$
Toray 090 (40% PTFE)+MPL	$0.077 \pm 0.006$

measured via Knudsen diffusion. Therefore, the contribution of Knudsen diffusion in the overall diffusion process is not very significant.

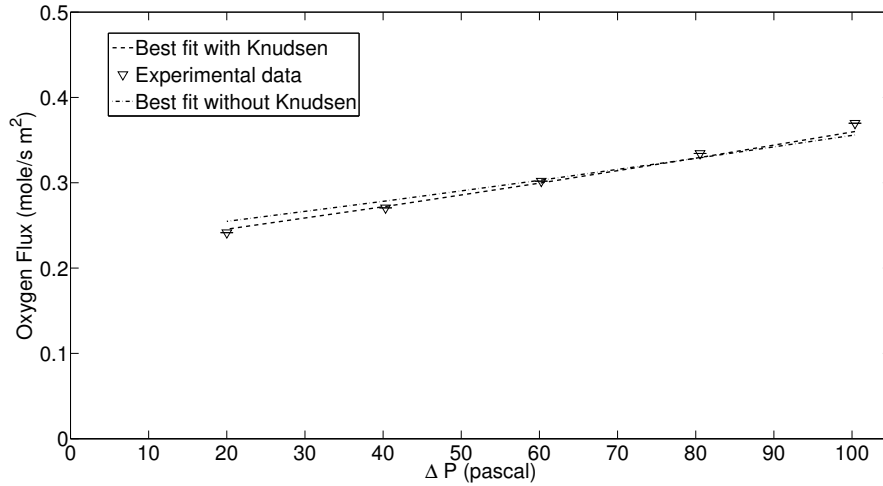


**Figure 3.22** – Diffusibility comparison with and without Knudsen diffusivity

Table 3.7 shows the results for the samples. The diffusibility estimated for GDL+MPL samples is comparable to their carbon substrate alone. The diffusibility is known to depend directly on porosity and tortuosity of the porous media. Since coating of an MPL does not change the porosity significantly, as shown in Table 3.1, diffusibility is not affected significantly. LaManna et al. [70] and Chan et al. [16] studied the effect of an MPL on diffusibility with carbon substrate loaded with 5% PTFE, and measured the reduction in diffusibility as 38%, and 42%, respectively. Chan et al. [16] used the stochastic model developed by Zamel et al. [55], and estimated the diffusibility for MPL alone as 0.201. Therefore, diffusibility of an MPL is comparable to GDLs. As PTFE content increases in the GDLs, diffusibility decreases significantly, as shown in Table 3.6. Hence, at high PTFE content, GDLs dominate the overall diffusion process in an GDL-MPL entity. Therefore, the difference in the diffusibility results is

not significant for GDL and GDL-MPL entity at high PTFE content.

### 3.5 Conclusions

A diffusion bridge based experimental setup is proposed to measure effective transport properties of porous media i.e. permeability, Knudsen diffusivity and molecular diffusivity in through-plane direction. Effect of PTFE on transport properties is studied by testing Toray 090 samples with 0, 10, 20 and 40% PTFE. The effect of PTFE on a GDL+MPL assembly is also studied by testing GDL+MPL samples loaded with 10, 20 and 40% PTFE.

Permeability is estimated by measuring the pressure drop across porous media at various flow rates. Knudsen diffusivity is measured by conducting permeability experiments with nitrogen and helium at low flow rates to avoid inertial permeability effects. The difference in the permeability results attributed to Knudsen slip. The effective molecular diffusivity is measured by introducing nitrogen and oxygen in the channels of the diffusion bridge. The absolute pressure of nitrogen and pressure difference between oxygen and nitrogen is controlled by pressure controllers. The oxygen concentration at various pressure differentials is measured in the nitrogen channel using an oxygen sensor. Various one dimensional models are used to estimate the transport parameters. Permeability of GDLs is estimated using compressible form of Darcy-Forcheimer equation. Permeability and Knudsen diffusivity for a GDL+MPL entity is estimated by using the Knudsen expression. To estimate effective molecular diffusivity, modified binary friction model is implemented. The permeability results in case of GDLs or permeability - Knudsen diffusivity results in case of GDL+MPL assembly is used in MBFM to estimate molecular diffusivity.

The permeability of Toray 090 samples is obtained in the range of  $1.13 \times 10^{-11}$  -  $0.35 \times 10^{-11} m^2$ , and found to decrease with PTFE content. The permeability and pore diameter for GDL+MPL samples is measured in the range of  $3.04 \times 10^{-13}$  -  $0.8 \times 10^{-13} m^2$ , and  $2.15 - 0.5 \mu m$  respectively. The permeability was found to decrease with PTFE content in GDL+MPL samples. The coating of MPL on carbon substrate decreased the permeability by two orders of magnitude and introduced Knudsen slip to be significant. The diffusibility for GDL and GDL+MPL samples is measured in the range of 0.24 - 0.08, and 0.18 - 0.08 respectively.

The measured parameters are used to fit in the models to predict the transport

properties. Carman-Kozeny model is used to fit for parameter  $K_{CK}$  to predict the permeability. Bruggmen model and percolation correlation parameters are fit in the diffusibility results to predict the diffusion coefficient in through-plane direction. The parameters obtained using the models should be helpful to study the gas behaviour in porous media using 2D and 3D simulations.

# Chapter 4

## Conclusion and Future Work

### 4.1 Conclusion

A diffusion bridge based experimental setup is proposed to accurately determine the mass transport properties of gas diffusion media in PEM fuel cells. The mass transport properties that are studied are permeability, Knudsen diffusivity and effective diffusivity. A thorough literature review is done to study the anisotropy of porous media with respect to the transport properties. Many researchers across the fuel cell community suggested that gas diffusion layers are anisotropic in nature. Hence, two diffusion bridges were designed to conduct experiments in through plane as well as in plane directions. Literature also showed the importance of PTFE and MPL, loaded and coated on gas diffusion layers. Hence, the effect of PTFE and MPL was studied on the mass transport properties. During the assembly of a fuel cell, the gas diffusion layers get compressed. Hence, the effect of compression was also studied in in-plane direction.

An in-plane diffusion bridge is designed to estimate the transport properties in the in-plane direction. The compression of the diffusion layers was controlled by placing the metal shims of known thickness at the edge of the diffusion bridge. The diffusion bridge consists of two channels for two different gases. The channels are separated by a porous media. The permeability, Knudsen diffusivity and effective diffusivity are estimated subsequently without opening/closing the diffusion bridge. The permeability is estimated by measuring the pressure drop across porous media at various flow rates set by a mass flow controller. The experimental data is fit in the compressible form of Darcy - Forcheimer equation to extract transport parameters, i.e., viscous and inertial permeability. The Knudsen diffusivity is estimated by running the permeability experiments using different gases with very different mean free paths, i.e.,

nitrogen and helium. The difference in the permeability measured between the two gases was attributed to Knudsen slip. The effective molecular diffusivity was measured by running two gases in two channels separated by the porous media. The flow rates, absolute pressure, and pressure difference between the channels was controlled by mass flow controllers, back pressure controller, and differential pressure controller, respectively. The moles of oxygen in the nitrogen channel were measured by an oxygen sensor at various differential pressures. Fick - Darcy model was used to fit the experimental data, and effective molecular diffusivity was computed.

The effect of PTFE over permeability was studied by testing Toray 090 samples with 0, 10, 20 and 40% wt PTFE. Samples were also tested at four compression levels corresponding to the thickness of 262, 248, 228, and 204  $\mu\text{m}$ . The viscous permeability was estimated in the range of  $0.98 - 0.13 \times 10^{-11} \text{m}^2$ . The Knudsen diffusivity was estimated to be negligible for a Toray 090 (40% PTFE) sample except for high compressions (27.65% or more). Hence, the Knudsen diffusivity was assumed to be negligible in the samples with less PTFE content. The effect of PTFE and compression was also studied on diffusibility by testing Toray 090 samples with 0, 10, 20 and 40% PTFE. The diffusibility was estimated between 0.52-0.09, and found to have an inverse relationship with PTFE and compression.

A through plane diffusion bridge is designed separately to measure the transport properties in through plane direction. The methodology of the measurement is similar to in-plane measurements using the same flow and pressure controllers. To measure the permeability of gas diffusion layers, the experimental data is fit into the compressible form of Darcy - Forcheimer equation. For MPL coated GDL, Knudsen diffusivity is added to the model and low flow rates are used to neglect the Forcheimer effect. Nitrogen and helium are used for testing in case of GDL+MPL assembly, and experimental data is fit in the model to estimate viscous permeability and Knudsen diffusivity or average pore diameter. Effective diffusivity is estimated using the modified binary friction model. In MBFM, Knudsen diffusivity is assumed to be zero for GDLs while Knudsen diffusivity is estimated from permeability experiments for GDL+MPL assembly.

The effect of PTFE is studied in both GDL and GDL+MPL assembly, PTFE content is varied as 0, 10, 20 and 40% in GDL, and, 10, 20 and 40% in GDL, coated with an MPL, samples. The viscous permeability for GDLs is measured in the range of  $1.13 - 0.35 \times 10^{-11} \text{m}^2$ . The viscous permeability and average pore diameter for

GDL+MPL assembly is measured in the range of  $3.04 - 0.8 \times 10^{-13} m^2$  and  $2.15 - 0.5 \mu m$ , respectively. The diffusibility for GDLs and GDL+MPL assemblies is estimated in the range of 0.23 - 0.07 and 0.2 - 0.08, respectively. The viscous permeability, Knudsen diffusivity and effective diffusivity were measured to decrease with PTFE content for both GDL and GDL+MPL samples.

The viscous permeability results were fitted to the Carman-Kozeny model. The Carman-Kozeny parameter was estimated for various GDL samples for in-plane and through-plane directions. Bruggmenn's empirical model and percolation model were fitted to the diffusibility results for in-plane and through-plane directions, and parameters were extracted. The fitting parameters estimated for various GDL samples in both in and through plane directions could be very useful for 2D or 3D simulations.

In summary, the contributions of this thesis are following :

1. The development of a diffusion bridge based experimental setup to measure mass transport properties viz permeability, Knudsen diffusivity and effective molecular diffusivity of PEM fuel cell layers
2. The measurement of transport properties in through and in-plane directions
3. Estimation of transport properties in Carman-Kozeny, Bruggmenn and Percolation correlations to predict the transport properties in both directions

## 4.2 Future Work

As discussed in literature review, water condensation is a problem for thick gas diffusion layers. The liquid water hinders the path of the reactant gases to reach the reaction site. Hence, the permeability and diffusivity properties of the layer are affected in the presence of liquid water. The current setup is unable to measure the transport properties with gases saturated with water at various levels. So far no experimental data is available for permeability and diffusivity in either in-plane or through-plane direction. The setup can be modified to saturate the gases, measure the saturation using a humidity sensor, and then measure the transport properties.

The current setup does not measure the transport properties with compression in through-plane direction. Hence, the diffusion bridge used for through plane direction could also be modified to include compression. The permeability results with compression in through plane direction are available in literature but no study is available

for diffusivity.

The experimental study can also be extended to measure the transport properties of catalyst and micro porous layers individually. Currently the challenge in the measurement is the availability of thick layers. The layers need to be thick enough to measure the average properties. The methodology of measurement might need to be changed since the permeability of layers is expected to be very low hence convection through the layers would be difficult.

# References

- [1] Li X. Diversification and localization of energy systems for sustainable development and energy security. *Energy Policy*, 33(17):2237–2243, 2005.
- [2] Li X. *Green Energy: Basic Concepts and Fundamentals*, volume 1. Springer, 2011.
- [3] Terefe B. Greenhouse Gas Emissions from Private Vehicles in Canada, 1990 to 2007, May 2010. URL <http://www.statcan.gc.ca/pub/16-001-m/2010012/part-partie1-eng.htm>. Taken on September 08, 2014.
- [4] *Canada's Emissions Trends 2012*. Environment Canada, August 2012. URL [http://www.ec.gc.ca/Publications/253AE6E6-5E73-4AFC-81B7-9CF440D5D2C5/793-Canada%27s-Emissions-Trends-2012\\_e\\_01.pdf](http://www.ec.gc.ca/Publications/253AE6E6-5E73-4AFC-81B7-9CF440D5D2C5/793-Canada%27s-Emissions-Trends-2012_e_01.pdf). Taken on September 08, 2014.
- [5] Wishart J. D, Dong Z, and Secanell M. M. Optimization of a pem fuel cell system for low-speed hybrid electric vehicles. In *ASME 2006 International Design Engineering Technical Conferences and Computers and Information in Engineering Conference*, pages 757–772. American Society of Mechanical Engineers, 2006.
- [6] Tsuchiya H and Kobayashi O. Mass production cost of pem fuel cell by learning curve. *International Journal of Hydrogen Energy*, 29(10):985–990, 2004.
- [7] Bernardi D. M and Verbrugge M. W. Mathematical model of a gas diffusion electrode bonded to a polymer electrolyte. *AIChE journal*, 37(8):1151–1163, 1991.
- [8] Bernardi D. M and Verbrugge M. W. A mathematical model of the solid-polymer-electrolyte fuel cell. *Journal of the Electrochemical Society*, 139(9):2477–2491, 1992.
- [9] Li X and Sabir I. Review of bipolar plates in pem fuel cells: Flow-field designs. *International Journal of Hydrogen Energy*, 30(4):359–371, 2005.

- [10] Zamel N and Li X. Effective transport properties for polymer electrolyte membrane fuel cells—with a focus on the gas diffusion layer. *Progress in energy and combustion science*, 39(1):111–146, 2013.
- [11] Mathias M, Roth J, Fleming J, and Lehnert W. Diffusion media materials and characterisation. *Handbook of Fuel Cells*, 2003.
- [12] Lim C and Wang C. Effects of hydrophobic polymer content in gdl on power performance of a pem fuel cell. *Electrochimica Acta*, 49(24):4149–4156, 2004.
- [13] Ismail M, Borman D, Damjanovic T, Ingham D, and Pourkashanian M. On the through-plane permeability of microporous layer-coated gas diffusion layers used in proton exchange membrane fuel cells. *International Journal of Hydrogen Energy*, 36(16):10392–10402, 2011.
- [14] J.T.Gostick. and Fowler M. In-plane and through-plane gas permeability of carbon fiber electrode backing layers. *Journal of Power Sources*, 162:228238, 2006.
- [15] Feser J, Prasad A, and Advani S. Experimental characterization of in-plane permeability of gas diffusion layers. *Journal of Power Sources*, 162(2):12261231, 2006.
- [16] Chan C, Zamel N, Li X, and Shen J. Experimental measurement of effective diffusion coefficient of gas diffusion layer/microporous layer in PEM fuel cells. *Electrochimica Acta*, 65:1321, 2012.
- [17] Chen-Yang Y, Hung T, Huang J, and Yang F. Novel single-layer gas diffusion layer based on ptfе/carbon black composite for proton exchange membrane fuel cell. *Journal of Power Sources*, 173(1):183–188, 2007.
- [18] Qi Z and Kaufman A. Improvement of water management by a microporous sublayer for pem fuel cells. *Journal of Power Sources*, 109(1):38–46, 2002.
- [19] Weber A. Z and Newman J. Effects of microporous layers in polymer electrolyte fuel cells. *Journal of The Electrochemical Society*, 152(4):A677–A688, 2005.
- [20] Niedrach L. W. Electrode structure and fuel cell incorporating the same, 1967. US Patent 3,297,484.
- [21] Siegel N, Ellis M, Nelson D, and Von Spakovsky M. Single domain pemfc model based on agglomerate catalyst geometry. *Journal of Power Sources*, 115(1):81–89, 2003.

- [22] Shen J, Zhou J, Astrath N. G, Navessin T, Liu Z.-S. S, Lei C, Rohling J. H, Bessarabov D, Knights S, and Ye S. Measurement of effective gas diffusion coefficients of catalyst layers of PEM fuel cells with a Loschmidt diffusion cell. *Journal of Power Sources*, 196(2):674678, 2011.
- [23] Yu Z and Carter R. N. Measurement of effective oxygen diffusivity in electrodes for proton exchange membrane fuel cells. *Journal of Power Sources*, 195(4): 1079–1084, 2010.
- [24] Shukla S, Taufertshofer K, Bhattacharjee S, Secanell M, Halliop E, Malevich D, and Karan K. Effect of ionomer loading in inkjet printed catalyst coated membranes on pefc performance. In *ASME 2012 10th International Conference on Fuel Cell Science, Engineering and Technology collocated with the ASME 2012 6th International Conference on Energy Sustainability*, pages 123–128. American Society of Mechanical Engineers, 2012.
- [25] Larminie J, Dicks A, and McDonald M. S. *Fuel cell systems explained*, volume 2. Wiley New York, 2003.
- [26] Phroah J. On the permeability of gas diffusion media used in PEM fuel cells. *Journal of Power Sources*, 144:7782, 2005.
- [27] Pharoah J, Karan K, and Sun W. On effective transport coefficients in pem fuel cell electrodes: Anisotropy of the porous transport layers. *Journal of Power Sources*, 161(1):214–224, 2006.
- [28] Ismail M, Damjanovic T, and D.Ingham . Effect of polytetrafluoroethylene-treatment and microporous layer-coating on the in-plane permeability of gas diffusion layers used in proton exchange membrane fuel cells. *Journal of Power Sources*, 195:66196628, 2010.
- [29] Tomadakis M. M and Robertson T. J. Viscous permeability of random fiber structures: comparison of electrical and diffusional estimates with experimental and analytical results. *Journal of Composite Materials*, 39(2):163–188, 2005.
- [30] Tomadakis M. M and Sotirchos S. V. Effective kundsens diffusivities in structures of randomly overlapping fibers. *AIChE journal*, 37(1):74–86, 1991.
- [31] Tomadakis M. M and Sotirchos S. V. Knudsen diffusivities and properties of structures of unidirectional fibers. *AIChE journal*, 37(8):1175–1186, 1991.

- [32] Johnson D. L, Koplik J, and Schwartz L. M. New pore-size parameter characterizing transport in porous media. *Physical Review Letters*, 57(20):2564, 1986.
- [33] Tomadakis M. M and Sotirchos S. V. Ordinary and transition regime diffusion in random fiber structures. *AIChE Journal*, 39(3):397–412, 1993.
- [34] Tomadakis M. M and Sotirchos S. V. Transport properties of random arrays of freely overlapping cylinders with various orientation distributions. *The Journal of chemical physics*, 98(1):616–626, 1993.
- [35] Tamayol A and Bahrami M. In-plane gas permeability of proton exchange membrane fuel cell gas diffusion layers. *Journal of Power Sources*, 196(7):35593564, 2011.
- [36] Hussaini I and Wang C. Measurement of relative permeability of fuel cell diffusion media. *Journal of Power Sources*, 195(12):38303840, 2010.
- [37] Lobato J, Cañizares P, Rodrigo M, Ruiz-López C, and Linares J. Influence of the teflon loading in the gas diffusion layer of pbi-based pem fuel cells. *Journal of Applied Electrochemistry*, 38(6):793–802, 2008.
- [38] Prasanna M, Ha H, Cho E, Hong S.-A, and Oh I.-H. Influence of cathode gas diffusion media on the performance of the PEMFCs. *Journal of Power Sources*, 131(1):147154, 2004.
- [39] Tamayol A, McGregor F, and Bahrami M. Single phase through-plane permeability of carbon paper gas diffusion layers. *Journal of Power Sources*, 204:9499, 2012.
- [40] Ismail M, Damjanovic T, Hughes K, Ingham D, Ma L, Pourkashanian M, and Rosli M. Through-plane permeability for untreated and ptfе-treated gas diffusion layers in proton exchange membrane fuel cells. *Journal of Fuel Cell Science and Technology*, 7(5):051016, 2010.
- [41] Gurau V, Bluemle M. J, De Castro E. S, Tsou Y.-M, Zawodzinski Jr T. A, and Mann Jr J. A. Characterization of transport properties in gas diffusion layers for proton exchange membrane fuel cells: 2. Absolute permeability. *Journal of power sources*, 165(2):793802, 2007.
- [42] Uchida M, Aoyama Y, Eda N, and Ohta A. Investigation of the microstructure in the catalyst layer and effects of both perfluorosulfonate ionomer and ptfе-loaded

- carbon on the catalyst layer of polymer electrolyte fuel cells. *Journal of the Electrochemical Society*, 142(12):4143–4149, 1995.
- [43] Park G.-G, Sohn Y.-J, Yang T.-H, Yoon Y.-G, Lee W.-Y, and Kim C.-S. Effect of ptfе contents in the gas diffusion media on the performance of pemfc. *Journal of Power Sources*, 131(1):182–187, 2004.
- [44] Williams M. V, Begg E, Bonville L, Kunz H. R, and Fenton J. M. Characterization of gas diffusion layers for PEMFC. *Journal of the Electrochemical Society*, 151(8):A1173A1180, 2004.
- [45] Ihonen J, Mikkola M, and Lindbergh G. Flooding of gas diffusion backing in PEFCs physical and electrochemical characterization. *Journal of the Electrochemical Society*, 151(8):A1152A1161, 2004.
- [46] Carrigy N. B, Pant L. M, Mitra S, and Secanell M. Knudsen Diffusivity and Permeability of PEMFC Microporous Coated Gas Diffusion Layers for Different Polytetrafluoroethylene Loadings. *Journal of The Electrochemical Society*, 160(2):F81F89, 2013.
- [47] Hirschfelder J. O, Curtiss C. F, Bird R. B, and others . *Molecular theory of gases and liquids*, volume 26. Wiley New York, 1954.
- [48] Agarwal R. K, Yun K.-Y, and Balakrishnan R. Beyond navier–stokes: Burnett equations for flows in the continuum–transition regime. *Physics of Fluids (1994-present)*, 13(10):3061–3085, 2001.
- [49] Pant L. M, Mitra S. K, and Secanell M. Absolute permeability and Knudsen diffusivity measurements in PEMFC gas diffusion layers and micro porous layers. *Journal of Power Sources*, 206:153160, 2012.
- [50] Bruggeman D. Calculation of various physics constants in heterogenous substances i dielectricity constants and conductivity of mixed bodies from isotropic substances. *Annalen der Physik*, 24(7):636–664, 1935.
- [51] Neale G. H and Nader W. K. Prediction of transport processes within porous media: diffusive flow processes within an homogeneous swarm of spherical particles. *AIChE Journal*, 19(1):112–119, 1973.
- [52] Das P. K, Li X, and Liu Z.-S. Effective transport coefficients in pem fuel cell catalyst and gas diffusion layers: beyond bruggeman approximation. *Applied Energy*, 87(9):2785–2796, 2010.

- [53] Nam J. H and Kaviany M. Effective diffusivity and water-saturation distribution in single-and two-layer pemfc diffusion medium. *International Journal of Heat and Mass Transfer*, 46(24):4595–4611, 2003.
- [54] Zamel N, Astrath N. G, Li X, Shen J, Zhou J, Astrath F. B, Wang H, and Liu Z.-S. Experimental measurements of effective diffusion coefficient of oxygen-nitrogen mixture in PEM fuel cell diffusion media. *Chemical Engineering Science*, 65(2): 931937, 2010.
- [55] Zamel N, Li X, and Shen J. Correlation for the effective gas diffusion coefficient in carbon paper diffusion media. *Energy & Fuels*, 23(12):6070–6078, 2009.
- [56] Zamel N, Li X, Becker J, and Wiegmann A. Effect of liquid water on transport properties of the gas diffusion layer of polymer electrolyte membrane fuel cells. *International Journal of Hydrogen Energy*, 36(9):5466–5478, 2011.
- [57] Marrero T and Mason E. A. Gaseous diffusion coefficients. *Journal of Physical and Chemical Reference Data*, 1(1):3–118, 1972.
- [58] Winkelmann J. Measurement methods: Diffusion of gases in gases, liquids and their mixtures. *Landolt Bornstein Database*, 2007.
- [59] Rohling J, Shen J, Wang C, Zhou J, and Gu C. Determination of binary diffusion coefficients of gases using photothermal deflection technique. *Applied Physics B*, 87(2):355–362, 2007.
- [60] Astrath N. G, Shen J, Song D, Rohling J. H, Astrath F. B, Zhou J, Navessin T, Liu Z. S, Gu C. E, and Zhao X. The effect of relative humidity on binary gas diffusion. *The Journal of Physical Chemistry B*, 113(24):8369–8374, 2009.
- [61] Bendt P. J. Measurements of  $\text{He}^3/\text{He}^4$  and  $\text{H}_2/\text{D}_2$  gas diffusion coefficients. *Physical Review*, 110(1):85, 1958.
- [62] Remick R. R and Geankoplis C. J. Binary diffusion of gases in capillaries in the transition region between knudsen and molecular diffusion. *Industrial & Engineering Chemistry Fundamentals*, 12(2):214–220, 1973.
- [63] Remick R. R and Geankoplis C. J. Ternary diffusion of gases in capillaries in the transition region between knudsen and molecular diffusion. *Chemical Engineering Science*, 29(6):1447–1455, 1974.

- [64] Evans III R, Watson G, and Truitt J. Interdiffusion of gases in a low permeability graphite at uniform pressure. *Journal of Applied Physics*, 33(9):2682–2688, 1962.
- [65] Evans III R, Watson G, and Truitt J. Interdiffusion of gases in a low-permeability graphite. ii. influence of pressure gradients. *Journal of Applied Physics*, 34(7):2020–2026, 1963.
- [66] Henry Jr J, Cunningham R, and Geankoplis C. J. Diffusion of gases in porous solids over a thousand-fold pressure range. *Chemical Engineering Science*, 22(1):11–20, 1967.
- [67] Reist P. C. Steady-state measurement of krypton-85-air diffusion coefficients in porous media. *Environmental science & technology*, 1(7):566–569, 1967.
- [68] Walker R and Westenberg A. Molecular diffusion studies in gases at high temperature. i. the “point source” technique. *The Journal of Chemical Physics*, 29(5):1139–1146, 1958.
- [69] Whitaker S. Role of the species momentum equation in the analysis of the stefan diffusion tube. *Industrial & Engineering Chemistry Research*, 30(5):978–983, 1991.
- [70] LaManna J. M and Kandlikar S. G. Determination of effective water vapor diffusion coefficient in pemfc gas diffusion layers. *international journal of hydrogen energy*, 36(8):50215029, 2011.
- [71] Hwang G and Weber A. Effective-Diffusivity Measurement of Partially-Saturated Fuel-Cell Gas-Diffusion Layers. *Journal of The Electrochemical Society*, 159(11):F683F692, 2012.
- [72] Kramer D, Freunberger S. A, Flckiger R, Schneider I. A, Wokaun A, Bchi F. N, and Scherer G. G. Electrochemical diffusimetry of fuel cell gas diffusion layers. *Journal of Electroanalytical Chemistry*, 612(1):6377, 2008.
- [73] Flckiger R, Freunberger S. A, Kramer D, Wokaun A, Scherer G. G, and Bchi F. N. Anisotropic, effective diffusivity of porous gas diffusion layer materials for PEFC. *Electrochimica Acta*, 54(2):551559, 2008.
- [74] Becker J, Flckiger R, Reum M, Bchi F. N, Marone F, and Stampanoni M. Determination of material properties of gas diffusion layers: experiments and simulations using phase contrast tomographic microscopy. *Journal of The Electrochemical Society*, 156(10):B1175B1181, 2009.

- [75] Zamel N, Becker J, and Wiegmann A. Estimating the thermal conductivity and diffusion coefficient of the microporous layer of polymer electrolyte membrane fuel cells. *Journal of Power Sources*, 207:7080, 2012.
- [76] Tomadakis M. M and Sotirchos S. V. Transport properties of random arrays of freely overlapping cylinders with various orientation distributions. *The Journal of chemical physics*, 98(1):616626, 1993.
- [77] Pant L. M, Mitra S. K, and Secanell M. A generalized mathematical model to study gas transport in PEMFC porous media. *International Journal of Heat and Mass Transfer*, 58(1):7079, 2013.
- [78] Kerkhof P. J. A modified Maxwell-Stefan model for transport through inert membranes: the binary friction model. *The Chemical Engineering Journal and the Biochemical Engineering Journal*, 64(3):319343, 1996.

# Appendix A

## Factory certificates of sensors

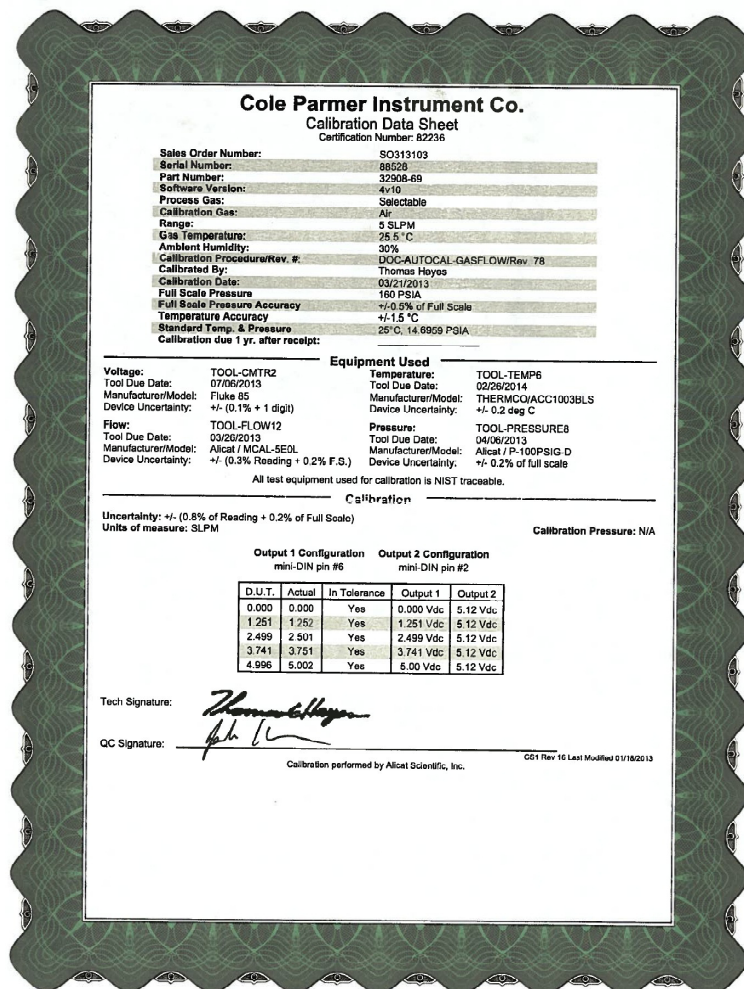


Figure A.1 – Factory certificate of mass flow controller

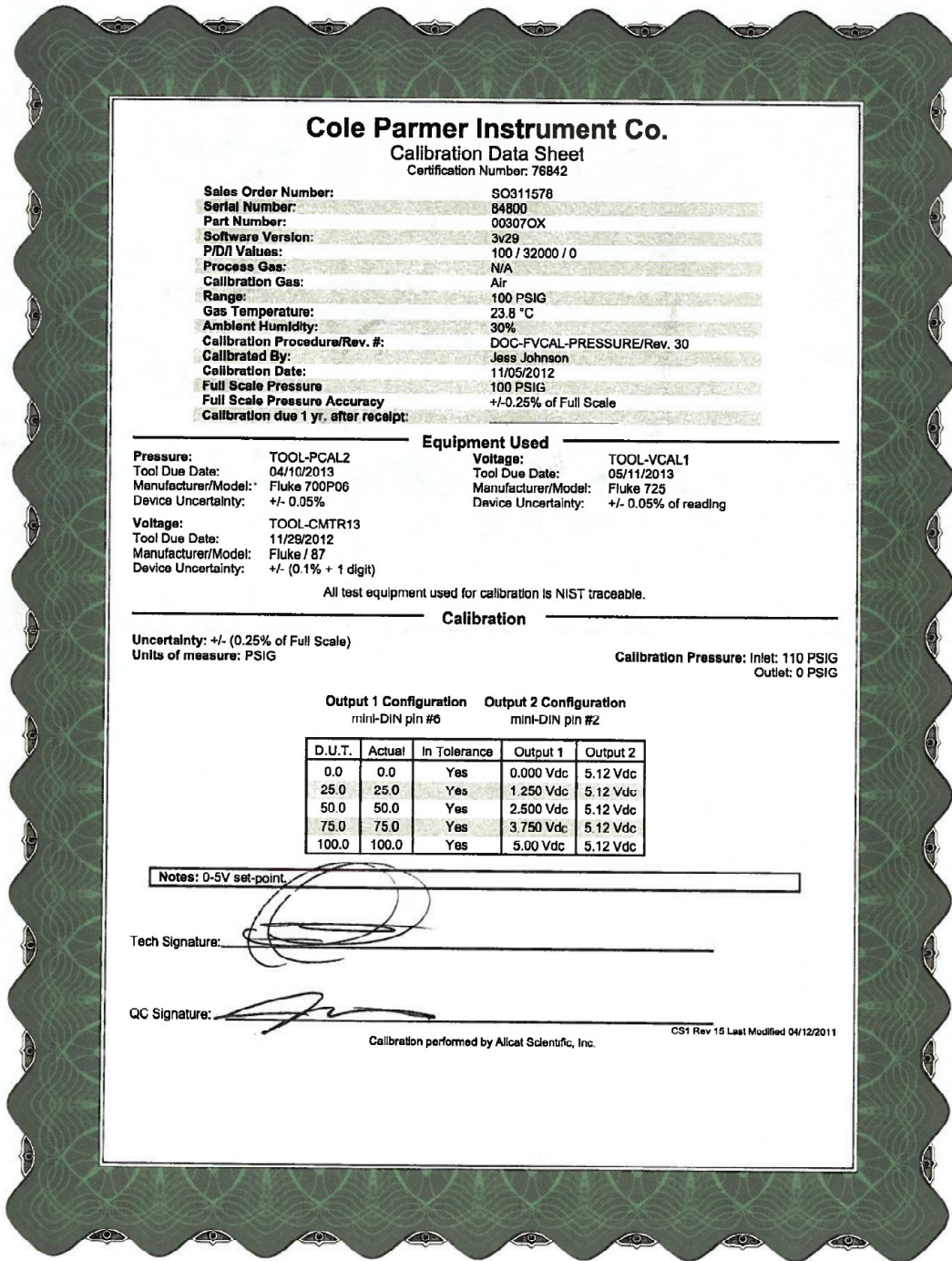


Figure A.2 – Factory certificate of back pressure controller

### Cole Parmer Instrument Co.

#### Calibration Data Sheet

Certification Number: 76838

<b>Sales Order Number:</b>	SO311578
<b>Serial Number:</b>	84801
<b>Part Number:</b>	00307TX
<b>Software Version:</b>	3V29
<b>P/D/I Values:</b>	100 / 32000 / 0
<b>Process Gas:</b>	N/A
<b>Calibration Gas:</b>	Air
<b>Range:</b>	500 Pa
<b>Gas Temperature:</b>	22.8 °C
<b>Ambient Humidity:</b>	30%
<b>Calibration Procedure/Rev. #:</b>	DOC-FVCAL-LPRESSURE/Rev. 22
<b>Calibrated By:</b>	Jess Johnson
<b>Calibration Date:</b>	11/05/2012
<b>Full Scale Pressure</b>	500 Pascal
<b>Full Scale Pressure Accuracy</b>	+/-0.25% of Full Scale
<b>Calibration due 1 yr. after receipt:</b>	

---

**Equipment Used**

**Voltage:** TOOL-CMTR13  
**Tool Due Date:** 11/29/2012  
**Manufacturer/Model:** Fluke / 87  
**Device Uncertainty:** +/- (0.1% + 1 digit)

**Pressure:** TOOL-PCAL7  
**Tool Due Date:** 12/13/2012  
**Manufacturer/Model:** Fluke 717 1G  
**Device Uncertainty:** 0.05% F.S.

All test equipment used for calibration is NIST traceable.

---

**Calibration**

Uncertainty: +/- (0.25% of Full Scale)  
Units of measure: Pa

Calibration Pressure: Inlet: .08 PSIG  
Outlet: 0 PSIG

Output 1 Configuration			Output 2 Configuration	
mini-DIN pin #6			mini-DIN pin #2	
D.U.T.	Actual	In Tolerance	Output 1	Output 2
0.0	0.0	Yes	0.000 Vdc	5.12 Vdc
125.0	125.0	Yes	1.250 Vdc	5.12 Vdc
250.0	250.2	Yes	2.500 Vdc	5.12 Vdc
375.0	375.2	Yes	3.750 Vdc	5.12 Vdc
500.0	500.0	Yes	5.000 Vdc	5.12 Vdc

Notes: 0-5V set-point.

Tech Signature: \_\_\_\_\_

QC Signature: *p.d.w.* \_\_\_\_\_

Calibration performed by Allcat Scientific, Inc. CS1 Rev 15 Last Modified 04/12/2011

Figure A.3 – Factory certificate of differential pressure controller

**OMEGADYNE INC.**  
**An Affiliate of Omega Engineering, Inc.**  
**CERTIFICATE OF CALIBRATION**

**Model Number:** MMDDB050BIV10B2C0T3A6

**Serial Number:** 406107  
**Date:** 9/27/2013  
**Job:** R7859

**Capacity:** 3.50 BAR  
**Excitation:** 24.00 Vdc  
**Technician:** GRS

**Pressure Connection:** 1/4-18 NPT Male

**Electrical Connection:** **WIRING CODE**  
 BLACK = - EXCITATION  
 WHITE = + OUTPUT  
 GREEN = N/C  
 RED = + EXCITATION

CALIBRATION WORKSHEET

Pressure BAR	OUTPUT Vdc
0.00	0.002
1.75	5.003
3.50	10.002
1.75	5.003
0.00	0.002

NOTES

**NIST Traceable Number(s):** C-1956, C-2492

Omegadyne Inc., certifies that the above instrumentation has been calibrated and tested to meet or to exceed the published specifications. This calibration was performed using instrumentation and standards that are traceable to the National Institute of Standards and Technology. This document also ensures that all testing performed complies with MIL-STD 45662-A, ISO 10012-1, and ANSI/NCSL Z540-1-1994 requirements. After Final Calibration our products are stored in an environmentally controlled stock room and are considered in bonded storage. Depending on environmental conditions and severity of use, factory calibration is recommended every one to three years after the initial service installation date.

*Bruce Lott*  
 Accepted and Certified By

9/27/2013  
 Date

Omegadyne Inc., 149 Stelzer Court, Sunbury, OH 43074 (740) 965-9340  
<http://www.omegadyne.com> email: [info@omegadyne.com](mailto:info@omegadyne.com) (800) USA-DYNE

Figure A.4 – Factory certificate of pressure transducer



830 Douglas Ave.  
Dunedin, FL 34698

### OXYGEN SENSOR QUALITY CONTROL CERTIFICATE OF COMPLIANCE

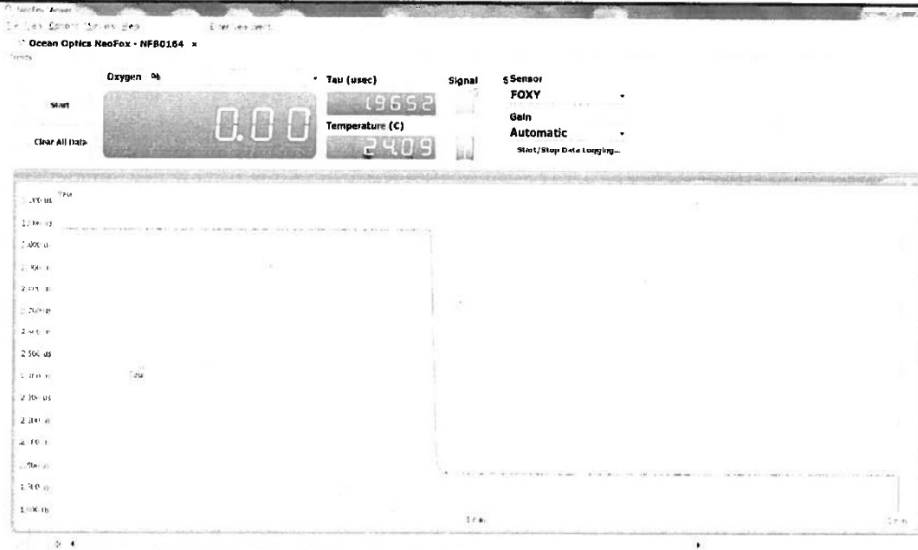
We hereby certify that the below noted sensor has been properly tested to ensure that this product meets or exceeds Internal QC/QA Specifications.

**Test Parameters**

All sensor data is obtained using NeoFox electronics which is set to automatic Gain, APD and Automatic LED settings.

The sensor is exposed to 0% Oxygen (Nitrogen) and 20.9% Oxygen (air) to check for Intensity of the sensor and calculate the Ratio  $R = \frac{\tau_{(nitrogen)}}{\tau_{(air)}}$

Serial Number: M373	Sensor Type: FOSPOR-600-32MM
Signal Intensity Max: X	R = 2.46
Overcoat :NO	Response Time if over-coated:



*Foxy: R > 1.3*  
*Hioxy coating: R > 2*  
*Fospor coating: R > 2*

**Tested By: Pamela Yates**

QFWI3587.1 Rev. A

**Figure A.5** – Factory certificate of oxygen sensor